FREQUENCY AND PHASE LOCKING OF A CW MAGNETRON

WITH A DIGITAL PHASE LOCKED LOOP USING PUSHING CHARACTERISTICS

BY

M. IMRAN TAHIR

ENGINEERING DEPARTMENT
LANCASTER UNIVERSITY

SEPTEMBER **2008**

ABSTRACT

The main body of work presented in this thesis is precise frequency and phase control of a 1.2 kW CW cooker magnetron (National 2M137) locked to a 10 MHz reference injected with a very small RF signal (of the order of -40 dBc) creating a suitable RF source for particle accelerators and other sophisticated applications. We will go on to discuss the characterization of the magnetron with differing heater powers and load conditions when operated with a low cost switched mode power supply. We similarly identify three different regimes of the magnetron operation with respect to the heater power: firstly low noise operation for small heater powers (up to 15W), secondly unstable operation for mid-range heater powers (15W to 30W) and thirdly high noise operation at high heater powers (30W to 54W). We then introduce a novel method to lock the magnetron output frequency to the 10 MHz reference using a digital frequency synthesizer IC (Analog Devices ADF4113) in a negative feedback loop, with this method we exploit the use of the pushing mechanism where the ADF41113 controls the power supply output to vary the magnetron's anode current, keeping its natural frequency locked to the reference. We next investigate the injection locking of the frequency locked magnetron with small injection levels (-29 dBc to -43 dBc) under differing operating conditions and observe a phase jitter performance of the order of+/-13^{o} for very small heater power and -29 dBc injection level. We then fast switch/ramp the injection phase and establish the maximum rate of change of the magnetron output phase. This rate was found to be 4π/us for -29 dBc injection level and 44W heater power. We finally discuss the implementation of a fast DSP based feedback control on the injection phase to improve the magnetron phase jitter performance to below 1^{o} r.m.s.

TABLE OF CONTENTS

CHAPTER 1

INTRODUCTION

The major advance set out in this thesis is a novel technique for phase locking magnetrons with very low injection powers [25]. When a magnetron is injection locked it effectively operates as an amplifier, this is because its output frequency and phase follow the injection source [35].

For most applications magnetrons are operated as high power microwave oscillators. A magnetron generates RF power by way of a stream of electron circulating a cathode in crossed electric and magnetic fields, getting bunched and then retarded by way of interaction with coupled cavities forming a slow wave structure in the anode [1], [2]. Typically magnetrons consist of

- A multi-cavity, cylindrical anode block (slow wave structure),
- a central coaxial cathode,
- output couplers in one or several of the cavities
- and a damping structure to shift or eliminate unwanted modes,
- permanent or electro-magnet

these parts are sealed in a vacuum vessel. The components described are shown for a cooker magnetron in Figure 1.1.

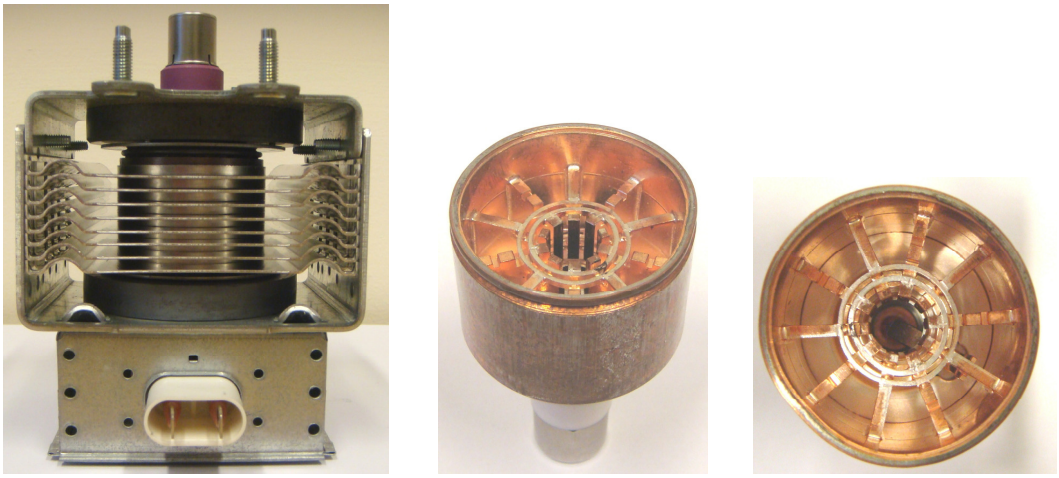

(a) (b) (c)

Figure 1.1 a) Side view of a magnetron with anode block, magnets, cooling fins, output coupling and HT and filament heater Input

b) The anode Block with straps

c) Cross sectional view of the anode block with output cavity coupling

The cathode is maintained at high negative DC potential with respect to the anode block. A DC magnetic field is established through the interaction space between the cathode and anode cavity coupling slots, this magnetic field is perpendicular to the DC electric field.

In the absence of the magnetic field, electrons emitted from the cathode move towards the anode in a purely radial direction following the DC electric field lines. When the magnetic field is applied, the electron trajectories bend and follow curved paths. The force F exerted by the magnetic field B on an electron moving with velocity $\underline{v}$ is given by

$$\underline{F} = -e\left(\underline{v} \times \underline{B}\right) \qquad \text{N} \qquad (1.1)$$

where e = 1.6×10^{-19} C.

For increasing magnetic field, the radius of curvature for the electrons decreases. Above a certain value of the magnetic field called the cut-off magnetic field B_c the electrons are returned to the cathode and the anode current is cut-off. A magnetron is always operated at a level where conduction between the anode and the cathode would be cut-off in the absence of an RF field in the cavities.

In the absence of an RF field the electrons form a circulating cloud around the cathode which reduces the electric field at the cathode and limits further emission. A mathematical description of this cloud was first given by Brillouin [66]. We shall frequently call this circulating cloud of electrons the Brillouin hub. Electrons within the space charge cloud and moving under the influence of crossed DC electric and magnetic fields may typically form circular orbits centralised on the cathode. Beyond the space charge cloud (nearer to the anode) solitary electrons move on epi-cycloidal paths.

Initial RF excitation of the cavities arises through interaction with small density fluctuations (noise) of the circulating electrons. Once the cavities have a small level of excitation, circulating electrons then interact with the fringing RF field in each gap. If an electron is moving in a circular orbit near the top of the Brillouin hub and gets retarded by a fringing electric field it will lose velocity; applying (1.1) the force generating the circular motion is reduced hence the radius of orbit increases. As the radius of orbit increases the DC electric field allows the velocity lost to be recovered. Any such retardation of electrons delivers RF energy to the cavity fields. Alternatively if an electron is moving near the top of the Brillouin hub in a circular orbit centralised on the cathode and gets accelerated by a fringing electric field it will

gain velocity; the force generating the circular motion is increased hence the radius of orbit decreases. The electron is turned back to the cathode. Although the initial acceleration of the electron takes RF energy from the cavity, the overall subtraction is very limited as the electron makes no further progression in the fringing field.

The fringing electric field selects electrons from the Brillouin hub enabling them to move outwards towards the anode, other electrons are forced to remain in the Billouin hub, the associated characteristic orbits are shown in Figure 1.2a.

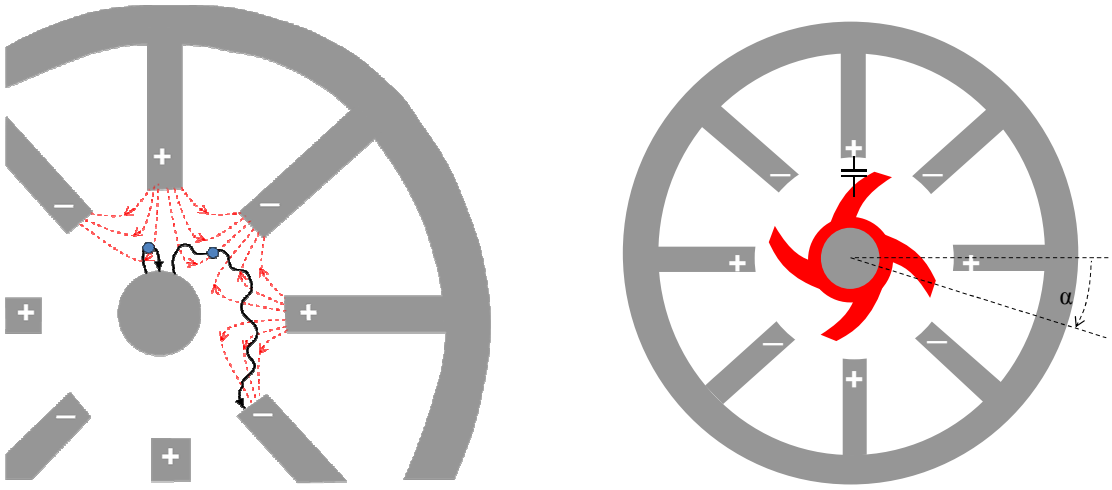

Figure 1.2 a) Electron motion in the interaction space b) Spoke formation

Once the RF field is fully developed the electron distribution takes the form of rotating spokes radiating from a rotating hub as shown in Figure 1.2b. The spokes are formed by the bunching effect the travelling RF slow wave along the anode cavities. Electrons phased such that they move closer to the anode continue to lose energy to the RF field and gain it from the DC field. It is these electrons that form the spokes. The electrons which are turned back form the gaps.

Magnetrons have a number of coupled cavities which may also be referred to as cells. As a consequence the overall anode structure can support a number of RF waves with differing phase advances per cell. These differing waves typically have differing frequencies and phase velocities, they are referred to as modes. The modes can be distinguished by their phase advance per cell. . Magnetrons are normally excited in the π mode where there is a phase advance of 180 degrees per cells and hence the field alternates on each anode gap. For the π mode the phase velocity of the slow wave equals twice the vane separation times the RF frequency. For continuous transfer of energy from electrons to the RF field (wave), the phase velocity of the slow wave and the velocity of the electrons must be synchronised. On average the RF period must be identical to the time it takes for electrons in a spoke to traverse two gaps. The number of spokes is half the number of cavities. The bunching of electrons to form of spokes is known as phase focusing. One notices that whilst average periods for the RF wave and electronic motion are identical, there will be a phase offset α between spokes and the RF wave and this phase can fluctuate with time and its steady state value depends on the magnetron operating parameters.

For a specific applied voltage V_c on the anode, there is a corresponding magnetic field B_c where electrons emitted (singly) from the cathode just miss the anode block and return to the cathode. In this instance the anode current will be zero. The values of V_c and B_c are known respectively as Hull cut-off voltage and magnetic field [1], [63].
The Hull cut-off voltage is related to the Hull cut-off magnetic field as

$$V_c = \frac{e}{m_e}\frac{1}{8}B_c^2 b^2\left(1-\frac{r_c^{\,2}}{r_a^{\,2}}\right)^2 \qquad \text{T} \qquad (1.2)$$

where r_a = anode radius

r_c = cathode radius

V_o = voltage applied between the anode and the cathode

e/m_e =1.759 × 10^{11} C kg^{-1}.

(Note that (1.2) gives an anode voltage which is positive with respect to the cathode.)

Consequently we have that for a given voltage $V = V_c$ equation (1.2) determines a value for B_c such that when $B > B_c$ electrons will not reach the anode. Similarly for voltages $V < V_c$ for a corresponding B_c electrons will not reach the anode.

The velocity of electrons reaching the anode at cut-off is determined as

$$v_c = \sqrt{\frac{2eV_c}{m_e}} = \frac{e}{2m_e} B_c b\left(1 - \frac{r_c^{\,2}}{r_a^{\,2}}\right) \quad \text{m s}^{-1} \qquad (1.3)$$

Hence the angular velocity ω_c of the electrons as they reach the anode is given as

$$\omega_c = \frac{v_c}{b} = \frac{e}{2m_e} B_c \left(1 - \frac{r_c^{\,2}}{r_a^{\,2}}\right) \quad \text{rad s}^{-1} \qquad (1.4)$$

As has been said, for a magnetron to oscillate, it is necessary that electronic angular velocity is synchronised to the velocity of the travelling wave on its slow wave structure. If ω_e is the average angular velocity of the electrons, then the time T taken by an electron to move between the centres of adjacent anode gaps is given by

$$T = \frac{2\pi}{N\omega_e} \quad \text{s} \qquad (1.5)$$

where N is the number of resonant cavities in the anode block.

Where the anode block has N coupled cavities, there exist N modes associated with the fundamental resonance of an isolated cavity. The differing modes correspond to a differing phase advance ϕ_i between cells. As has been said the magnetron is normally operated in the π-mode where the phase advance per cell is 180^o hence the electric

field alternates on each gap. In order for a π-mode to exist on a periodic structure N must be even. Each of the modes will have an associated frequency and if the cavities are identical with no asymmetries then $\frac{N}{2}-1$ modes will be degenerate [1] (where N is even).

The coupled cells effectively form a transmission line. For a magnetron this transmission line closes on itself. Were the transmission line not to be not closed on itself the phase advance per cell φ would have a continuous dependence on the angular frequency of the wave ω. Note that the transmission line will have a limited pass-band. Associated with a phase advance of $\varphi(\omega)$ per cell are all the spatial harmonics given as

$$\phi_m(\omega) = \varphi(\omega) - 2\pi m \qquad \text{per cell where } m = 0, \pm 1, \pm 2, \ldots.$$

For a magnetron the slow wave structure is closed on itself hence the total phase shift around the anode block so as to accept oscillation is $2\pi n$ radians,

where $n = 0, \pm 1, \pm 2, \ldots, \pm N/2$ hence

$$N\phi_m = N\{\varphi(\omega_i) - 2\pi m\} = 2\pi n$$

which can be re-written as

$$\varphi(\omega_i) = \frac{2\pi}{N}(n + mN) \qquad (1.6)$$

Here $\varphi(\omega)$ is a function which can be determined from a single cell of the structure and (1.6) determines discrete modal angular frequencies ω_i of the complete N cell magnetron structure.

For an RF angular frequency ω_i the time to advance one radian is given as $1/\omega_i$ hence the time to advance an angle $\varphi_i = \varphi(\omega_i)$ is given as φ_i/ω_i .The angular velocity of the slow wave ω_{sw} is given as the physical angle between two cells divided by the time for the wave to advance by φ_i hence

$$\omega_{sw} = \frac{\text{Physical angle}}{\text{time for advance}} = \frac{\left(2\pi/N\right)}{\left(\varphi_i/\omega_i\right)} = \frac{2\pi}{N\varphi_i}\omega_i \qquad (1.7)$$

this is illustrated in Figure 1.3

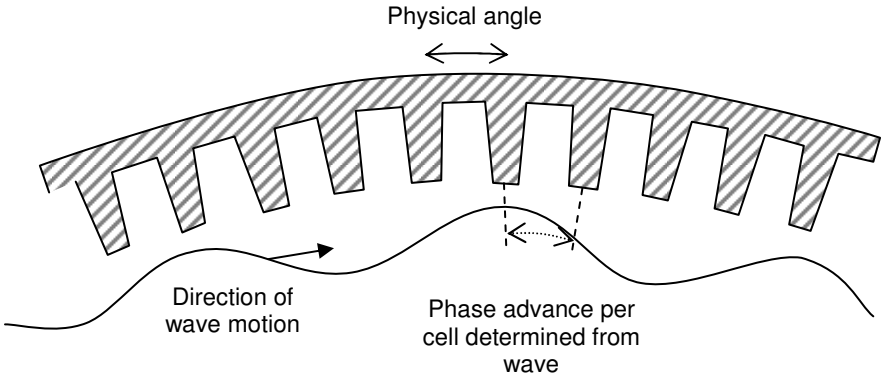

Figure 1.3 Illustration of a wave on a periodic structure

Combining (1.6) and (1.7) we have

$$\omega_i = \left(n + mN\right)\omega_{sw} \qquad (1.8)$$

The Hartree condition for oscillation is that the electron angular velocity equals the angular velocity of the slow wave at the anode i.e. $\omega_e = \omega_{sw}$. (Note that ω_c was also used as the angular velocity of electrons at the anode but only applied on the Hull Cut-Off parabola).

Every point on the Hull Cut-Off parabola has an associated angular frequency for the electrons given by (1.4) hence using (1.8) we can define a characteristic magnetic field B_X on the cut-off parabola where the angular frequency of the electrons equals the angular frequency of the slow wave for a specific mode determined as

$$B_X = \frac{2m_e}{e}\frac{r_a^{\,2}\omega_{sw}}{\left(r_a^{\,2} - r_c^{\,2}\right)} \tag{1.9}$$

Associated with B_X is the characteristic voltage V_X determined by (1.2) i.e.

$$V_X = \frac{m_e}{2e} r_a^{\,2}\omega_{sw}^2 \tag{1.10}$$

Slater [29] shows for arbitrary combined RF and DC fields rotating with the angular velocity ω_e that

$$\frac{V}{r_a - r_c} = B\omega_e\left(\frac{r_c + r_a}{2}\right) - \frac{m_e}{2e}\omega_e^2\left(\frac{r_a^{\,2}}{r_a - r_c}\right) \tag{1.11}$$

where V should be interpreted as the combined DC and RF potential along a line from anode to cathode in frame of rotation, (in the rotating frame V is time independent but takes a differing value for differing angles in that frame). The equation tells us that if an electron arrives at the anode with zero radial velocity, angular velocity ω_e and has moved in a transverse magnetic field B then it must have moved through a voltage V. The Hull Cut-Off applies in the absence of an RF field. When an RF field is present equation (1.11) shows that electrons can travel to the anode for voltages below the Hull Cut-Off. One notices that when $\omega_e = \omega_c$ equation (1.11) is of the form

$$V = V_X\left(2\frac{B}{B_X} - 1\right) \tag{1.12}$$

implying that the line (1.11) goes through a point on the Hull Cut-Off parabola and a little analysis shows that this line is a tangent to the Hull Cut-Off parabola at the point (B_X, V_X). Since V_X and B_X are positive when V from (1.12) is plotted against B the line

has positive gradient but a negative intercept. This means that the equation yields a positive operating voltage when B is large. The Hartree condition requires $\omega_e = \omega_{sw}$ hence substituting (1.8) in (1.11) gives the Hartree equation as

$$\frac{V_H}{r_a - r_c} = B\left(\frac{\omega_i}{n+mN}\right)\left(\frac{r_c + r_a}{2}\right) - \frac{m_e}{2e}\left(\frac{\omega_i}{n+mN}\right)^2\left(\frac{r_a^{\,2}}{r_a - r_c}\right) \qquad (1.13)$$

This equation determines values of the starting anode voltage V_H for a given magnetic field B where the magnetron will start to oscillate. Operating points for magnetrons lie on straight lines determined by m and n which are tangent to the Hull Cut-Off as shown in Figure 1.4.

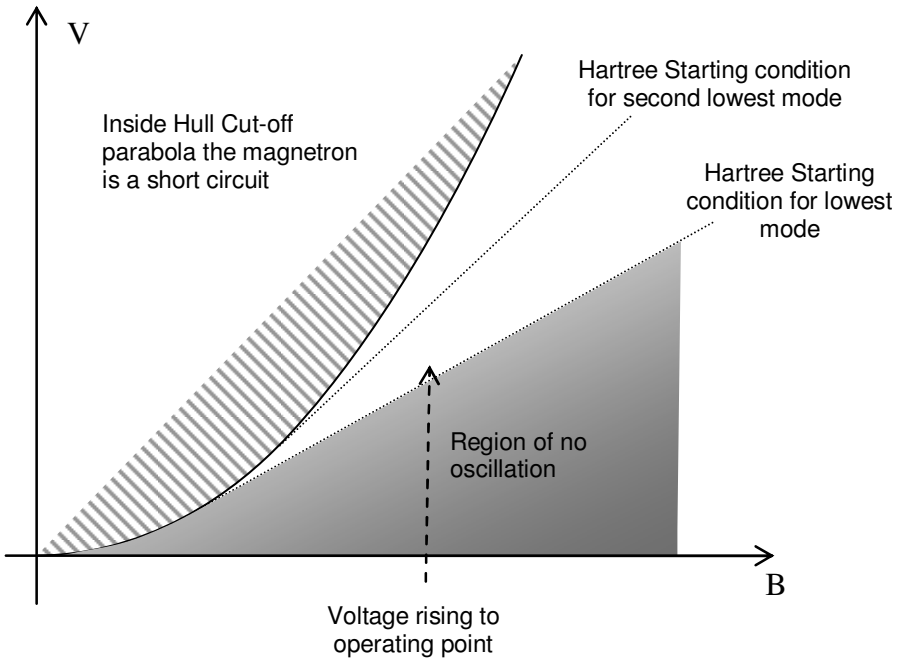

Figure 1.4 Hull cut-off voltage and Hartree Voltage with magnetic field

Inspection of (1.13) together with Figure 1.3 shows that the lowest mode occurs for the minimum value of $\frac{\omega_i}{n+mN}$ and this needs to be the π mode for efficient operation. The anode voltage is applied after the magnetic field and rises until the

starting condition is met. On the Hartree line the radial current is zero hence although the magnetron oscillates it can barely supply any power. Power is delivered at points above the Hartree line.

Different values of $m + nN$ represent different modes of oscillation. When *n = N/2,* the phase shift between two cavities $\varphi_m = \pi$ so that fields are in opposite directions for successive cavities. This mode is known as the π-mode and is almost invariably used for magnetrons as it gives the highest efficiency [31]. For the π-mode the Hartree condition (1.13) becomes

$$V_H = \frac{\omega_\pi}{(1+2m)N}\left(\left(r_a{}^2 - r_c{}^2\right)B - \frac{m_e}{e}\frac{2\omega_\pi r_a{}^2}{(1+2m)N}\right) \qquad (1.14)$$

From Equation 1.13 it can be seen that each mode has a different threshold voltage. The anode block without straps as shown in Fgure 1.2 can be modelled with an equivalent circuit, the simplest possibility is shown in Figure 1.5.

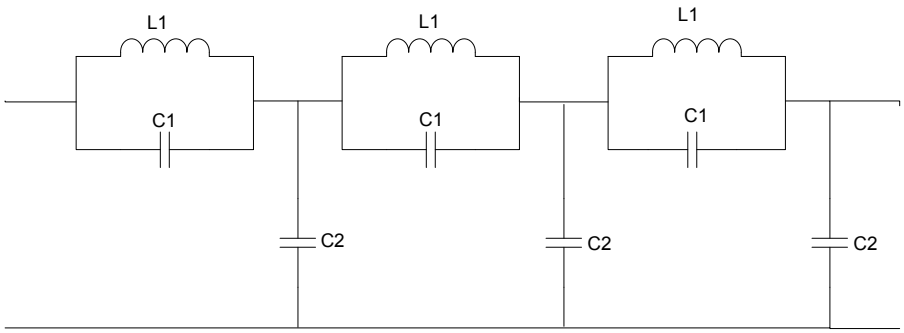

Figure 1.5 Magnetron Equivalent Circuit

When the cell of this equivalent circuit is repeated in an infinite train the transmission line becomes a low pass filter. Frequencies at and above that of the parallel resonator are rejected. The dispersion curve for this network has been derived by Hinkel [1] to be

$$\omega = \left[\frac{L_1 C_2}{1 - \cos\varphi} + L_1 C_1 \right]^{-\frac{1}{2}} \tag{1.15}$$

where φ is the phase advance per cell (cavity). This dispersion curve is illustrated in Fgure 1.6. When a finite number of cells N are connected in a loop rather than being connected in an infinite chain, the phase advance after N cells must be a multiple of 2π hence for a magnetron anode as shown in Figure 1.2 the only allowable phase advances per cell are given as $\frac{2\pi n}{N}$ where n is an integer. Differing phase advances per cell correspond to differing modes with differing frequencies. Modes are marked in Figure 1.6 by vertical lines. When C_2 is small compared to C_1 the dispersion curve for the anode block/transmission line becomes very flat near to the π mode [1].

Where modes are close the magnetron may oscillate in a mode other than the desired mode. The situation is more complex than this as the preferred starting mode will be the mode with the lowest threshold voltage V_H as illustrated in Figure 1.4 and determined by $\frac{\omega_i}{n + mN}$. The dispersion curve of Figure 1.6 gives the π mode as having the highest frequency and not the lowest frequency hence a plane anode as illustrated in Figure 1.2 gives a magnetron that is highly unlikely to start in the π mode.

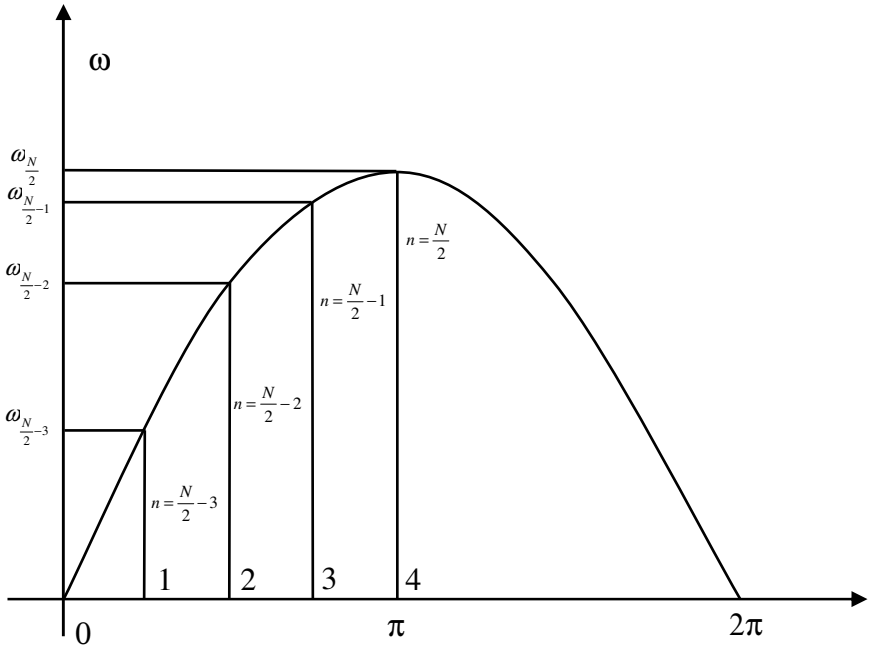

Figure 1.6 Dispersion curve for a magnetron anode structure with N cavities

The mode structure of a magnetron anode can be modified by geometrical changes. The most widely used modification is to add straps as illustrated in Figure 1.1. The work presented in this thesis used a strapped magnetron. The straps are typically formed from four metal rings, two at the top of the anode and two at the bottom. One pair of straps, top and bottom, is connected to the even numbered anode segments and the other pair of straps to the odd numbered anode segments. When the magnetron operates in the π mode each strap is an equi-potential surface and is adjacent to a strap with the opposite polarity. The π mode therefore has a much higher effective capacitance C_1 for the resonator and hence the mode frequency is reduced. This added effective capacitance is reduced progressively for modes with higher iterations from the π mode. An alternate and more rigorous treatment of the dispersion curve for the strapped anode is given by Hinkel [1]. In this analysis an equivalent circuit is formed from delay lines representing the straps and a delay line connecting the top and the bottom straps which represents the anode block.

In order to use our simple equivalent circuit in Figure 1.5 we must assume that C_1 depends on the mode number. This equivalent circuit is useful if we wish to consider in a simple way the manner by which the charged spokes affect the frequency of the π mode. For the π mode (1.15) gives $\omega_\pi = \left[0.5L_1 C_2 + L_1 C_1\right]^{-\frac{1}{2}}$. Setting

$$\omega_r = 1/\sqrt{L_1 C_1} \tag{1.16}$$

one obtains

$$\omega_\pi = \omega_r \frac{1}{\sqrt{1+\frac{C_2}{2C_1}}} \tag{1.17}$$

When a magnetron operates in the π mode, C_1 and ω_r are practically fixed however the effective capacitance C_2 between the vane tips and the electron cloud (Brillouin hub plus spokes) can vary. Consequently the shape, magnitude and relative phase of the electron cloud with its rotating spokes can change the frequency of the operating π mode. Equation (1.17) can be used to give a dynamic relationship between behaviour of the space charge and the magnetron output frequency.

At low power levels and at an instant when the RF field across the gap is at it maximum the spokes are adjacent to the positively charged vanes. Figure 1.2 shows the spokes at position which is slightly advanced from this position. Increasing the anode voltage increases the drift velocity of the spokes and they move forward of vanes at an instant when the RF field across the gap is at it maximum. With this phasing of the spokes the magnetron starts to deliver power. The maximum power is delivered when electrons in the spokes experience maximum retardation from the fields across the resonator gaps. This means that maximum power is delivered when the phasing of the spokes puts them close to the middle of the resonant cavity gaps

when the RF fields has their maximum retarding value. As the phase angle α (shown in Figure 1.2b) between the spokes and the peak field of the RF wave on the anode block increases, the effective capacitance C_2 between the anode block and the electronic charge decreases. The frequency of the magnetron output increases as a result and the phenomenon is known as the pushing effect. Frequency pushing requires a change in the angular speed of the spokes [3]. The phase angle α increases from zero as the spoke phase moves in advance of the phase of RF field on the vanes. As spokes move to a position of maximum power the radial current in the spokes increases and hence the current in the external circuit increases. This means that frequency is instantaneously related to the current flowing between the cathode and the anode. Typically pushing curves for magnetrons are given as plots of frequency against current rather than frequency against voltage. For a magnetron the voltage current characteristic tends to be very flat. An approximate analysis for magnetron steady state voltage current characteristics has been given by Vaughan [31].

The natural π-mode frequency of the magnetron's slow wave structure also depends strongly on its temperature. As the current increases and the electrons hit the anode with more energy, it becomes hot, expands and the output frequency decreases. For many CW magnetrons, the frequency shift associated with temperature variations of the anode is of the same order of the magnitude as that produced by the pushing phenomenon [25].

Another parameter which has a great effect on the output frequency is variation in the load circuit. A change in the load impedance results in a change in the resonance frequency of the loaded slow wave structure. This is the pulling effect. A change in

the load can be determined from the phase angle and the amplitude of the reflected wave from the load [1].

Magnetrons can produce very high output powers. Having a cross field configuration, the magnetron is smaller in size then linear beam tubes such as a klystron and this is significant factor with respect their low cost per installed kilowatt. The magnetron has a reputation for high phase noise and frequency jitter. Much work has been done in the past investigating the sources of noise in magnetron frequency spectra. Like other oscillators, some of the main contributions to the noise come from thermal cycling, power supply ripple (pushing) and load fluctuations (pulling). As the magnetron is a vacuum tube, it relies upon a heated filament cathode to eject the electrons for it to work. This adds another source of noise in frequency spectrum as the frequency depends upon the capacitance between the anode and the cathode as mentioned earlier in the Chapter and due to irregular fluctuation in the space charge this capacitance is not constant [6]. W.C. Brown discovered that turning the filament off once the magnetron had started transforms the magnetron into a very low noise oscillator and in this situation only secondary emission serves as the current source [7], [8],[9]. The noise in magnetrons at higher filament heater powers has been explored previously in great detail due to its use in microwave heating, radar and wireless power transmission applications [10] - [15]. In depth theoretical studies, time domain analysis and computer simulation of the magnetron noise has also been performed over past few decades [16] - [18].

Electron emission from the filament can be divided into two regimes. When the filament voltage is raised from zero, the electron emission initially depends upon the

filament temperature only and is known as temperature limited emission [64]. In this regime the magnetron output has a frequency spectrum that is almost free of random phase noise and spurious oscillations. Above a certain level of the filament heater power and hence filament temperature, the already existing charge layer starts restricting the further emission of the electrons. This is known as the space charge limited emission [65]. In this emission regime, random motion of excess electrons related to a re-arrangement of the space charge about the cathode, causes spurious oscillations in the space charge and hence in the frequency spectrum of the magnetron output [8].

Operating with no heater power and relying completely on the secondary emission can cause the spokes to break-up and result in instability particularly at lower anode currents where there is less secondary emission [9]. An optimum operating point typically exists in the middle of the temperature limited zone [10]. For the magnetron chosen for this work, noise performance related to different heater power levels has been discussed in detail in the *Chapter 2*.

Like other oscillators, the frequency of the magnetron output can be pulled by an external signal which is injected into the magnetron [28], [29]. If the signal is strong enough to pull the magnetron frequency to its own frequency then the process is known as injection locking. The injection locked magnetron is also known as a reflection amplifier [29] - [39]. To guarantee a locking range over the entire frequency band associated with uncontrolled and unwanted disturbances, a large amount of injection power is normally required. To minimise injection power the natural frequency of the magnetron output can be controlled so that it stays very close to the

frequency of the injection signal. There are number of ways to control the natural frequency. One method is to use the pulling characteristics by controlling the amplitude and phase of the reflected power to magnetron with motorised tuning stubs in the output waveguide. This method is slow due to the mechanical motion involved and does not respond to fast changes in frequency.

Another method to reduce injection power is to make use of the pushing characteristics to control the natural frequency by varying the anode current. In 1989, W.C. Brown reported a stabilisation method using a small buck-boost electromagnet adding field to that from the permanent magnet. The consequential change in the crossed magnetic field changes the anode current hence the frequency [8]. The method employed a phase comparator to obtain the phase error between the injection reference and the injection locked magnetron output and used it to change the current through the electromagnet in order to correct the magnetron natural frequency. However the response time in this case was also very slow due to the large inductance of the electromagnets.

Anode current can also be controlled by varying the anode voltage. This is the most rapid method for controlling the anode current and hence the output frequency. The work reported by Kyoto University exploited this method of frequency control however their implementation required a double balanced mixer and a complicated PC based feedback control loop [24].

The intended application in both cases above was for Solar Power Station Satellites using mass produced CW cooker magnetron technology with output powers in the

range 600-1000 W. Another sophisticated application of frequency and phase locked magnetrons is as RF sources for particle accelerators where they can replace large and expensive Klystrons [40]. The novelty of the research work presented in this thesis is the use that is made of recent advances in telecommunication related ICs for frequency and phase control. This work exploits switched mode power supply technology intended for industrial microwave heating. The research work has provided a very low cost and highly integrated solution for frequency and phase locked magnetrons.

In the past frequency locking to an external source has only been achieved by injection locking. In this thesis it is shown for the first time that frequency lock of a 2.45 GHz magnetron to an external 10 MHz reference source can be achieved using frequency agile synthesis technique, where the phase/frequency error from a phase detector is used to control the switched mode power supply output voltage and the magnetron anode current. Detailed design and analysis of the frequency locked magnetron is presented in *Chapter 3*.

Using the method described in the Chapter 3, the centre of our magnetron output frequency spectrum is locked to a multiple of our external 10 MHz reference source. Due to loop bandwidth limitations on the feedback control system described in Chapter 3, all causes of frequency drift cannot be controlled adequately close to zero for the output to be regarded as being phase locked, i.e. there is some residual bandwidth on the magnetron output. With just the control action described in Chapter 3 the spectral quality is still too poor for sophisticated applications. Injection locking is ultimately required to obtain low phase jitter operation. If the injection

source is locked to the same 10 MHz reference as used to stabilise the magnetron frequency then only a very small amount of injection power is required to achieve a phase lock. This novel method is discussed in Chapter 4. All the inputs and system disturbances which would produce frequency shifts before, now affect the phase alone [25]. These phase shifts depend upon the heater power, injection power (level) and anode current ripple level. If the magnetron natural frequency drifts far enough away to cause a phase shift greater than 90 degrees, the frequency feedback control on the magnetron re-adjusts the anode current to bring its natural frequency back.

Once phase locked, the magnetron follows the phase of the injection signal. By exploiting this fact the phase of the injection signal was switched between 0 and 90 degrees, in order to investigate the magnetron response and the rate at which the magnetron output follows the injection phase. The results show that the injection locking exhibits a second order response [41]. This experimental setup and the results are presented in *Chapter 5*.

To make the magnetron suitable for accelerator application, a precise sub-degree control over the magnetron output phase is required. This is achieved by establishing an additional feedback loop that controls the injection signal phase. The error signal for this feedback loop is provided by a fast digital phase detector which tracks the phase difference between the injection signal and the magnetron output. This phase error is then corrected by advancing or retarding the injection phase through an electronic phase shifter or a vector modulator. This method is explained in *Chapter 6*.

Initially in *Chapter 2* the characteristics of the cooker magnetron used for the research when operated with an industrial grade switched mode power supply is considered. It is essential to characterise the free running operation of both the power supply and the magnetron in order to determine the parameters for the feedback control system.

CHAPTER 2

CHARACTERISATION OF THE MAGNETRON 2M137 FOR DIFFERENT PARAMETERS

A number of parameters need to be set in order for a magnetron to oscillate and deliver a required amount of RF power. The principal input parameters are the DC voltage applied between the anode and the cathode, the magnetic field through the anode shell, the low voltage (AC or DC) applied across the cathode filament heater and the RF load. One can regard the oscillation frequency and the output power as output parameters.

A magnetron can be characterised by plotting these various output parameters against input parameters. The most commonly used plots are performance charts (anode voltage plotted against the anode current), pushing curves (frequency of oscillation plotted against anode current), electronic efficiency, and the Rieke Diagram where output power and frequency measured against a varying load are plotted on a polar plot [1]. All these plots are normally available on the manufacturer's datasheet and play a vital role in assessing the suitability of a magnetron for a given task.

The magnetron used for the purpose of this research is a Panasonic 2M137 which delivers a maximum of 1.2kW CW RF Power at 2.45 GHz and is commonly used for industrial heating and cooking applications. Its Datasheet is given in Appendix VI. Although the

datasheet has all necessary plots to determine its suitability for this research, those plots however were obtained using a simple half wave rectifier as the power supply. The power supply used for this research is an industrial standard switch-mode power supply and has different characteristics to a half wave rectifier. As a consequence it was important to obtain all necessary plots for the magnetron with this particular power supply. Detailed plots of interdependence of different magnetron parameters are required in order to decide a number of parameters for frequency feedback control implementation.

2.1 Experimental setup for characterisation of the Magnetron 2M137

The experimental arrangement used to set an operating point for the magnetron and measure different input and output parameters is shown in Figure 2.1. the high voltage between the cathode and the anode is provided by a 2kW switch-mode power supply manufactured by Alter Systems, Italy. This power supply consists of a Pulse Width Modulator (PWM) IC, an H-bridge IGBT inverter, a step up transformer and an output filter. Frequency of the PWM IC is set to 43 kHz as the high power IGBTs cannot switch faster than 20 µs. The 30:1 high voltage step up transformer is wound on a high frequency ferrite core. The low pass filter inside the power supply consists of a 5nF capacitor from HT to ground and a choke in series with the load. The power supply comes with current feedback control and delivers constant current into the load (i.e. magnetron). The current can be varied with a knob provided on the front panel. The circuit diagram of the power supply and further details can be found in Appendix I.

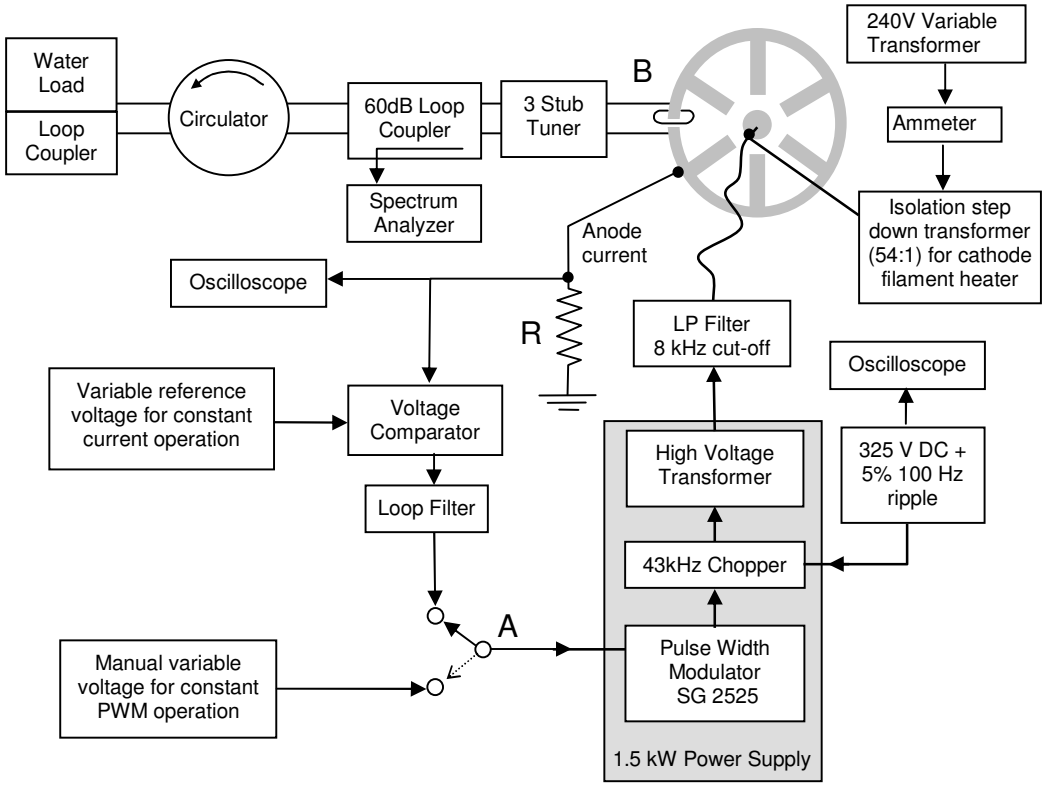

Figure 2.1 Setup for characterisation of the Magnetron 2M137

The default setting for the Alter power supply is a current feedback control mode. The supply has no user facility or simple internal modification for frequency feedback control. Our requirement is to vary anode current in order to correct for frequency drift. A major modification was made by removing the PCBs containing control and submerged interlock circuitry from the power supply enclosure and replacing with our own control and interlock circuit boards. The pulse width of PWM IC can now be controlled either by an external DC voltage (manually variable), a current feedback controller as shown in Figure 2.1 or frequency feedback controller as described in chapter 3. When an external

control voltage is applied, the mode of operation is referred as constant PWM mode in the text to follow.

The voltage applied to the cathode heater filament comes from a 54:1 step down isolation transformer often referred to as the filament transformer. The secondary winding of the filament transformer floats at cathode HT voltage (around -4000V). A variable transformer is inserted between the mains voltage and primary winding of the filament transformer. It gives an output between 260VAC and 0VAC thereby allowing variation of the heater power from zero to slightly above the maximum level recommended by the magnetron manufacturer. An ammeter is placed after the variable transformer in order to measure the current drawn by the primary side of the filament transformer.

2.2 Cathode heater response to its input voltage

Figure 2.2 shows the relationship between the voltage applied to the filament transformer and the input power drawn by the transformer while the magnetron was operational.

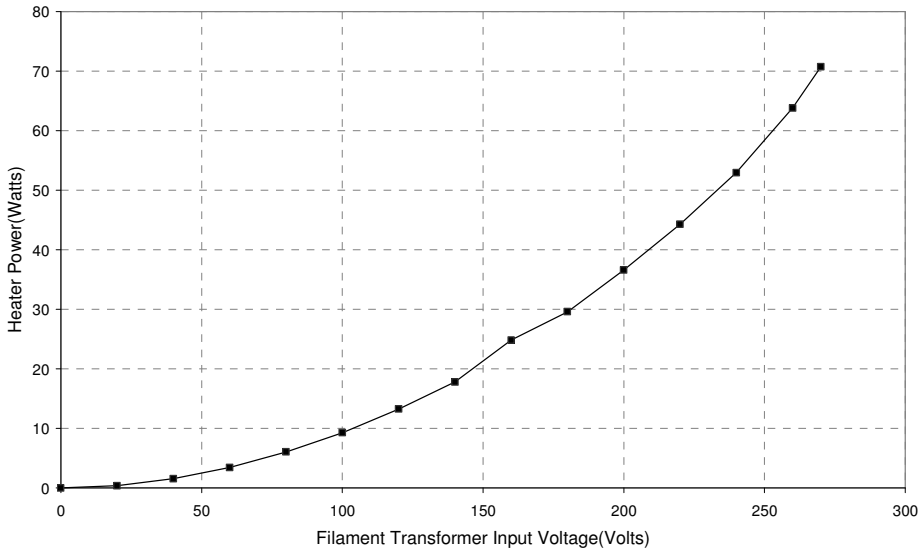

Figure 2.2 Cathode heater input power vs. filament transformer input voltage

One can notice a small kink between 18W and 30W of heater power which is an interesting point on this curve as we subsequently realised that it coincides with the transition between temperature limited and space charge limited electron emission [41]. This transition divides regimes of good and bad frequency and phase noise performance of the magnetron output. Data relating to these regimes is given later in this chapter.

2.3 Pushing Curves

A change in anode voltage changes the current flow between the cathode and anode. This in turn changes the frequency of oscillation and the effect is known as the pushing phenomenon. Building on the work of Welch [3] and adding a few extra assumptions including triangular spokes, constant charge density in the spokes, development of the spoke from the Brillouin radius, rounding of the gap field solution, Vaughan [31] was the

first person to publish a simple model that predicted both performance curves and pushing curves for a range of magnetrons with useful accuracy.

The hub and spoke model used by Vaughan is illustrated in Figure 2.3. Vaughan's model uses Welch's criterion for the phase range in which a spoke will develop. The model assumes charge density in the spoke equals charge density at the top of the Brillouin cloud (hub). This model scales without ad-hoc adjustment for a wide range of magnetron designs. The magnetron model in Figure 2.3 has N vanes and operates in the π-mode. Various dimensions defined in the Figure are

r_a = Distance between the cathode centre and the vane surface

r_b = Distance between the cathode centre and the outer surface of the Brillouin hub

h = Distance between end of one vane to start of the next vane

P = Distance between centre of one vane to the centre of the next vane

t = Vane thickness

V_H = Hartree Voltage

V_a = Applied DC voltage between anode and the cathode

also define

L = Axial length of the spoke

The angles α and β are phase angles, relative to the 2π phase shift over one wavelength (two vanes) on the anode. Angle β is the phase width of the base of the triangular spoke and α is the phase angle between the centre of the gravity of the spoke and zero of the RF potential V_{RF} in the phase focusing half cycle. The phase angle between the maximum and zero of the RF potential is $\frac{\pi}{2}$ (for the π mode) and phase focusing occurs in this range as shown hence the start of the triangular spoke is at the maximum of the RF

potential (i.e. spoke formation begins at the positive peak of phase focusing half cycle). Consequently

$$\alpha = \frac{\beta}{2} - \frac{\pi}{2} \qquad (2.1).$$

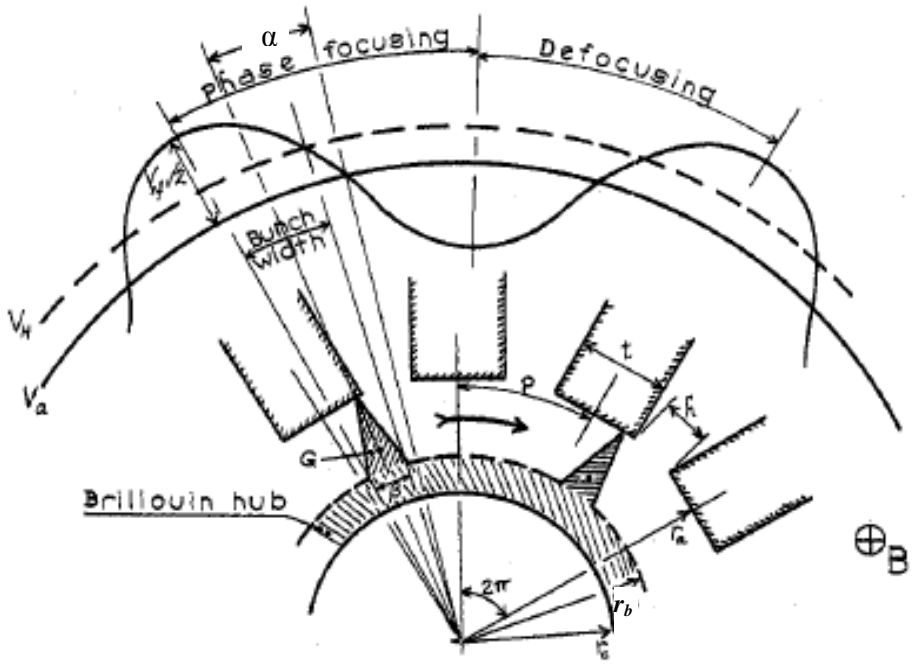

Figure 2.3 Magnetron interaction space and with hub and spoke model, anode voltage components and phase relations (*Image reproduced for illustration, from Vaughan's Research Paper 'A Model for Calculation of Magnetron Performance'* [31])

A relationship between the DC anode current I_{dc} and the tangential component of electric field E_t at point G in Figure 2.3 is derived in [31] as a product of charge density, the average radial velocity at G and spoke cross sectional area at G to be

$$I_{dc} = \rho \frac{E_t}{B} \frac{2L\beta}{3} \frac{2r_b + r_a}{3} \qquad \text{A} \qquad (2.2)$$

where r_b is determined from by solving

$$\frac{8m_eV_a}{eB^2r_c^2}=2\left\{\left(\frac{r_b}{r_a}\right)^2-\left(\frac{r_c}{r_b}\right)^2\right\}\ln\left(\frac{r_a}{r_b}\right)+\left(\frac{r_b}{r_c}-\frac{r_c}{r_b}\right)^2 \qquad (2.3),$$

where the charge density ρ is that at the outer edge of the Brillouin hub determined as

$$\rho=\varepsilon_o\frac{e}{m}B^2\left(\left(1+\frac{r_c^{\,4}}{r_b^{\,4}}\right)/2\right) \qquad (2.4),$$

where the tangential electric field E_t at point G referenced to the spoke (i.e. it moves with the spoke and hence has no explicit time dependence) is determined from an approximate solution to the wave equation in the gap and is given as

$$E_t=\frac{V_{RF}\sqrt{2}}{h}\frac{\sin\left(\pi\frac{h}{P}\right)}{\pi\frac{h}{P}}\frac{\sinh\left(\frac{1}{3}\pi\frac{r_a-r_b}{P}\right)}{\sinh\left(\pi\frac{r_a-r_b}{P}\right)}\cos^2\alpha \qquad (2.5),$$

and where phase width for the base of the spoke β as determined by Welch's criterion namely that the spoke grows from the region where the sum of the anode voltage plus the radial RF voltage exceeds the Hartree threshold voltage is given as

$$\beta=\cos^{-1}\left(\frac{V_H-V_a}{V_{RF}\sqrt{2}}\right) \qquad (2.6).$$

It is now useful to pick out the dependency of magnetron frequency and current on the angle α. Vaughan's model assumed that the charge density $\rho=$constant and this is apparent from (2.3) where it depends only on r_b, r_c and B.

As h, P and r_a are fixed for a particular magnetron it is useful to write (2.5) in the form

$$E_t=K.V_{RF}\cos^2\alpha \qquad (2.7)$$

where $K = \frac{\sqrt{2}}{h} \frac{\sin\left(\pi \frac{h}{P}\right)}{\pi \frac{h}{P}} \frac{\sinh\left(\frac{1}{3}\pi \frac{r_a - r_b}{P}\right)}{\sinh\left(\pi \frac{r_a - r_b}{P}\right)}$ is fixed for a particular magnetron.

The Hartree Voltage has previously been given and for m = 0 we have

$$V_H = B\frac{\omega . r_a^{\,2}}{N}\left[1 - \left(\frac{r_c}{r_a}\right)^2\right] - \frac{2m\omega^2 r_a^{\,2}}{eN^2} \quad \text{V} \tag{1.14a}$$

which has the form

$$V_H = A\omega - C\omega^2 \tag{2.8}$$

where A and C fixed for a magnetron when the magnetic field is fixed and are given as

$$A = B\frac{.r_a^{\,2}}{N}\left[1 - \left(\frac{r_c}{r_a}\right)^2\right] \qquad C = \frac{2mr_a^{\,2}}{eN^2}$$

Substituting (2.8) in (2.6), the angle β can be related to the magnetron output frequency

$$\beta = \cos^{-1}\left(\frac{A\omega - C\omega^2 - V_a}{V_{RF}\sqrt{2}}\right) \tag{2.9}$$

Using (2.6) and (2.8) equation (2.2) can be written to show the frequency dependence as

$$I_{dc} = K.\rho.V_{RF}.\cos^{-1}\left(\frac{A\omega - C\omega^2 - V_a}{V_{RF}\sqrt{2}}\right).\cos^2\alpha \tag{2.10}$$

This can be re-written as

$$A\omega - C\omega^2 = V_a + \sqrt{2}V_{RF}.\cos\left(\frac{I_{dc}}{K.\rho.V_{RF}.\cos^2\alpha}\right). \tag{2.11}$$

Using (2.1) the relationship between I_{dc} and a can also be obtained as

$$I_{dc} = \rho.K.V_{RF}.(2\alpha + \pi)\cos^2\alpha \tag{2.12}$$

A dependency of instantaneous frequency of the magnetron output on the anode current is given by (2.11). It shows that the magnetron can be treated either as a voltage controlled oscillator or as a current controlled oscillator. Equation 2.12 gives the relationship between the anode current and spoke position with respect to the peak of the RF field (angle α). A change in the angle α increases or decreases the effective capacitance between the spoke and the anode and the frequency of the output changes accordingly.

2.3.1 Pushing Curves for the Magnetron 2M137 With Matched Load

The pushing curves obtained by ourselves using the set-up of Figure 2.1 and for the magnetron (2M137) used for all other experimental work presented in this thesis are shown in Figure 2.4. The curves are recorded for different heater power levels and a matched output load (≈ 0.001% reflected power). The shape and relative position of the pushing curves greatly depends upon the heater power. For low heater powers the magnetron output frequency becomes more sensitive to the anode current variation at low anode currents and this is most easily seen from the pushing curves for 33W and 10W heater power in Figure 2.4. The frequency dependence upon heater power will be discussed in further detail later in the chapter.

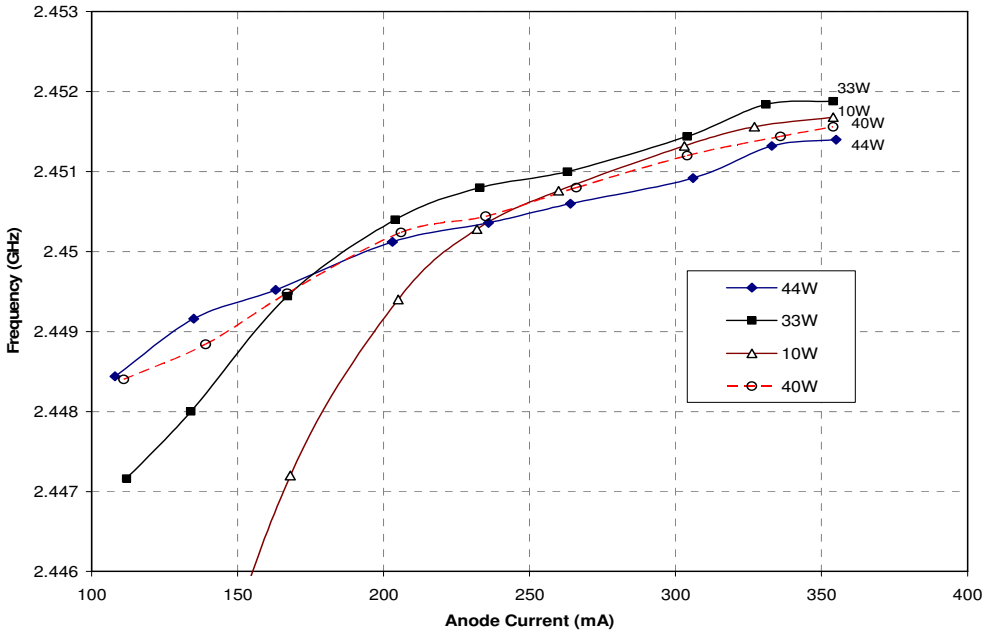

Figure 2.4 Pushing Curves with matched load, for different heater powers

2.3.2 Pushing Curves for the Magnetron 2M137 With Un-matched Load

The shape and relative position of the pushing curves on Figure 2.4 also depends upon the output load of the magnetron. Frequency dependence upon the load is known as frequency pulling. Our measurements showing the effect of the pulling phenomenon on pushing is presented in Figures 2.5a and 2.5b. The pushing curves in these Figures have been measured with nominally 10% reflected power at different phase angles, for two heater powers namely 40W and 10W. Pushing curves with differing reflected powers are normally presented on a Rieke diagram however here for the purpose of comparison they are plotted in the format of the pushing curves (Frequency vs. Anode current).

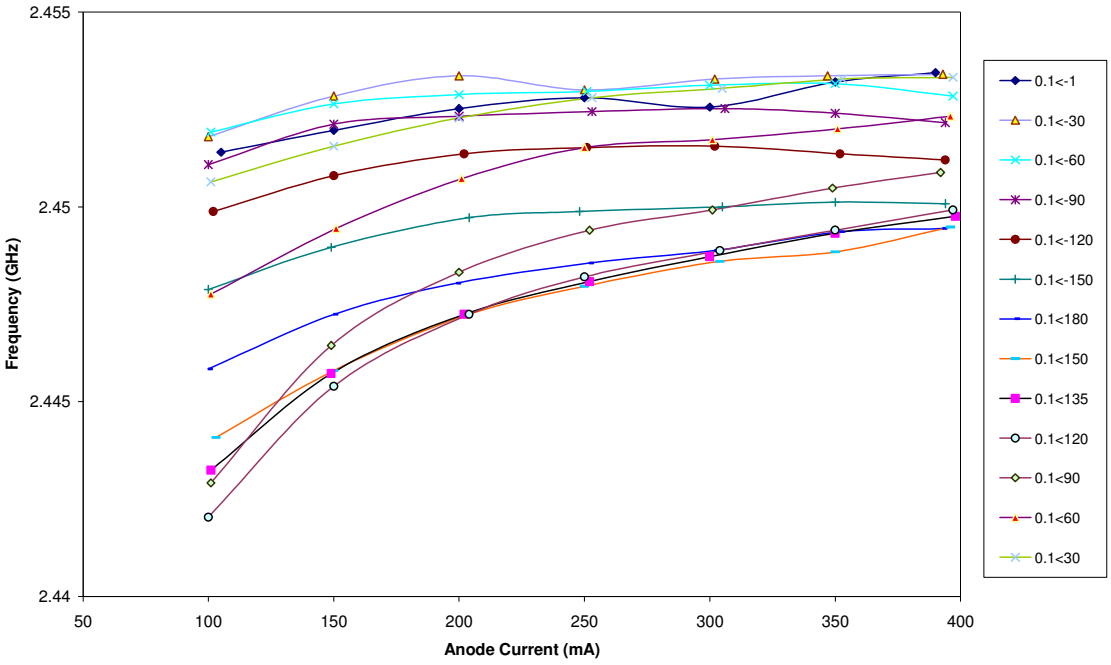

a: Pushing Curves at Heater Power : 40W

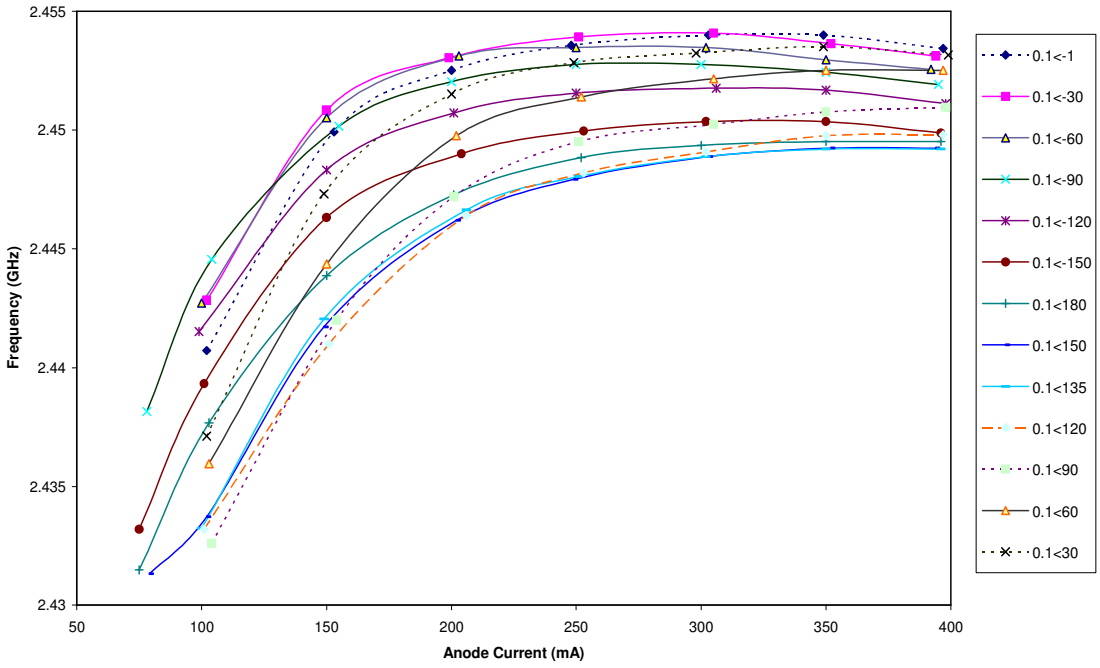

b: Pushing Curves at Heater Power: 10W

Figure 2.5 Pushing Curves with unmatched load at two different heater levels

The load was varied with a 3-stub tuner. Stub positions for this tuner giving specific loads had previously been calibrated by replacing the magnetron with a network analyser through a matched waveguide transition (point B in Figure 2.1).

In order to find the magnetron plane of reference (i.e. load angle at which the magnetron is maximally efficient) the load was varied with 15^{o} steps with a reflection coefficient of 0.1 and efficiency of the magnetron determined on each step from the DC power input and RF power output. A plot of the efficiency vs. load angle (reflected power phase) is shown in Figure 2.6. The magnetron was found to be maximally efficient at the reflection angle of 135^{o}. The polar plot shows that for reflection phases between 120^{o} and 140^{o} efficiency is within 1% of the peak.

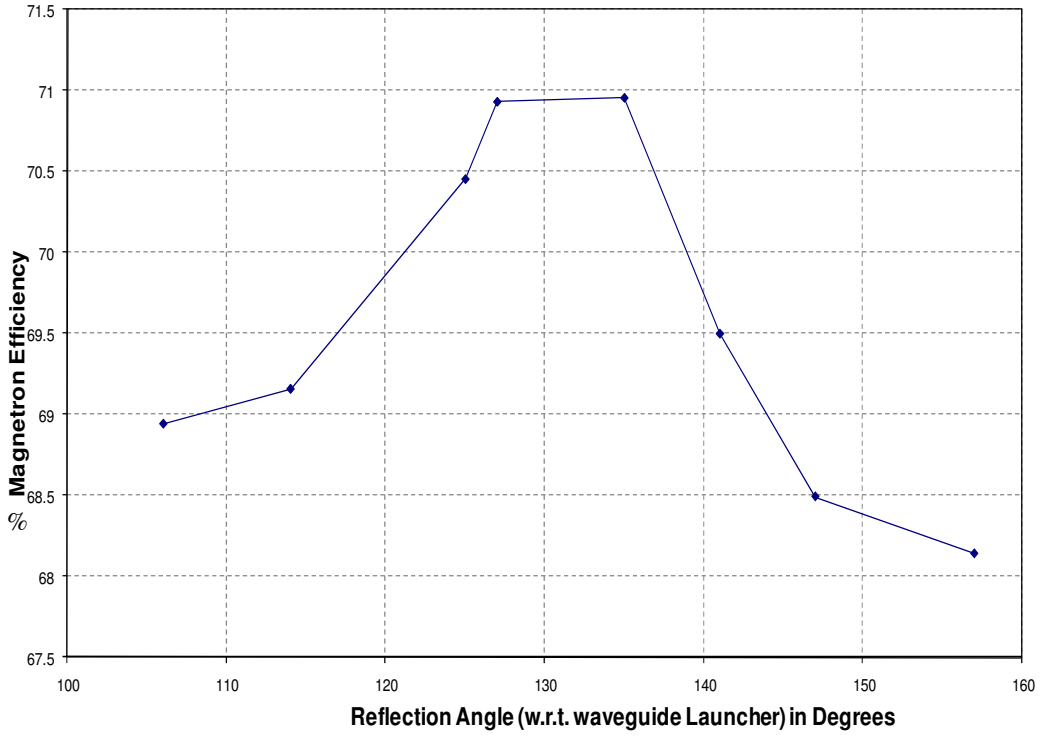

Figure 2.6 Magnetron Efficiency w.r.t the phase of the reflected wave

In Figures 2.5a and 2.5b the pushing curves in the region of maximum efficiency reside at the lowest frequencies. Moving 180^{o} away from curves associated with maximum efficiency (centred at 135^{o}) either towards the load or towards the generator the pushing curves associated with lower efficiencies have increasingly the higher frequencies for a given anode current.

2.3.3 Effect of Space Charge Limited Emission on Pushing Curves

In the case of space charge limited electron emission (corresponding to Figure 2.5a, with a high heater power of 40W) there is an reduction in the pushing curve slope as we move away from the region of maximum efficiency. Towards the generator by 75^{o} or more from the region of maximum efficiency at 135^{o} (i.e. at angles -150^{o}, -120^{o}, $-90^{o,}$ -60^{o}) the pushing curves' slopes start to become negative at about 80% of maximum rated anode current. Moving towards the load by 75^{o} or more from the region of maximum efficiency at 135^{o} (i.e. at angles 60^{o}, 30^{o}, -1^{o}, -30^{o}) gives a pattern of slopes going positive, then negative and then positive again (i.e. they have dips). The dip shifts from higher to lower anode currents as the reflection angle moves to the load. These dips might theoretically exist for reflection angles of -150^{o}, -120^{o}, -90^{o} and -60^{o}, as these curves might turn positive were the anode current to be further increased. Such anode currents however would be beyond the absolute maximum anode current specified by the manufacturer of the magnetron.

The positive slope of the pushing curves prevalent at low anode currents has been associated with a change in the effective capacitance between anode and the Brillouin

space charge hub as the angle α between the RF wave and the spoke position changes [3] (see chapter 1). Brown [9] has attempted to explain the negative slopes on the pushing curves for some operating points at high anode current by considering a broadening of the spokes. No published work gives insight on the dips we have observed.

It is clear from Figure 2.5a that the curves in the region of maximum efficiency are very closely spaced (curves at angles 120^o, 135^o and 150^o) hence the load variations in this region have the least effect on the pushing curves. There are regions either side of the phase of peak efficiency at 135^o which extend from 150^o to -120^o and from 120^o to $30^o$where the pushing curves are very sensitive to variation in the load. The curves tend to become closely spaced again (less sensitive to load variations) as the reflection angles approach to -45^o which is the phase 180^o from the phase of maximum efficiency. In this region (as mentioned earlier) the frequency sensitivity becomes low and the curves suffer from slope reversals (making frequency control by varying the current difficult).

The dependency of the frequency on the anode current is closely linked to the phase of the rotating space charge spokes relative to the phase of peak RF field (previously defined as angle α). For the π mode, simulation shows the crest of the RF field losing most of its amplitude as it crosses the centre of each vane. It is convenient therefore to reference the position of the spoke to an instant when the crest of the RF field is at the centre of a gap and hence the RF voltage at the centre of the gap is zero. At a given operating point when the anode current, anode voltage and RF power output are known then the relative angular position of the spoke to the angular position of the peak RF field (α) will be

determined. When the anode voltage is increased, the electron drift velocity in the crossed magnetic field given by $\frac{E_{radial}}{B}$ increases and the angle α starts to reduce, The spoke is moving forward and away from the positively charged vane behind it referenced to an instant when the vane takes it maximum positive charge (RF field is maximum). The radial electric field is composed of both an RF component and a DC component from the anode voltage. As the spoke advances the radial field contribution from the RF wave is reduced hence the drift velocity falls back to the value required by synchronisation but with the angle α reduced. This response can be visualised from inspection of Figure 2.7 where RF and DC fields are combined.

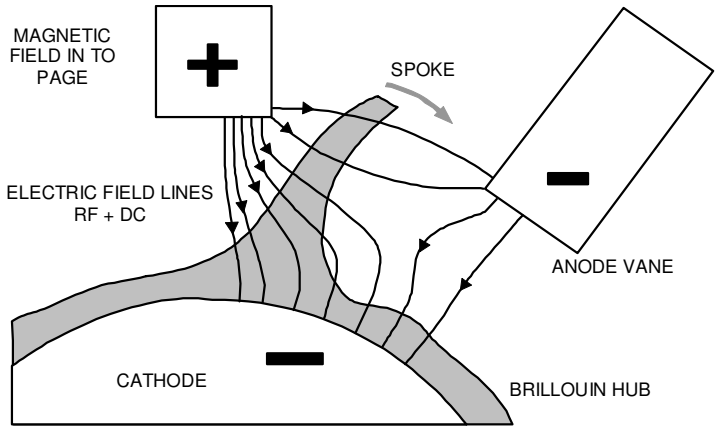

Figure 2.7 Diagram showing magnetron spoke position referenced to the anode vane behind the spoke at the instant that the vane takes its peak positive charge.

If a spoke is phased at the point of maximum RF field i.e. middle of the cavity gap, the electrons emitted from cathode surface face the maximum retarding RF field, and have

maximum transfer of energy to the RF field. With the spoke is at this position electrons see the maximum tangential field, accordingly the drift velocity along the spoke is maximised, hence current is maximised when RF power is maximised. When the spoke is in the middle of the cavity the effective capacitance between the spoke (the effective electrode) and vanes (the effective ground) are smallest hence the slow wave structure's modal frequency as determined by (1.15) is maximised. In contrast when a spoke is phased close to a vane, the tangential retarding RF field is small, hence power transfer is low, drift velocity of electrons along the spoke is low hence DC anode current is low. The effective capacitance between the spoke and the vane is high because of the smaller gap and the magnetron output frequency is lower [3].

2.3.4 Effect of Temperature Limited Emission on Pushing Curves

At reduced heater power when the electron emission from the cathode is presumably temperature limited (dependent on back bombardment), the pushing curves have greater frequency sensitivity for all loads. In Figure 2.5b (10W heater power), the pushing curves in the region of maximum efficiency (reflection phase angles 120^{o}-150^{o}) give frequency changes of about 12 MHz, 3 MHz and 0.5 MHz for anode current changes of 100mA to 200mA, of 200mA to 300mA and of 300mA to 400mA respectively. In contrast corresponding curves in the Figure 2.5a (40W heater power), have frequency changes of just 3 MHz, 1 MHz, 0.75 MHz for the same the anode current variations. The gradient of the pushing curve for low heater power shown in Figure 2.5b is almost independent of the load. There aren't any dips in curves of Figure 2.5b unlike Figure 2.5a. Almost all the pushing curves tend to attain a negative slope at higher anode currents beyond the region

of maximum efficiency. Within the maximum efficiency region and for our presumed case of temperature limited emission given in Figure 2.5b the pushing curves are almost flat above an anode current of 300mA, this is in contrast to Figure 2.5a corresponding to space charge limited emission where pushing curves still have a reasonable slope at high power output levels above 300mA.

2.4 Power Supply Ripples

It is clear from Figure 2.5a and Figure 2.5b that any ripple or jitter present on the anode current modulates the magnetron RF output both in amplitude and frequency**.** There are two major ripple contributions from the switch-mode power supply output shown in Figure 2.1. One is at 100 Hz due to full-wave rectified mains and the other is at 43 kHz which is the operating frequency of the H-Bridge. The upper trace in Figure 2.8 shows the 100 Hz ripple on the 325V DC line measured with a 50:1 differential probe with AC coupling. The corresponding ripple on the anode current at a current level of 310 mA (rms) is shown in the lower trace of Figure 2.8. The anode current was measured across a 47Ω resistance placed between the magnetron anode and the ground plane. The switch-mode power supply SM-445 has a relatively small parallel capacitance of 2.35mF smoothing the full wave rectified mains. When around 5A current is drawn from the mains there is about 5% voltage ripple on 325V DC supply to the chopper. After the HT transformer this input ripple feeds through to give 13% anode current ripple for an anode current of 350 mA (this corresponds to 4000V DC on secondary side of high frequency transformer with 95% power supply efficiency and 65% magnetron efficiency). As

expected both the input ripple and the anode current output ripple decrease when the overall power (input and output) is reduced.

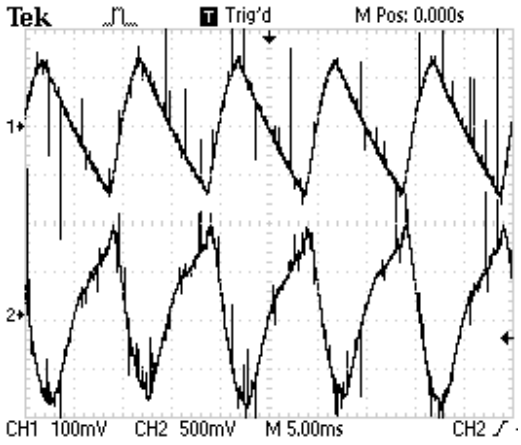

Figure 2.8 CH1 (top trace) shows 100 Hz Ripple on the 325V DC (with 50:1 probe), CH2 (bottom trace) shows the anode current across a 47Ω resistance between anode and ground. (Measurements are for constant PWM operation)

The reason for the 13% ripple at 100 Hz on the anode output current from the HT transformer arising when there is only 5% voltage ripple on the DC input is mainly due to flat voltage current characteristic of the magnetron. Additionally the transformer used in the power supply is designed to operate at 43 kHz and at low frequencies such as 100 Hz, its primary winding impedance is reduced. In constant current mode with current feedback control (as opposed to constant PWM mode), the output ripple on the anode current is reduced by at least factor of 20. However as a main objective of this research,

the anode current needs to be varied in order to correct for frequency drifts, hence constant current operation is not an option.

2.4.1 RF Demodulation with a Diode Detector to accurately measure power output amplitude ripple

The spikes on traces in Figure 2.8 come from electromagnetic pick up (interference) on the measurement probes coming from the 43 kHz power supply switching frequency. This can be demonstrated as their magnitude is independent of the current measurement shunt resistance value. The spikes can be removed with the help of the averaging function on the oscilloscope, however this slightly changes the shape of the ripple near the peaks. The presence of these spike made it is quite difficult to observe the level of 43 kHz ripple on the anode current using the 47Ω shunt resistance. To get an estimate of the 43 kHz ripple on the anode current we looked at both 43 kHz ripple and 100 Hz ripple on the power output from the magnetron and assumed that the ratio of the anode current ripple to output power ripple would be similar at these two frequencies (based on the fact that magnetron response is sub micro-second). A diode detector was used to demodulate the magnetron RF output via the 60 dB loop coupler shown in Figure 2.1 (the spectrum analyser was replaced with a diode detector). Using this method the characteristic spikes we were associating with the 43 kHz electromagnetic interference were removed and a regular 43 kHz oscillation remained. Voltage probe measurements on the chopper input are compared with power output measurements in Figure 2.9. The smaller trace in Figure 2.9a is the 100 Hz ripple on 325V DC line and bigger trace is the output from a diode detector. The diode detector provides an output free of interference as the diode detector

is mounted directly on the waveguide loop coupler, its output is connected to the oscilloscope by a coaxial line and the entire demodulated output path is completely shielded. The spikes seen in Figure 2.9a are on the smaller trace (325V DC ripple) and not on the diode detector output. The small jitter present on the 100 Hz ripple of the power output in 2.9a (bigger trace) is due to the switching frequency of the power supply, and it can be seen more clearly in Figure 2.9b on an expanded timescale. The shape of the ripple also suggests the presence of a more prominent sub-harmonic at 21.5 kHz. The ripple due to the switching frequency (43 kHz) is observed to be about 1/6th of the ripple due to the rectified mains, (the diode detector amplitude response is approximately linear over the measurement range).

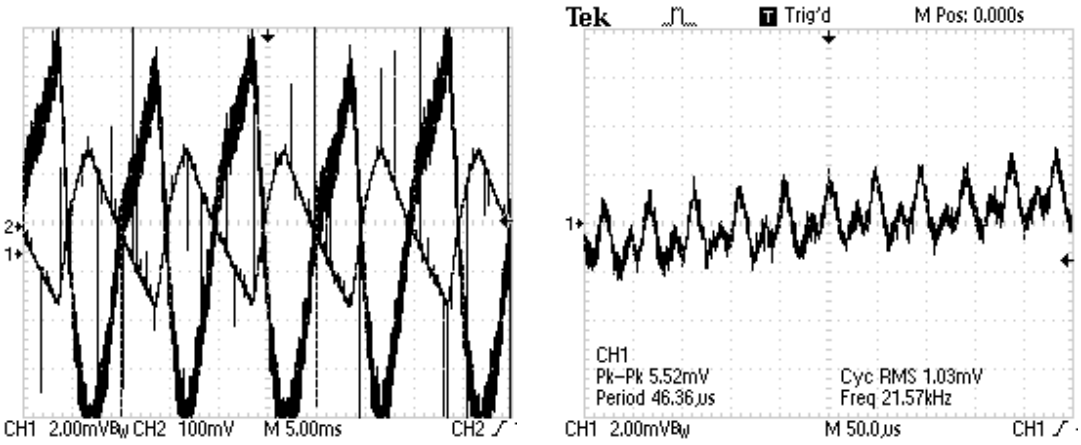

(a) **(b)**

Figure 2.9 Small trace in (a) shows 325V DC ripple at 100 Hz measured with probe on chopper input, large trace in (a) shows RF power output ripple at 100 Hz measured with diode detector, the trace in (b) shows RF power output ripple at 43 kHz measured with diode detector (all with zero cathode heater power).

In order to measure the amplitude ripple contribution from the switch-mode power supply alone the filament heater was turned off for the measurements of Figures 2.8 and 2.9. The filament heater current is AC with a frequency of 50 Hz. When heat power is applied there is no significant 50 Hz additional amplitude ripple on either the RF power output or the anode current. The filament heater does however introduce additional, randomly fluctuating, high frequency noise when the cathode temperature is raised to the region associated with space charge limited emission.

2.5 Effect of heater power and anode current ripple on magnetron output frequency spectrum in constant PWM mode

The cathode filament heater as shown in Figure 2.1 is driven by un-rectified 50 Hz AC and has a great effect on the frequency spectrum of the magnetron RF output. Both the anode current and the heater power ripples modulate the frequency. The combined effect gives the RF output a spectral bandwidth as shown Figures 2.10 (a-e). The measurements for these figures were made with the switched mode power supply being operated in constant PWM mode. All snapshots on the left are traces from the spectrum analyser for differing heater powers and snapshots on the right are corresponding traces from the oscilloscope giving demodulated RF power output from the diode detector.

In Figures 2.10a and 2.10b corresponding to a heater powers of 54W and 42W there are large regular dips in power output (Note that the anode current is negative hence the zero is above the trace). At the high heater power of 54W the power dips occur at a regular

interval of about 24 μs which is probably linked to the chopper frequency. At the heater power of 42W, the power dips are less regular and not as deep but always occur when the anode current magnitude is smallest with respect to the 100 Hz ripple. The pattern of dips occurs on every other peak of the 100 Hz ripple and hence is probably tied to the highs of the barely visible 50 Hz heater power ripple. The diode output of Figure 2.10b suggests the dips are not only tied to the 100 Hz ripple but also to lows of the 43 kHz ripple. The spectra for these two high heater powers show large single sideband peaks below the centre frequency. The power dips disappear for heater powers at and below 40W. During this study we had insufficient time to analyse these dips. Speculating they could be due to moding or the magnetron turning itself off. Most of the work was undertaken at heater powers below 44W because this was the region where the best locking performance was obtained.

Numerical simulations by Karzhavin [10] indicate that the ratio of the cathode radius to the Brillouin hub radius has an important role to play in the process of noise generation. For a magnetron model with space charge limited emission and not including back bombardment and secondary emission he found that the charged spokes will have instabilities and cause random noise when the ratio $2\pi r_k/n : \pi r_c > 1$ where r_c is the unperturbed cycloid radius, r_k is the cathode radius and n is the number of spokes. When he considered back bombardment is conditional ratio for noisy operation became $\pi r_k/n : \pi r_c > 1$.

Figures 2.10 (a-e) show a reduction in fluctuating noise spectra as heater power is reduced. Brown's observations [9] support our observations as he points out that for a magnetron operating in the space charge limited mode (high heater power when there is presumably an excess of electrons) then high frequency noise and ripple present on high voltage supply has a much larger effect on anode current and the frequency spectrum. Brown also observes that if the cathode is operating in a temperature limited emission regime (small or no heater power), then any abrupt change in the high voltage applied to the magnetron, gives virtually no instantaneous increase in anode current. His explanation is that the anode current can only grow slowly in this regime as the final operating point at the new voltage is linked to the final cathode temperature; this temperature grows slowly with increasing back bombardment which is linked to increasing current. If however there is excess emission, then there will be an instantaneous increase in the anode current to a new operating point but this point is short of the final operating point where the remaining change requires an increased cathode temperature. This is Brown's explanation as to why very high level spurious sidebands are present when ripple and transients are present on the high voltage supply for space charge limited emission mode and why they are greatly reduced for temperature limited emission mode.

The 43 kHz ripple measured by the diode detector and shown explicitly in Figures 2.10a and 2.10b reduced slightly as the heater power is reduced from 42W to about 18W. In Figure 2.10d, when the heater power is at 30W, the random noise at about 1 MHz from the centre of frequency spectrum begins to take a discrete form with sidebands at 2^{nd} and 4^{th} harmonic of the chopper switching frequency (i.e. 96 kHz and 172 kHz). For heater power levels of 25W and 18W in Figures 2.10e and 2.10f respectively, the 2^{nd} harmonic

(96 kHz) becomes 20 dB smaller however 4^{th} harmonic (172 kHz) remains almost the same. Following Brown's observations [9] we identify the region between 30W and 18W is a transition zone between the space charge limited and temperature limited electron emissions from the cathode surface. Well within the temperature limited emission at 13W heater power, as shown in Figure 2.10g side bands at 4^{th} harmonic of the switching frequency (172 kHz) completely disappear. The remaining 2^{nd} harmonic sidebands have a further drastic reduction when the heater power is brought down to 9W as shown in Figure 2.10h. With further reduction in heater power to 6W and below shown in Figures 2.10i and 2.10j, these sidebands get lost at the noise floor of the Spectrum Analyser.

The 3 dB width of the frequency spectrum in Figures 2.10(a-i) is the combined effect of power supply ripples (i.e. 100 Hz, 43 kHz) and mains 50 Hz on the heater source. In Figure 2.10j the heater is completely turned off and we only see the effect of the power supply ripples. The spectral width when the heater is completely turned off is about four times less compared with when the heater is at its higher levels 36W – 54W. In Figure 2.9 we saw that on the power output the 100 Hz ripple was about 6 times bigger than 43 kHz ripple hence the 3 dB spectral width is determined by predominately the 100 Hz ripple whereas the 43 kHz gives a modulation to produce amplitude side bands well below 3 dB.

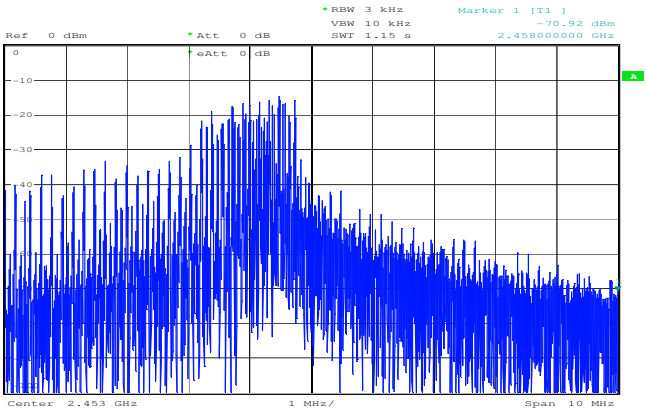

Magnetron output frequency spectrum

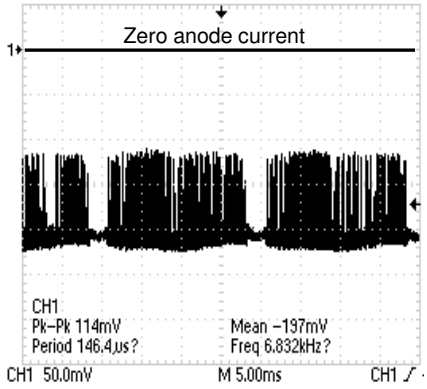

RF power output (5ms/div)

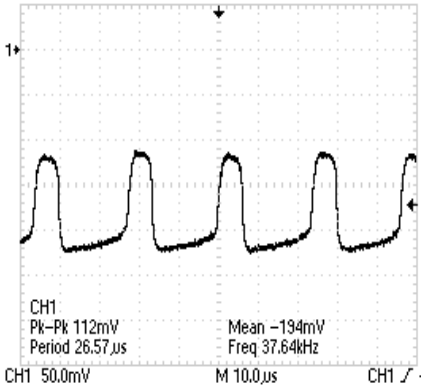

RF power output (10 µs/div)

showing high frequency noise.

Figure 2.10a Magnetron output through a 60dB loop coupler, on Spectrum Analyser (Left) and after a Diode Detector (Right) for **54W** Heater Power

Note: Power Supply is operated in constant PWM mode for all figures in Figure 2.10.

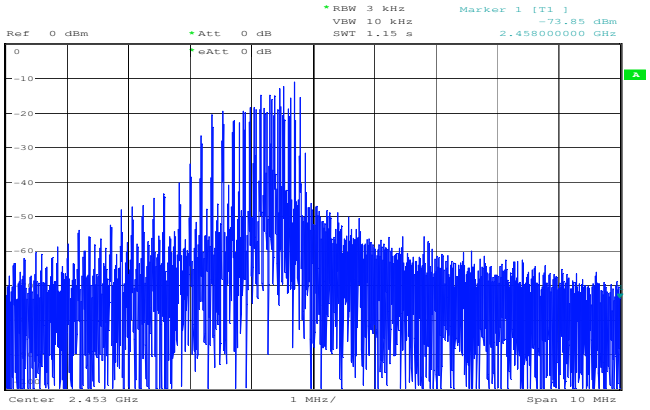

Magnetron output frequency spectrum

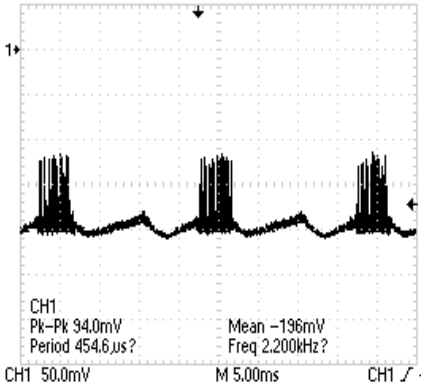

RF power output (5ms/div)

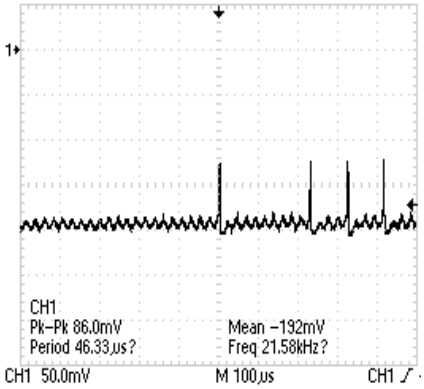

RF power output (100 µs/div) showing high frequency noise.

Figure 2.10b Magnetron output through 60dB loop coupler, on Spectrum Analyser (Left) and with Diode Detector (Right) for **42W** Heater Power

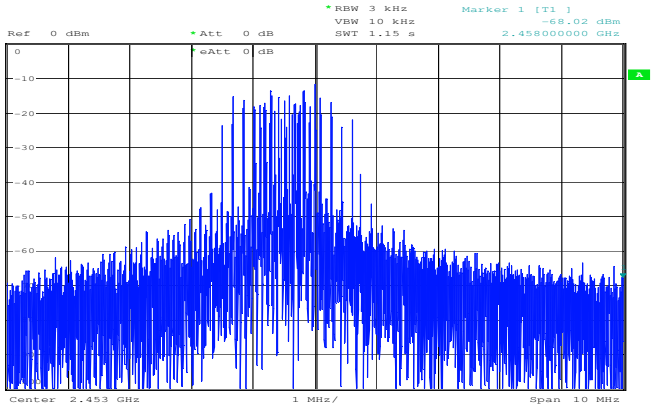

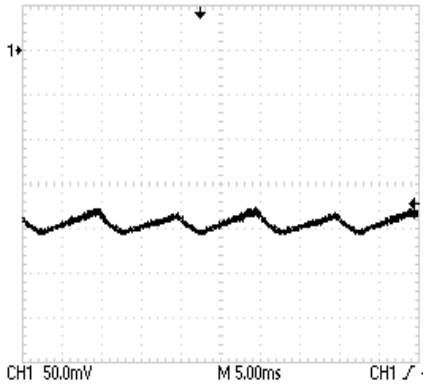

Magnetron output Frequency Spectrum RF power output

Figure 2.10c Magnetron output through a 60 dB loop coupler, on Spectrum Analyser (Left) and after a Diode Detector (Right) for **36W** Heater Power

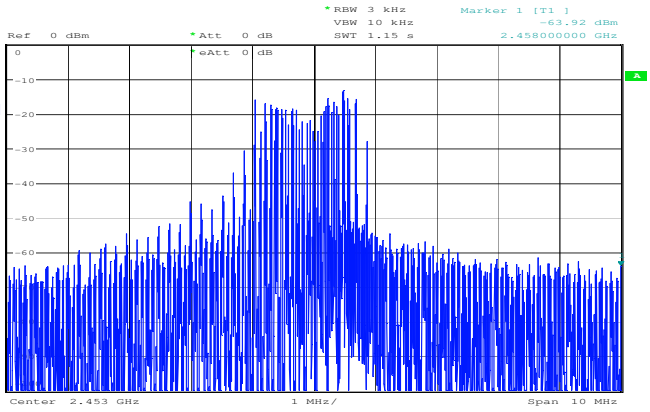

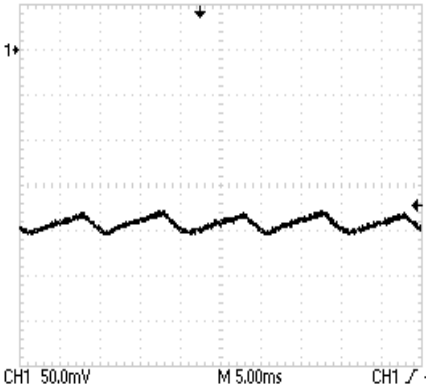

Magnetron output Frequency Spectrum RF power output

Figure 2.10d Magnetron output through a 60 dB loop coupler, on Spectrum Analyser (Left) and after a Diode Detector (Right) for **30W** Heater Power

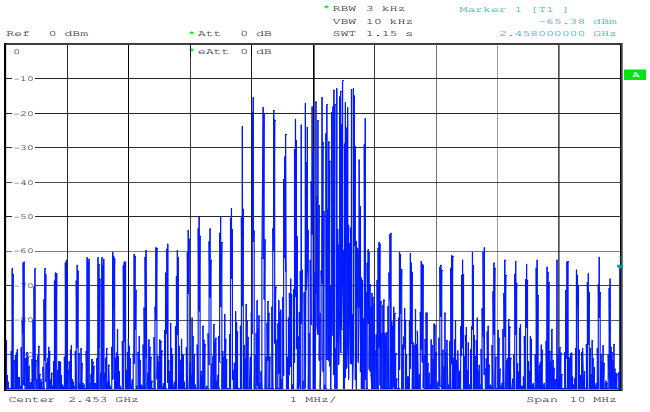

Magnetron output Frequency Spectrum

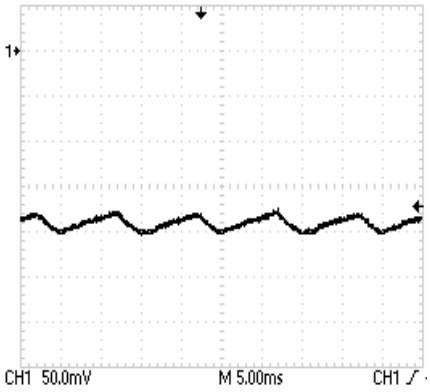

Magnetron Output through a Diode Detector

Figure 2.10e Magnetron output through a 60 dB loop coupler, on Spectrum Analyser (Left) and after a Diode Detector (Right) for **25W** Heater Power

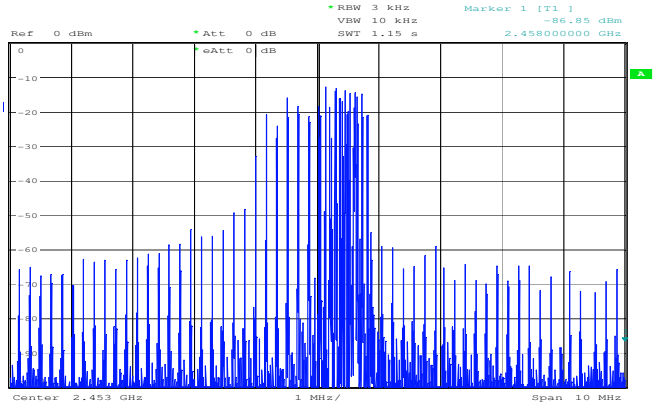

Magnetron output Frequency Spectrum

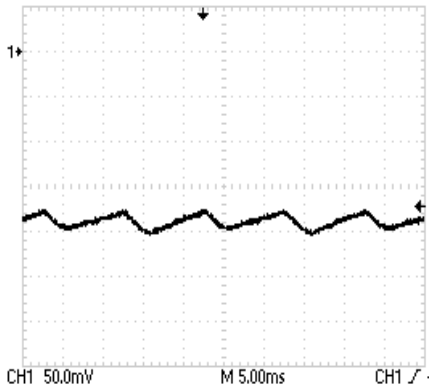

Magnetron Output through a Diode Detector

Figure 2.10f Magnetron output through a 60 dB loop coupler, on Spectrum Analyser (Left) and after a Diode Detector (Right) for **18W** Heater Power

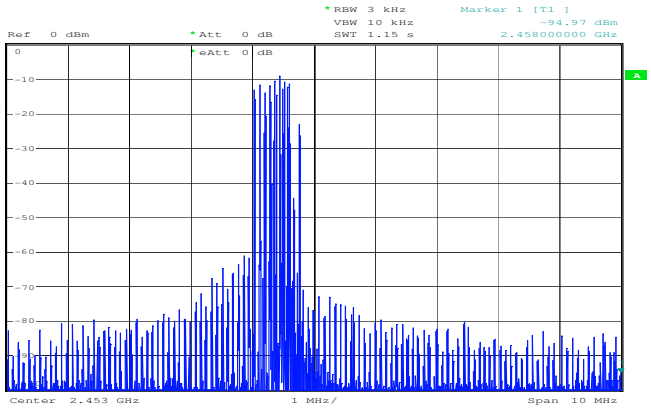

Magnetron output Frequency Spectrum

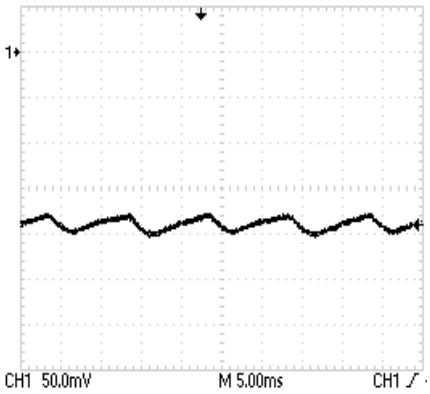

Magnetron Output through a Diode Detector

Figure 2.10g Magnetron output through a 60 dB loop coupler, on Spectrum Analyser (Left) and after a Diode Detector (Right) for **13W** Heater Power

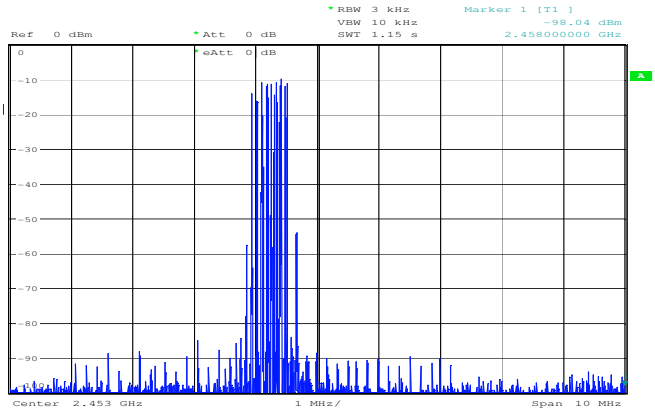

Magnetron output Frequency Spectrum

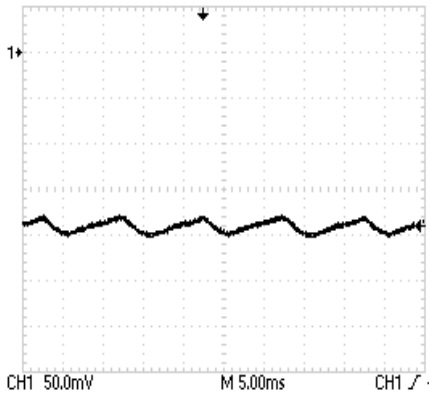

Magnetron Output through a Diode Detector

Figure 2.10h Magnetron output through a 60 dB loop coupler, on Spectrum Analyser (Left) and after a Diode Detector (Right) for **9W** Heater Power

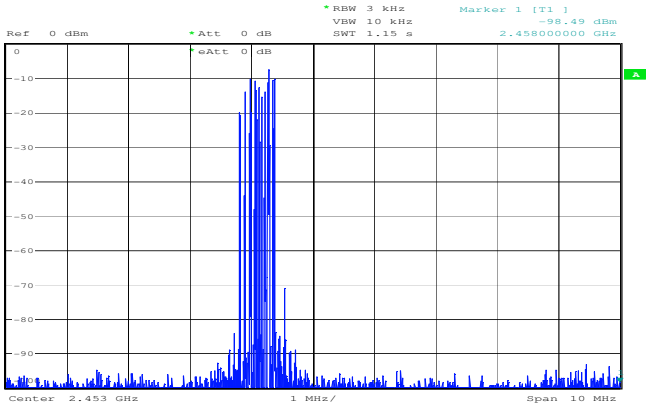

Magnetron output Frequency Spectrum

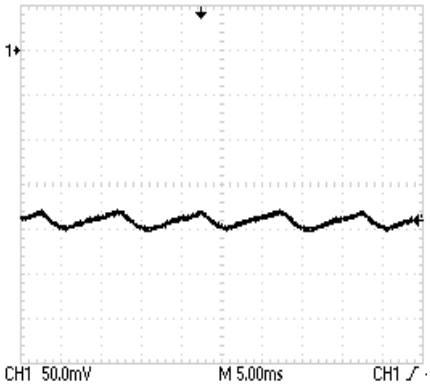

Magnetron Output through a Diode Detector

Figure 2.10i Magnetron output through a 60 dB loop coupler, on Spectrum Analyser (Left) and after a Diode Detector (Right) for **6W** Heater Power

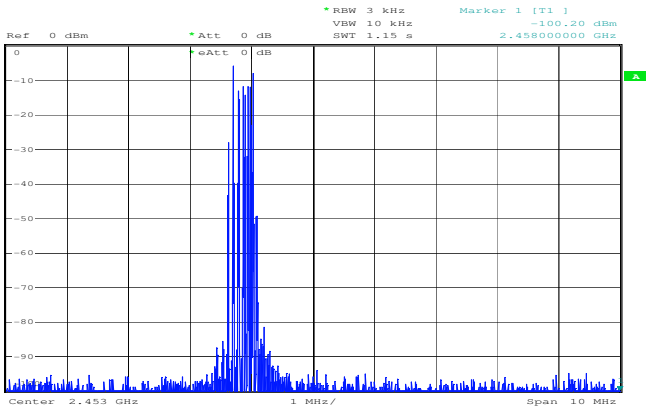

Magnetron output Frequency Spectrum

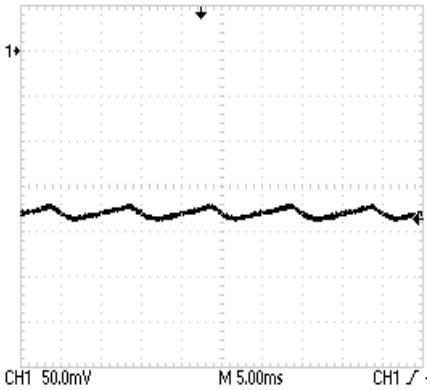

Magnetron Output through a Diode Detector

Figure 2.10j Magnetron output through a 60 dB loop coupler, on Spectrum Analyser (Left) and after a Diode Detector (Right) for **0W** Heater Power

In constant PWM mode, reducing the heater power gives a small reduction in anode current, Figure 2.11 shows this dependency. As the dependency is small it was not completely apparent in Figure 2.10 (a-j). The result is not too surprising as one expects anode current to depend on the availability of electrons emitted from the cathode. The corresponding change in the frequency is shown in Figure 2.12.

This is not what one would immediately expect from the pushing curve. The pushing curve gives monotonically increasing frequency with anode current to at least 400 mA. Figure 2.11 gives increasing anode current with heater power hence in figure 2.12 we might have expected monotonically increasing frequency with heater power. Instead for the space charge limited emission region (high heater power) the frequency decreases with an increase in anode current for currents well below 400 mA. This means that the magnetron output frequency has a dependency on the heater power as well. A plausible explanation for this frequency dependency when the heater power is high (25-54W) could be a reduction in the Brillouin hub radius with a reduction in the heater power. Consequently with reference to the equivalent circuit in Figure 1.5, the capacitance between the hub and the anode decreases and the frequency increases. This increase in frequency is greater than the decrease in the frequency expected from the pushing curves when the anode current decreases due to a reduction in the heater power. For heater powers below 25W although the frequency decreases with decreasing heater power, it is difficult to say whether the net change in frequency is due to the reduction in anode current alone or if there is a significant heater power dependency. This uncertainty was resolved by operating the switched mode power supply in constant current mode so that the anode current stays constant when the heater power is varied.

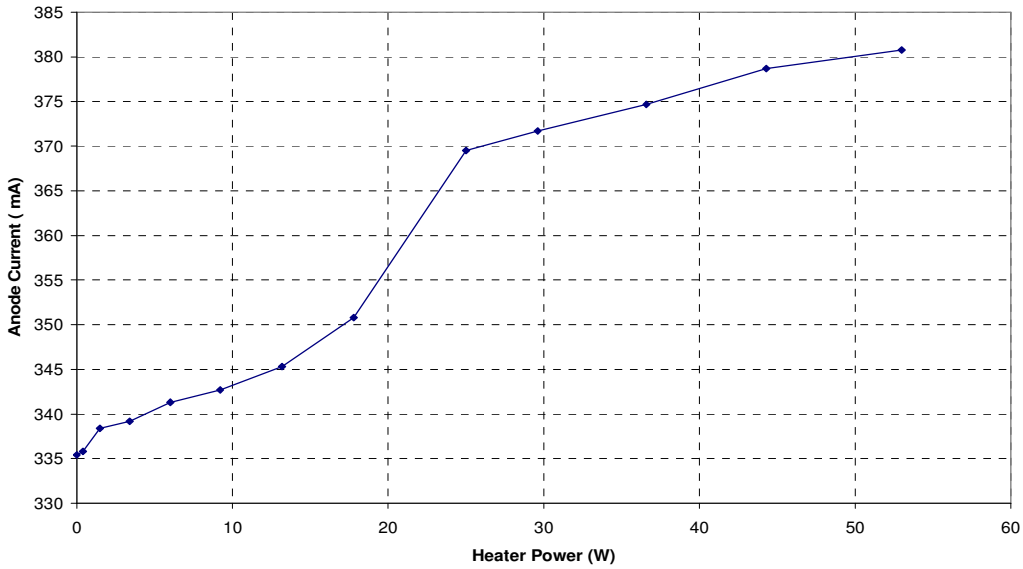

Figure 2.11 Change in Anode Current with respect to change in heater power, constant PWM mode.

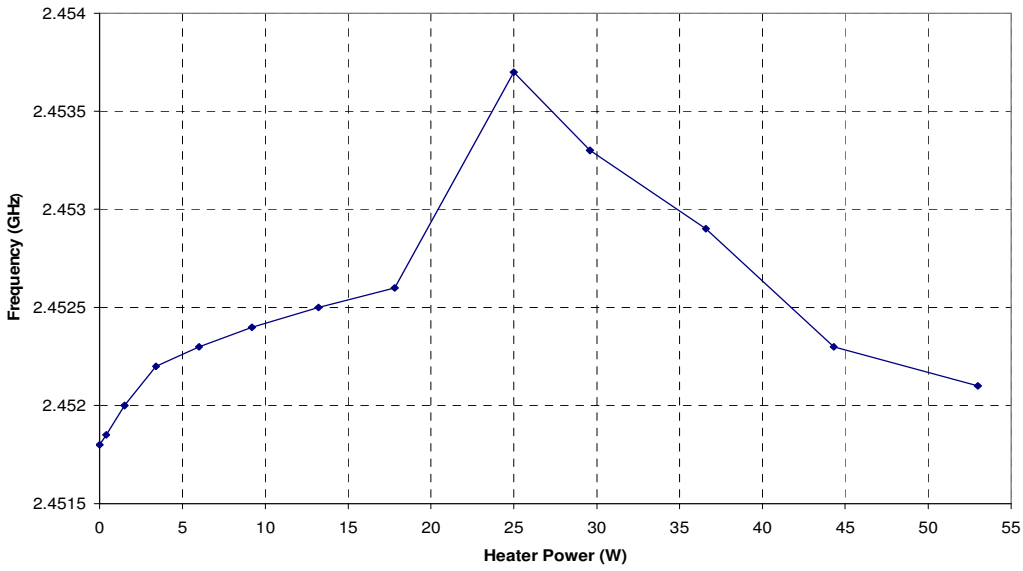

Figure 2.12 Effect of heater power on magnetron frequency (constant PWM)

2.6 Effect of heater power on the frequency spectrum in constant current mode

A functional diagram for switched mode power supply operation with current feedback control is shown in Figure 2.1. The anode current measured across the resistor R is compared with a set voltage reference using an op-amp voltage comparator. The error signal from the voltage comparator is fed to a loop filter which the controls the PWM IC input voltage keeping the anode current at the set level. The frequency spectra obtained with constant anode current of 305 mA are shown in the twelve screen shots of Figure 2.13. The effect of anode current ripple is negligible (~ 0.65 %) in this case because the current feedback loop is able to reduce the ripple by a factor of 20. Increasing the heater power from zero to 15W the spectral bandwidth gradually increases with sidebands appearing below initial peak at 2.4530 GHz (the peak also shifts slightly). At a power level between 15W and 18W there is sudden increase in the bandwidth. This large bandwidth is unchanged in the heater power range of 18W to 30W. Between 30W and 33W of heater power there is a sudden decrease in bandwidth. At 33W the bandwidth is similar to that at 12W, but with increased sidebands.

In the frequency spectrum for 15W heater power, two peaks start to appear in the frequency spectrum and these remain up to a heater power of 30W. Below a heater power of 15W we are probably safe to assume that we have temperature limited emission enhanced by back bombardment and above 30W of heater power we are probably safe to assume we have space charge limited emission. We notice that for low heater powers below 15W the is an apparent frequency peak near to 2.4530 GHz

and for high heater powers near to 33W the peak spectral output is centred at a lower frequency of 2.4518 GHz. Between 18W and 30W of heater power the output spectra show both the low heater power peak and the high heater power (33W) peak. The spectral shape between 18W and 30W suggests that magnetron switches between these two frequencies and is indicative of an unstable operating region between temperature limited emission and space charge limited emission. We will refer to this region as the region of instability throughout the remainder of this thesis. At the mid-range anode current (200mA, half the maximum anode current) and very high anode current (maximum 400mA) this region of instability is relatively small and exists between 25W - 30W of heater power only.

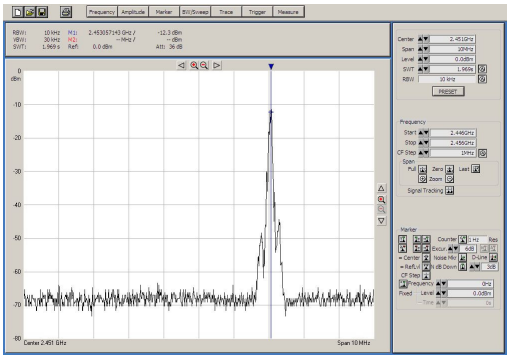

0W

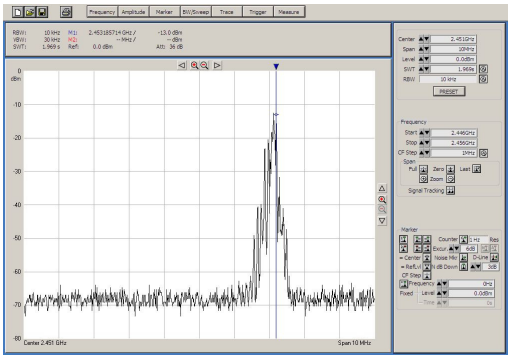

9W

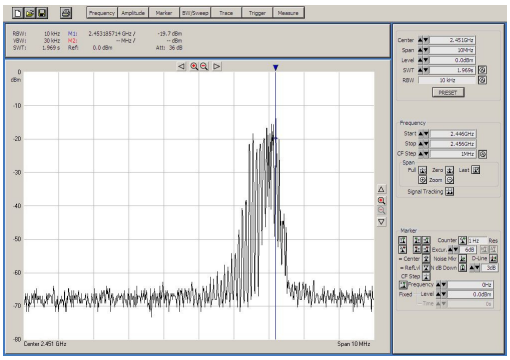

12W

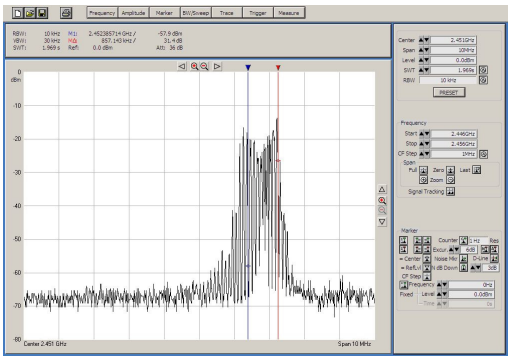

15W

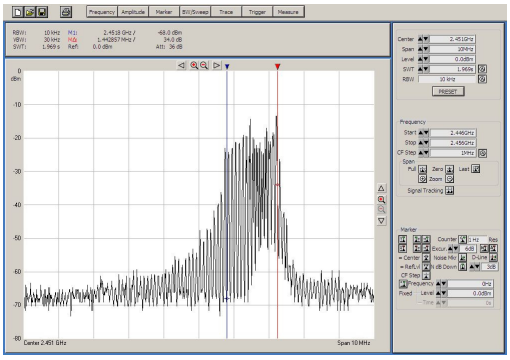

18W

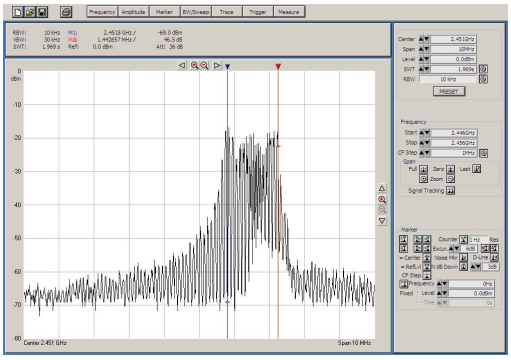

21W

Figure 2.13 Magnetron output spectra with constant anode current for different heater power levels {SPAN: 10 MHz (1 MHz/Div) RBW: 10 kHz}

(Figure 2.13 Continued)

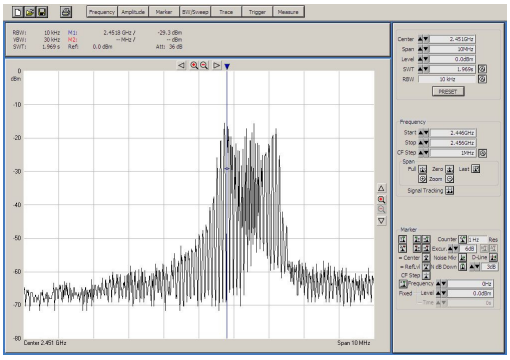

25W

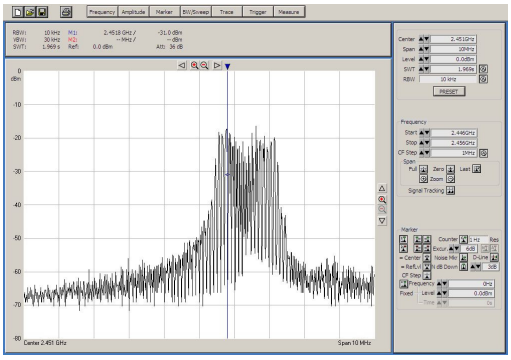

27W

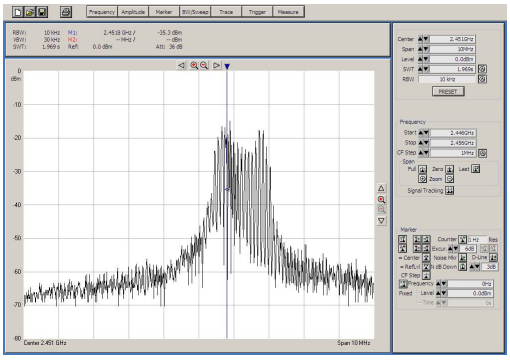

30W

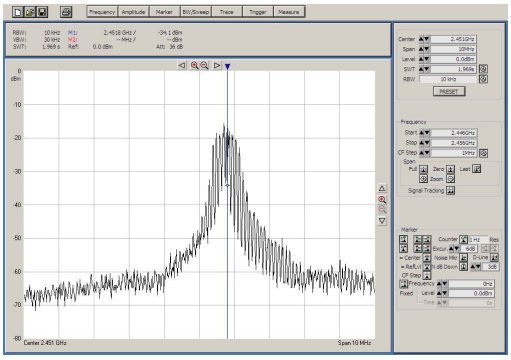

33W

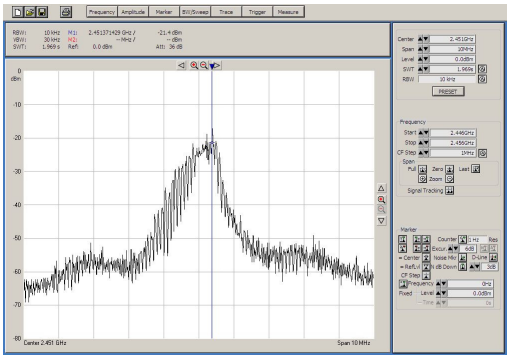

44W

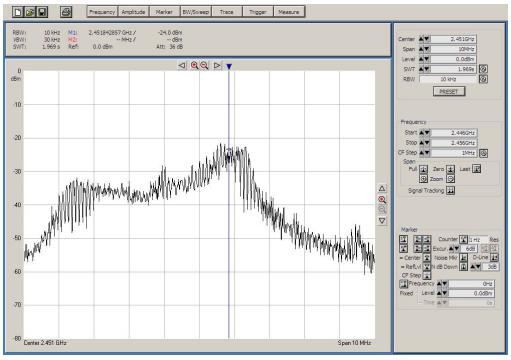

52W

Figure 2.13 Magnetron output spectra with constant anode current for different heater powers {SPAN: 10 MHz (1 MHz/Div) RBW: 10 kHz}

This behaviour of frequency shift with heater power is summarised in Figure 2.14a and 2.14b for different anode currents when the power supply is operated in constant current mode. The figures plot the centre frequency of the 3 dB band against heater power. Figure 2.14b is the same as Figure 2.14a but with different scale to adjust the added plot for 105mA.

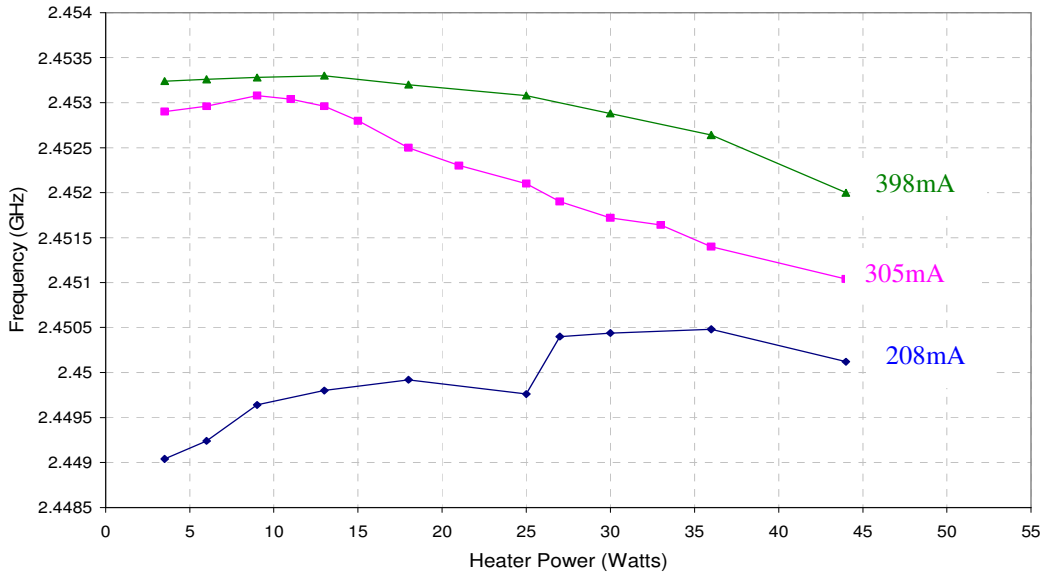

Figure 2.14a Magnetron frequency vs. heater Power (Constant Anode Current)

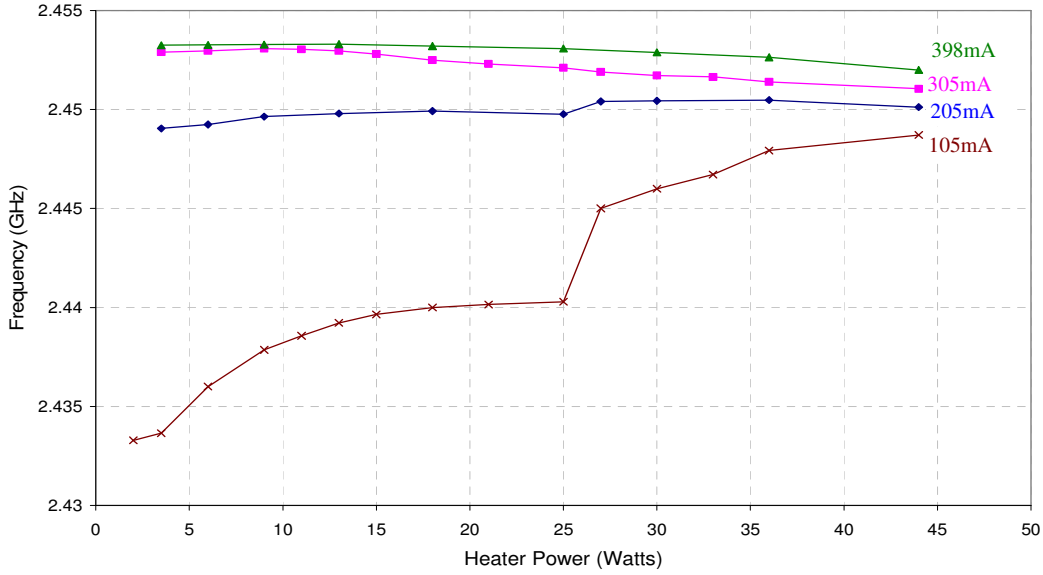

Figure 2.14b Same as Figure 2.14a with an added Plot at 105mA and zoomed out

Shown in the Figure 2.14, the magnetron has a different response to the change in heater power at higher anode current (above 250 mA) compared with low anode current (below 250 mA). This dependency on the anode current may be explained by Brown's suggestion [7], that reducing the heater power shifts the space charge spokes in such a way so that the back bombardment increases in order to supply the necessary amount of electrons to sustain the oscillations.

Reducing the heater power reduces the space charge hub radius as described earlier in this section, thus the total cathode to anode capacitance decreases and frequency of the magnetron output increases. This effect is lot more pronounced at very low anode currents as shown by the curve at 105mA in the Figure 2.14b. As the anode current is held constant by the feedback loop, an increase in anode voltage is observed when the heater is turned down. The total increase in voltage as the heater power is reduced from 52W to zero, is about 200V for 205 mA anode current, and 100V for 398 mA anode current.

2.7 Heater power effect on the magnetron efficiency

A drop in electronic efficiency (where electronic efficiency is defined here as r.m.s. RF power output divided by the product of r.m.s. anode current and voltage) of about 6% is observed when the heater is turned down from its maximum to zero. The overall efficiency (whose definition additional includes input power to the filament heater) is reduced by just 3%. Efficiency plots are shown in Figure 2.15 for an average of

300mA anode current and are obtained with power supply operated in constant PWM mode.

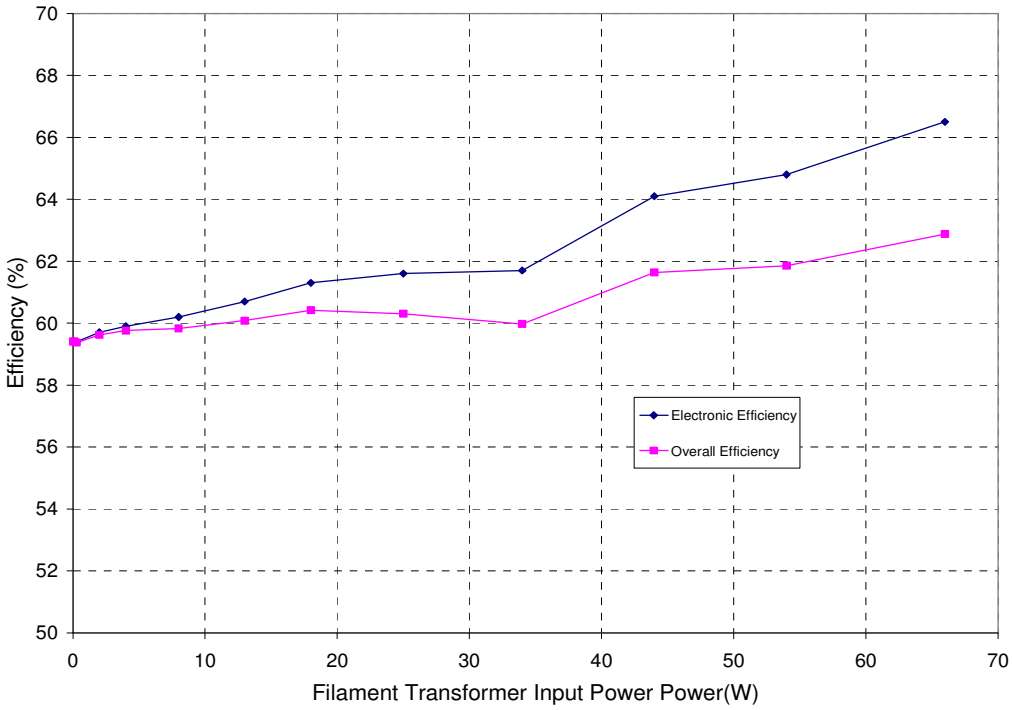

Figure 2.15 Efficiency plotted against heater power (constant PWM)

2.8 Anode temperature and Frequency

Most of the efficiency loss is due to heating of the anode as electrons strike the inner surfaces of the vanes. Also small portion of energy is lost in the cathode heating due to back bombardment. Anode heating causes the cavities to expand and frequency to fall. The relationship between anode temperature and frequency has been measured and the results are given in Figure 2.16. This figure was obtained by operating the magnetron with a constant anode current of 330mA and recording the frequency as the magnetron anode heated up from the room temperature. The temperature

measurement was made at the outer surface of the anode. The anode is a solid copper block hence a measurement on the outer surface is representative of the bulk. On average we see a frequency drop of 40 kHz for a 1^{o}C temperature rise.

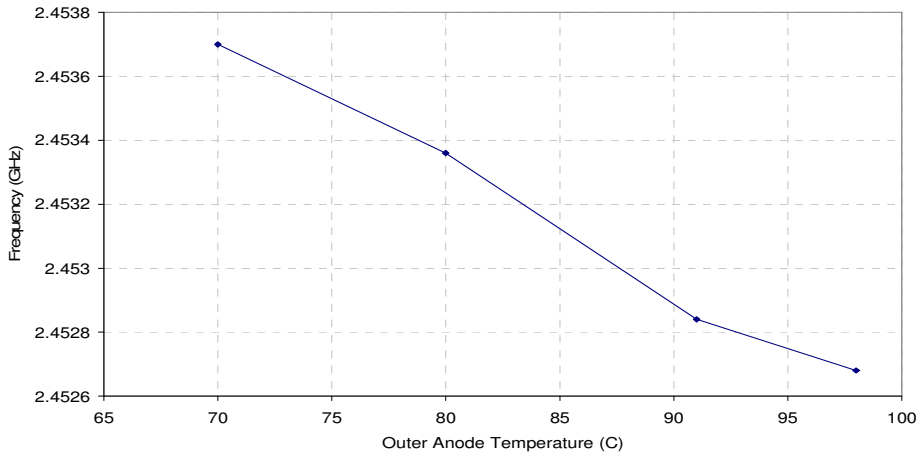

Figure 2.16 Frequency as a function of outer anode surface temperature at constant anode current of 330mA.

The magnetron's pushing response provides the fastest opportunity for changing its output frequency. By controlling the anode current, the frequency can be held constant against other influences which tend to change it, e.g. load, anode temperature, heater power ripple and ripple on the anode current itself. Our technique for achieving frequency stability using recent advances in digital frequency synthesis technology [46] is discussed in next chapter.

CHAPTER 3

DIGITAL PHASE LOCKED LOOP IMPLEMENTATION FOR THE MAGNETRON

As described in detail in Chapter 2, the frequency of the magnetron RF output is affected by all the input parameters, i.e. the anode voltage, the anode current, the cathode heater power, the load, the anode temperature and the magnetic field across the tube. Any of the above parameters can be used in a negative feedback loop in order to stabilise the frequency. How good the frequency stability would be, remains dependent primarily upon the speed at which the chosen parameter can respond to a change in the frequency.

Brown [8] has demonstrated phase locked magnetron operation with frequency stabilisation plus injection locking. He used a small electromagnet along with the main magnetic field in order to vary the anode current in such a way as to minimise variation of the magnetron's natural frequency. When the magnetic field changes, the anode current changes and the operating point moves to a differing position on the pushing curve. Negative feedback stabilises the natural frequency and hence the phase shift between the injection signal and the magnetron output. The method was only demonstrated in conjunction with the injection locking. Changing current in an electromagnet's windings

typically has a poorer time response than direct anode current variation (due to the smaller inductance) hence we chose not to pursue Brown's method.

Frequency stabilisation is also possible by variation of the load. This can be achieved using motorised tuning stubs in the output waveguide so as to use the pulling characteristic. Mechanical tuner adjustment has a slower time response than anode current adjustment using a switched mode power supply.

The cathode heater power can also be used for the frequency control, but it has relatively less effect on the frequency. Moreover as it floats at high negative voltage -4000V DC for our magnetron, it is normally powered by AC through an isolation transformer. In order to use the cathode heater for control it would need a controllable DC supply that floats at the HT voltage.

In early 90s improvements in MOSFET and IGBT structures allowed the production of low cost, high power, high voltage switched-mode power supplies (with high switching frequencies) for different applications. One such application was magnetron power supplies for industrial heating systems, a block diagram for which is shown in Figure 2.1. This power supply topology allows control of the high output voltage (~ 4 kV and above) with a small voltage (~ 3V) applied to the PWM IC input. Implementation of anode current feedback control became straight forward and now provides stable and controllable microwave power for many industrial applications. The high switching frequency (typically 43 kHz at 2 kW output) makes rapid change of the anode current possible and hence use of the pushing characteristic for frequency control straightforward.

One such implementation was proposed by N. Sinohara *et al* in August 2003 [24]. He used a double balanced mixer to measure phase error with respect to a reference signal for an injection locked magnetron and then used a PC based controller to minimise it by varying the anode current through a satellite grade very stable power supply. The published paper [24] does not describe any details of the hardware implementation and analysis of the control performance.

A novel way of implementing the idea of controlling the magnetron frequency through its anode current is presented in this thesis using a 'Phase Locked Loop Synthesizer' Integrated Chip (IC). This IC is normally used in handheld transceivers such as mobile phones and is very low in cost, highly integrated and available off the shelf from many IC manufacturers.

3.1 Frequency feedback circuitry and experimental setup

The technique used for magnetron frequency control is similar to the frequency synthesis method for local oscillators in wireless communication applications. In this method, the output frequency of a voltage controlled oscillator (VCO) is divided down to the channel step size (or channel bandwidth) and a digital phase frequency detector compares it with a reference signal which is also at the same frequency. The error signal is filtered by a low pass filter which also sets the loop gain and phase shift and is used to control the VCO frequency. The associated block diagram is shown in Figure 3.1.

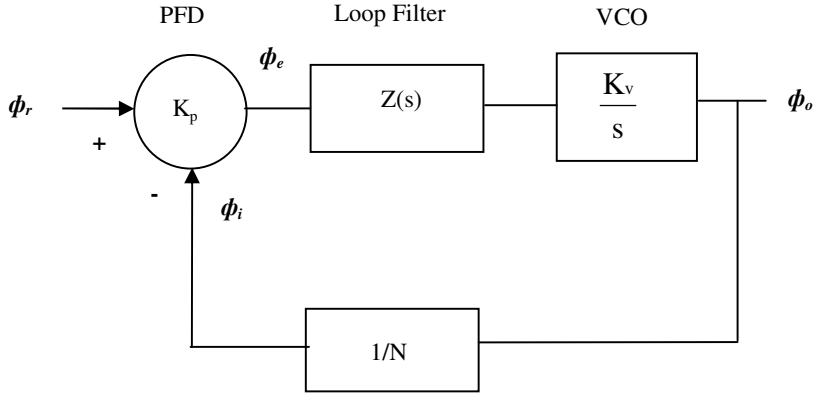

Figure 3.1 Block Diagram of a Digital PLL Circuit

Input /Output relationships for this circuit can be obtained as follows:

$$\text{Forward Loop Gain} = G(s) = \frac{\phi_o}{\phi_e} = K_p K_v \frac{Z(s)}{s} \tag{3.1}$$

$$\text{Reverse loop Gain} = H(s) = \frac{\phi_i}{\phi_o} = \frac{1}{N} \tag{3.2}$$

$$\text{Open Loop gain} = H(s) \cdot G(s) = \frac{\phi_i}{\phi_e} = K_p K_v \frac{Z(s)}{Ns} \tag{3.3}$$

$$\text{Closed loop gain} = \frac{\phi_o}{\phi_r} = \frac{G(s)}{1 + G(s)H(s)} = \frac{K_p K_v Z(s)}{s + \frac{K_p K_v}{N} Z(s)} \tag{3.4}$$

Due to an increased demand of light weight and small size in handheld wireless devices, the frequency dividers and the digital phase detector are now integrated in one package by IC manufacturers. One such IC is ADF4113 from Analog Devices was selected for this research. The functional diagram for this device is shown in Figure 3.2 and its internal

architecture in Figure 3.3. It principally consists of two programmable frequency dividers, a digital phase frequency detector (PFD) and a charge pump. The frequency dividers divide both the RF and the reference input down to the required step size of the RF output frequency. The frequency step size of 200 kHz is chosen for this research, as it gives an appropriate number of points on the pushing curve.

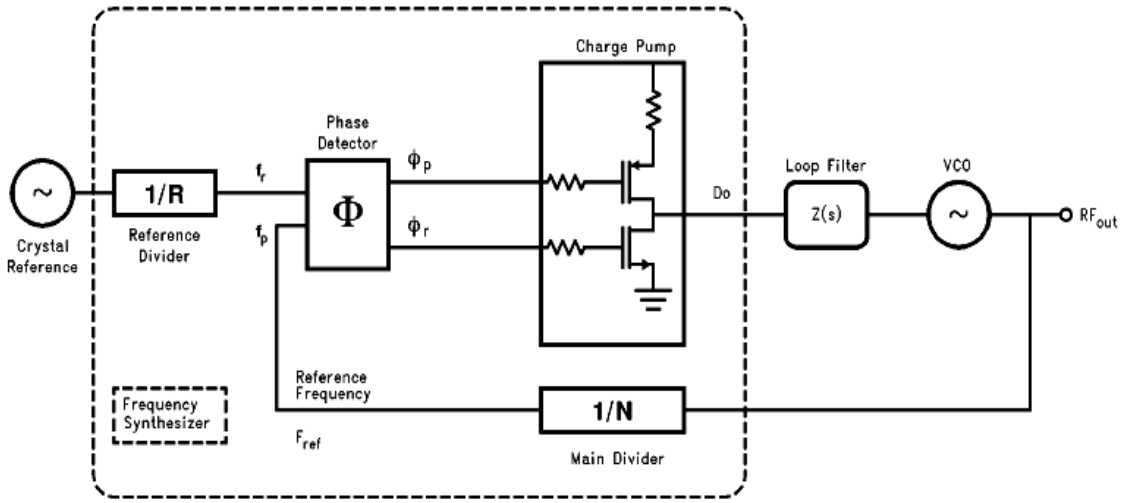

Figure 3.2 Functional Block Diagram of a PLL (From National Application note 1001 [43])

A maximum reference frequency of 50MHz can be applied to the reference input. The Reference Counter/divider has a division ratio from 1 to 16383. The maximum RF input at which the RF input dividers in the IC can work is 4GHz. There are two frequency counters/dividers for the RF input, namely Counter A and Counter B as shown in Figure 3.3. Counter A gives a division ratio of 1 to 63 and Counter B can divide by 3 to 8191. A suitable combination of these two counters can be used to achieve a division ratio anywhere between 3 and 516033. A reference oscillator of 10MHz and a division ratio of

50 from the Reference Counter are used to achieve 200 kHz clock at the reference input of the PFD. The RF input frequency is divided down to 200 kHz by the formula:

$$f_{RF} = [(P \times B) + A] f_{REF} / R \qquad (3.5)$$

Where P is the Pre-scalar divider, operating at CML (Current Mode Logic) level which divides the RF input down to a manageable frequency for the CMOS A and B counters [46]. The value of P can be set to 8, 16, 32 or 64 through programming.

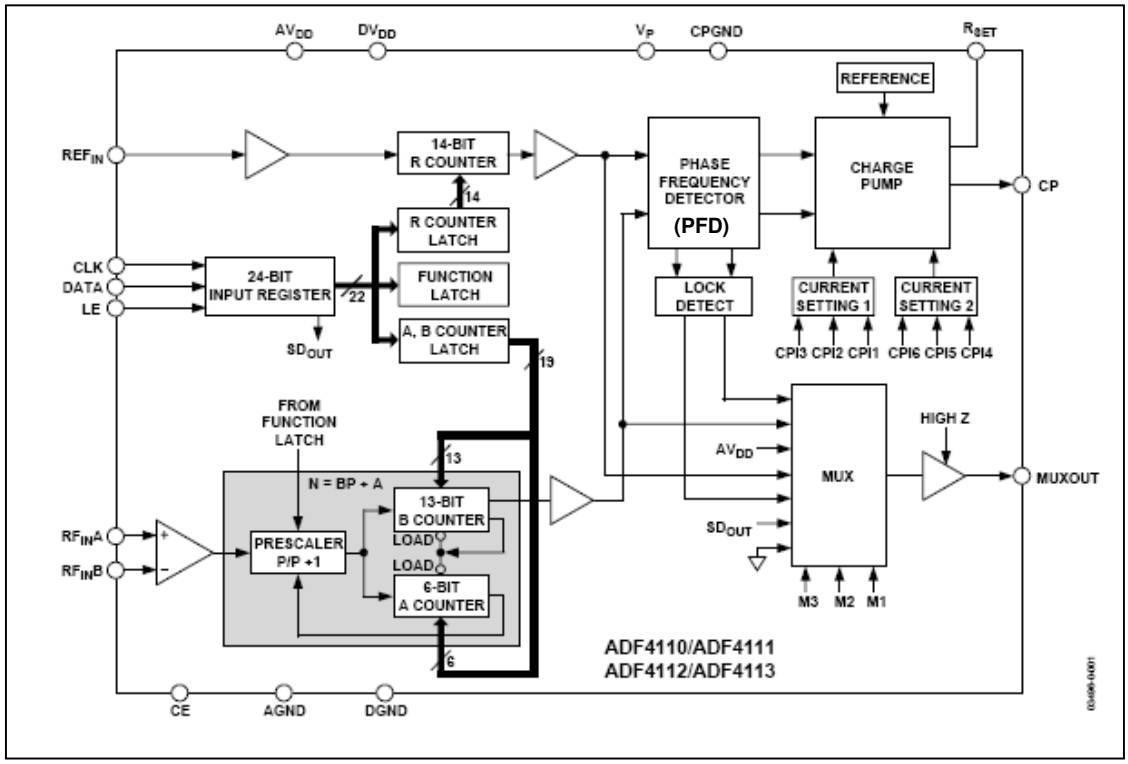

Figure 3.3 Internal Architecture of ADF4113 (Device datasheet [44])

A microcontroller from Atmel AT89c4051 is used to program the desired division ratios into a 24-bit register which further programs the counter latches. The division ratios once programmed are held by the latches, until the new values are updated by the

microcontroller when a change in frequency is required. The PFD in Figure 3.3 compares the time difference between the two pulses and generates an output pulse proportional to this time difference. Figure 3.4 shows the specific implementation of the PFD (left) and the charge pump (right) that were shown in outline in figure 3.3. The switching logic for the PFD is shown in the bottom trace of Figure 3.4.

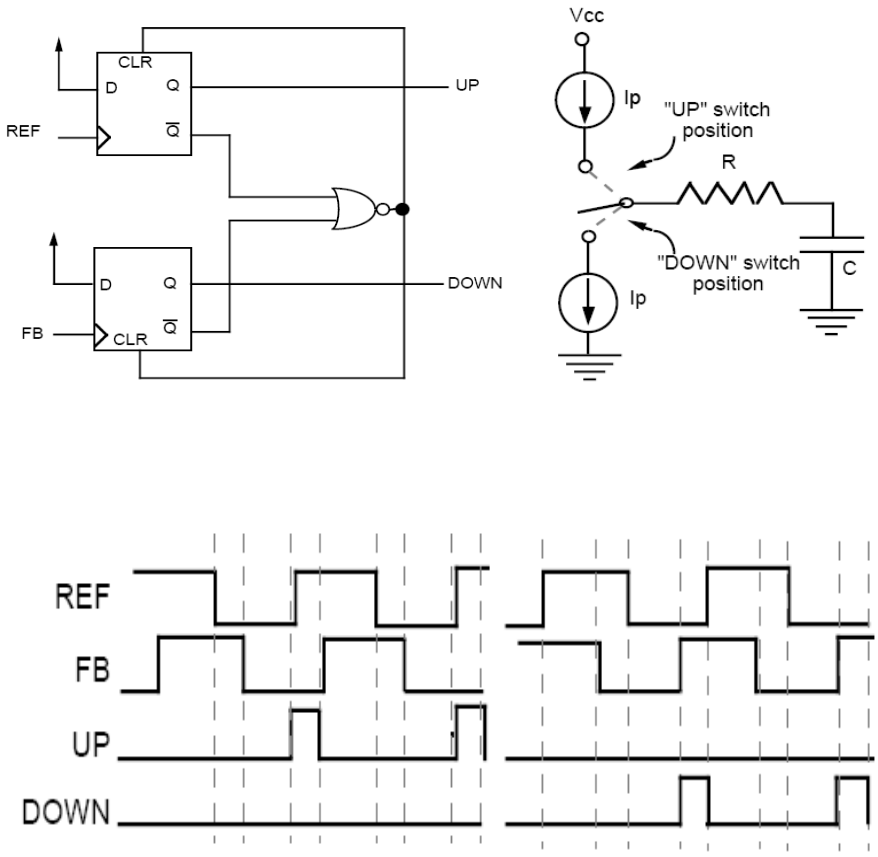

Figure 3.4 PFD and charge pump configuration and operation (AN_155 from Integrated Device Technology, Inc [45])

If the Reference signal leads the RF feedback signal, pulses appears at the flip-flop output labelled as 'UP' in Figure 3.4. The 'Up switch' closes and the capacitor C in Figure 3.4 charges from the power supply Vcc. The pulse width (ON time) determines the charge that is added to the capacitor.

If the RF feedback leads the reference, then the output described as 'Down' carries the pulse. In this case the 'Down switch' closes and the capacitor C discharges to ground [45]. The pulse width (ON time) determines the charge that is subtracted from the capacitor. The resistance R represents the intrinsic resistance of the switch. The capacitance C is added externally, it might be regarded as part of the loop filter and is often referred to as the integrating capacitance. The chip manufacture tries to keep the resistance R as small as possible to give the best frequency response.

The capacitance C is followed by a low pass filter which allows adjustment of the closed loop parameters, in order to achieve the best possible performance. The integrating capacitor and the low pass filter, together are also known as a loop filter. In a standard frequency synthesised local oscillator system, there is a VCO after the loop filter. However in our experimental setup, the loop filter output goes to the control input of the Magnetron power supply. Thus from the perspective of a frequency synthesiser system, the power supply and the magnetron together can be treated as a VCO, and will be called a *Voltage Controlled Magnetron Oscillator (VCMO)* in this thesis in order to distinguish from the term VCO.

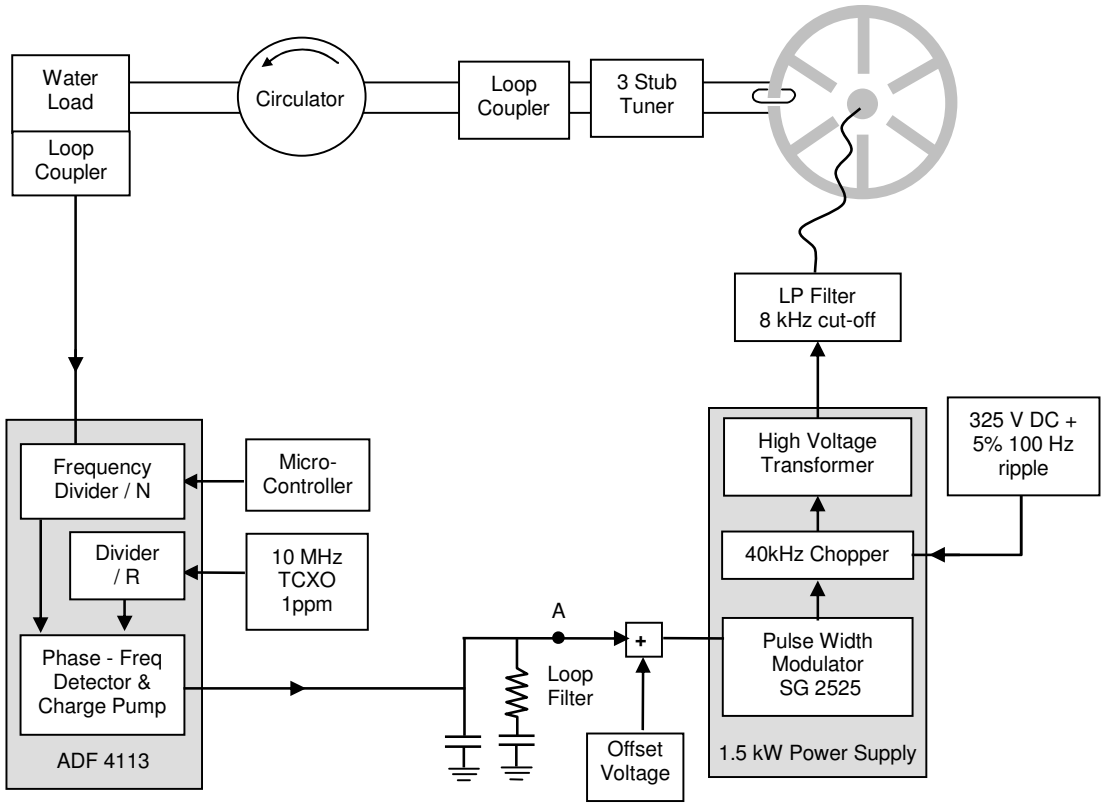

Figure 3.5 Frequency Feedback control implementation with ADF4113

The experimental setup for phase/frequency locking of the magnetron with ADF4113 is shown in figure 3.5. An offset voltage is added to the control input as shown in Figure 3.5 so that the magnetron starts with 100mA anode current when the power supply is turned on. This offset voltage is necessary for the frequency feedback control to work because an initial frequency has to be present at the RF input of ADF4113 for the phase detector to begin its operation. An anode current of the order of 100mA is chosen because the magnetron 2M137 is unstable for an anode current below 70mA. A detailed circuit

diagram of the control input circuit that we designed and built can be found in Appendix II, Figure AII.7.

3.2 Loop Filter design

The loop filter design is at the heart of the magnetron frequency control implementation. Figure 3.9 re-draws the key components of the loop filter. In order to determine the values for the loop filter components, the frequency sensitivity of the VCMO to its control input is required. A variable voltage source was applied at the control input of the power supply with the loop filter disconnected at the point marked A in Figure 3.5. Anode current is plotted against the control voltage V_c in Figure 3.6 for two heater power levels, 10W and 40W. For these measurements a small amount of reflected power to the magnetron was set to bring the pushing curves take an intermediate slope with respect to the likely range of operation. The pushing curves for the two heater powers are presented in Figure 3.7. Combining the data from Figure 3.6 and Figure 3.7, we get the *frequency sensitivity curves* for the two heater power levels and at the chosen level of reflection, as shown in Figure 3.8.

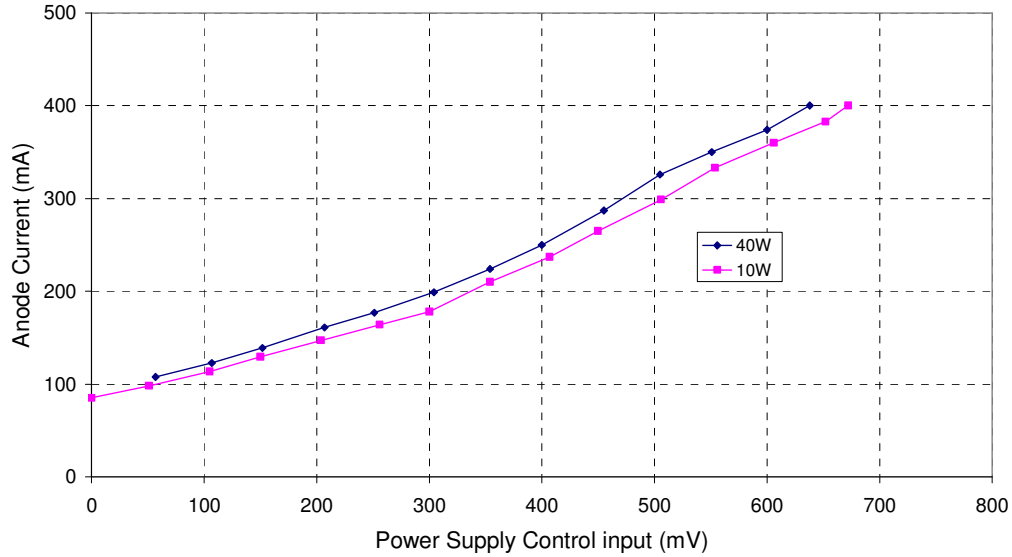

Figure 3.6 Anode Current vs. Power Supply Control input (DC)

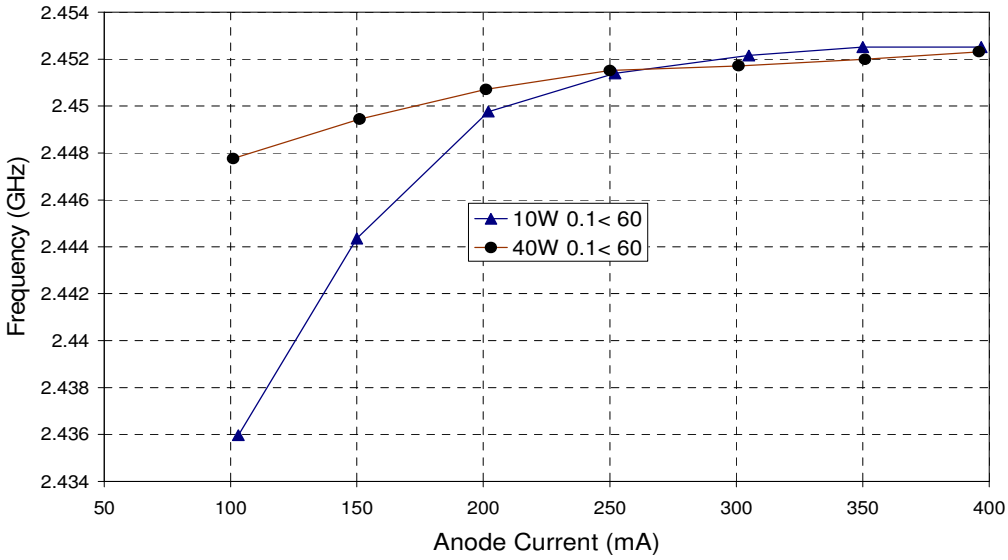

Figure 3.7 Pushing Curves for 10W and 40W Heater Powers with 10% reflected power at a phase of 60^{o}

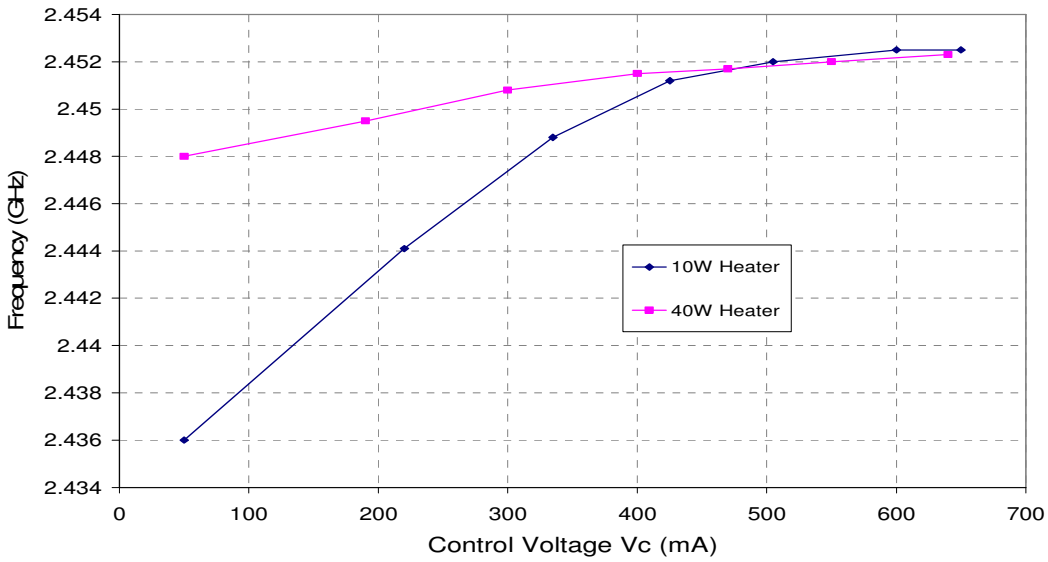

Figure 3.8 Frequency Sensitivity of Voltage Controlled Magnetron Oscillator (Power Supply+ Magnetron' as a VCO), where the power supply's control input is a DC voltage.

A large variation in pushing curve slope is seen for 10W heater power. We have a maximum slope of 28MHz/V for an input control voltage V_c from 50mV to 350mV and a minimum slope of 10MHz/V for V_c from 350mV to 600mV. The curve for 40W heater power has minimal slope variation and the slope is about 6MHz/V. Each pushing curve slope demands different loop filter component values for an optimum performance. Whilst it might be possible to switch between differing filters or differing current levels from the Phase Frequency Detector output for simplicity a compromise between performance and ease of operation was achieved with fixed loop filter component values designed for an average slope of 14 MHz/V. The detailed loop filter design is presented in the Appendix II. The parameters used for the loop filter design are:

VCMO sensitivity = K_v = 14MHz/V

PFD Constant = K_p = 2.5mA

RF Division Ratio = N = $\frac{2.45\text{GHz}}{200\text{KHz}}$ = 12250

Damping factor = 0.707 (for critically damped operation)

The loop filter with component values from Appendix II is shown in Figure 3.9.

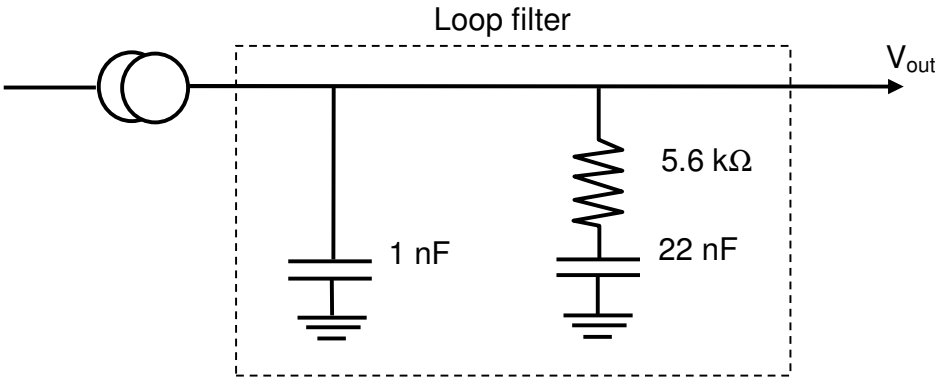

Figure 3.9 Second order loop filter for the charge pump PFD

3.3 AC Response of the power supply and feedback loop stability

AC response curves for gain and phase of the switched power supply are needed for analysing the feedback loop stability and its performance with the designed loop filter. The AC gain of the switched power supply is determined by applying a sinusoidal signal at the control input (point A as before). The frequency of the signal is varied and peak to peak values of the anode current through the magnetron are recorded. (Note that the response of the magnetron is orders of magnitude faster than the switched mode power supply). The AC gain (I_a/V_c) is plotted against the control input frequency in Figure 3.10,

for two heater powers 10 and 40W. The phase response (delay) introduced by the power supply vs. the input frequency of control voltage V_c is shown in Figure 3.11.

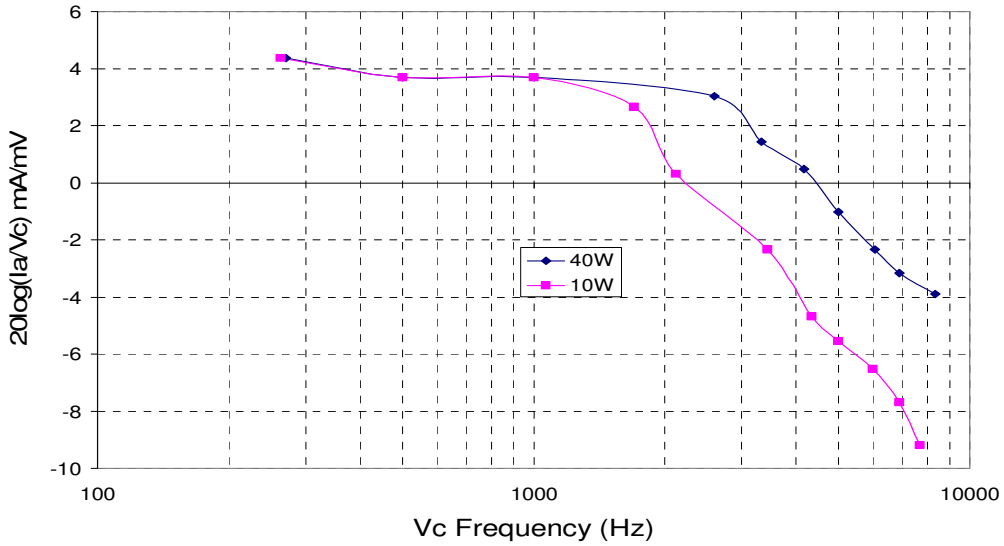

Figure 3.10 Power supply AC Gain

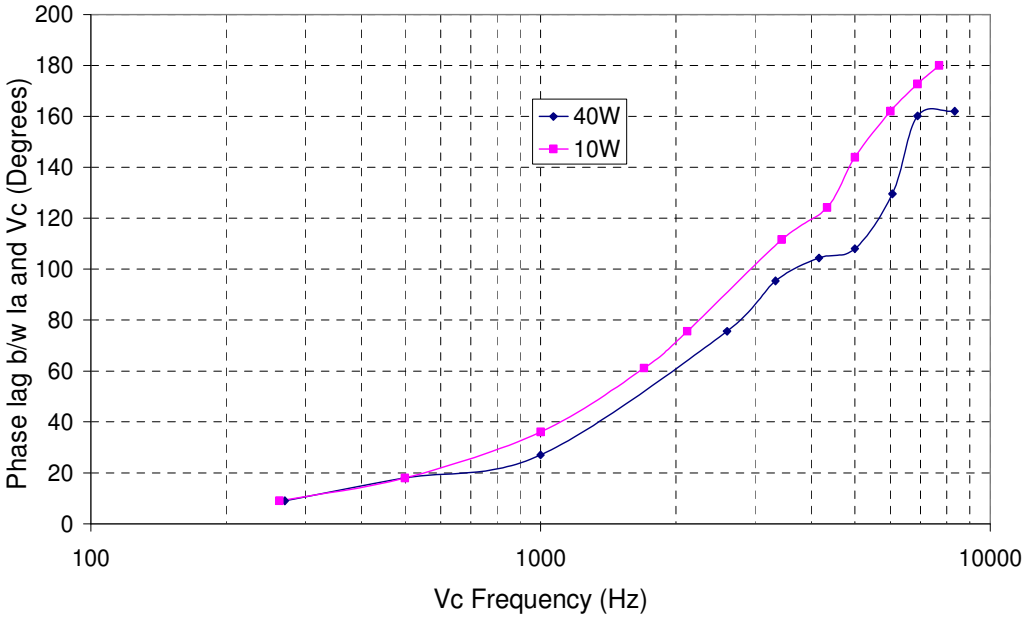

Figure 3.11 Phase delay through the power supply

Figures 3.12a and b show calculated open loop gain and phase margin plots of a PLL as shown in Figure 3.1 (with broken feedback path after divider) comprised of an ideal VCO with frequency sensitivity 14MHz/V and the loop filter of Figure 3.9. These plots are obtained by putting values of K_v, K_p, Z(s) and N from Section 3.2 into (3.3) where Z(s) is the transfer function of the loop filter given in Equation AII.16 in Appendix II.

Figure 3.12a gives unity gain at 3.5 kHz hence from Figure 3.12b there is 65^o of phase margin. The loop is stable according to the Nyquist Stability Criterion, which requires at least 45^o of phase margin when open loop gain is 1, to ensure the stability.

Introducing the effect of gain and phase change through the power supply, we obtain open loop gain and phase margin plots as shown in Figure 3.13a and 3.13b. These plots show the deviation of the VCMO (at the operating point of 14MHz/V) from an ideal VCO due to the switched mode power supply involved. Comparing the open loop response of the VCMO with that of an ideal VCO allows us to estimate the role of the switched mode power supply in the feedback loop performance. Addition of the power supply response brings the open loop bandwidth (point of unity gain) to about 2.7 kHz for the VCMO with 170^o phase margin. The Unity Gain Bandwidth of 2.7 kHz is much less than the power supply switching frequency (43 kHz) which ensures a stable operation.

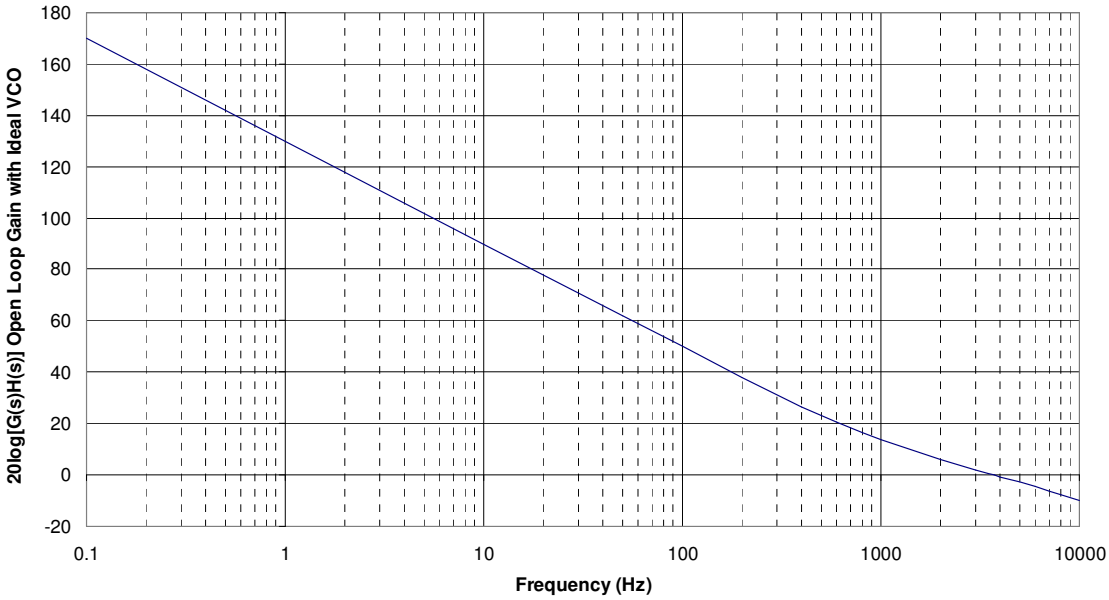

Figure 3.12a Open loop gain plot assuming an ideal VCO

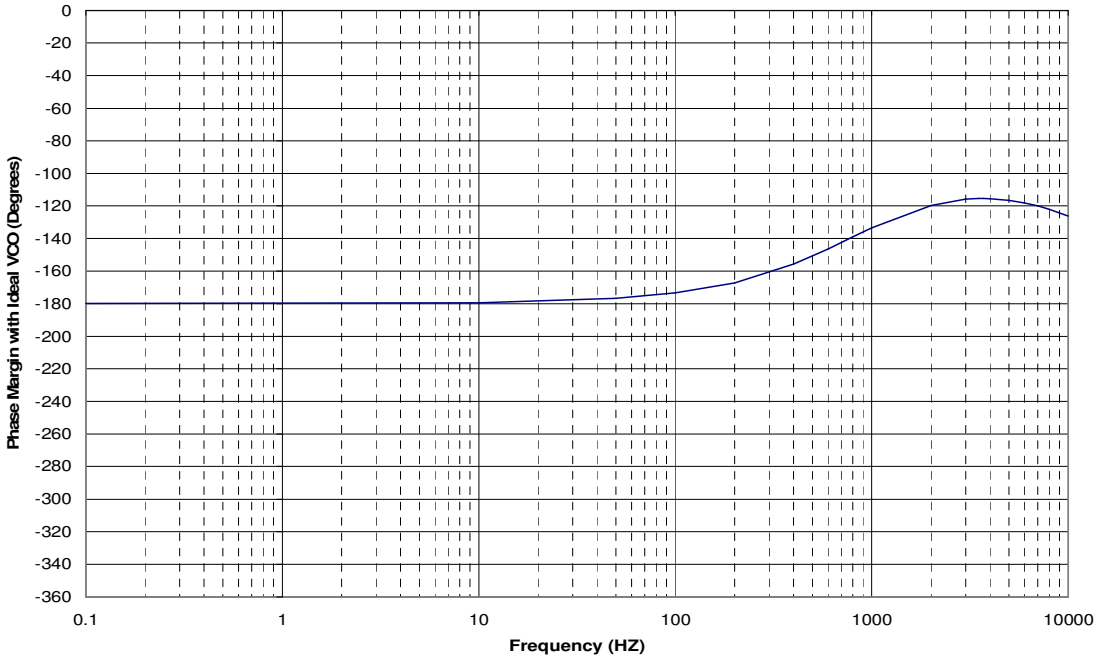

Figure 3.12b Open loop Phase Margin plot for an ideal VCO

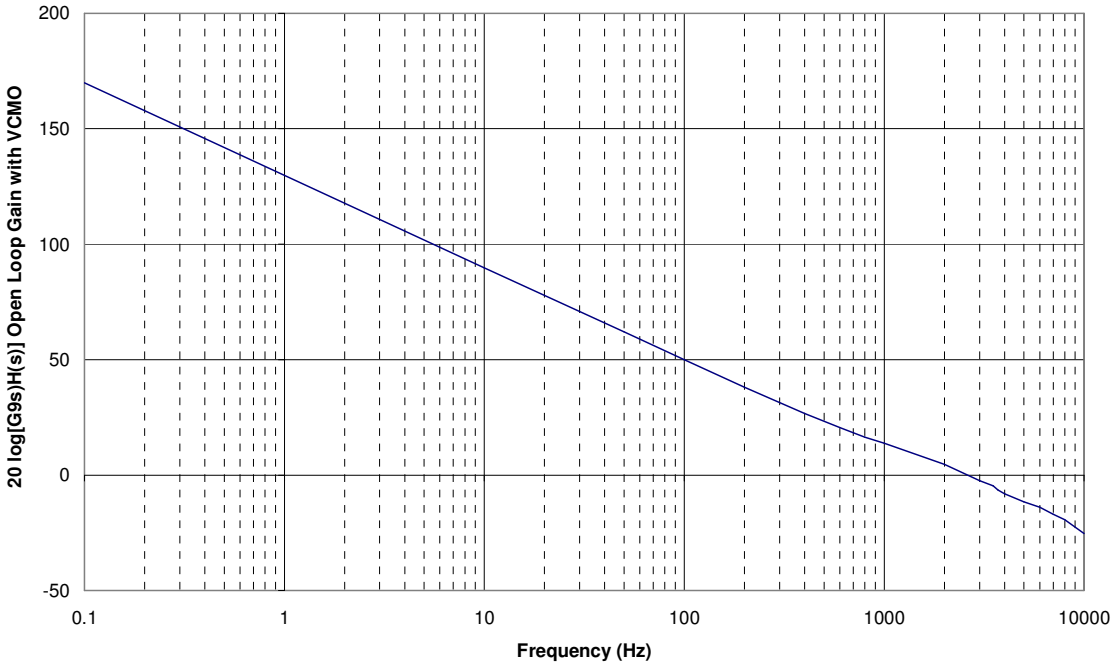

Figure 3.13a Open Loop Gain Plot with Power Supply and Magnetron

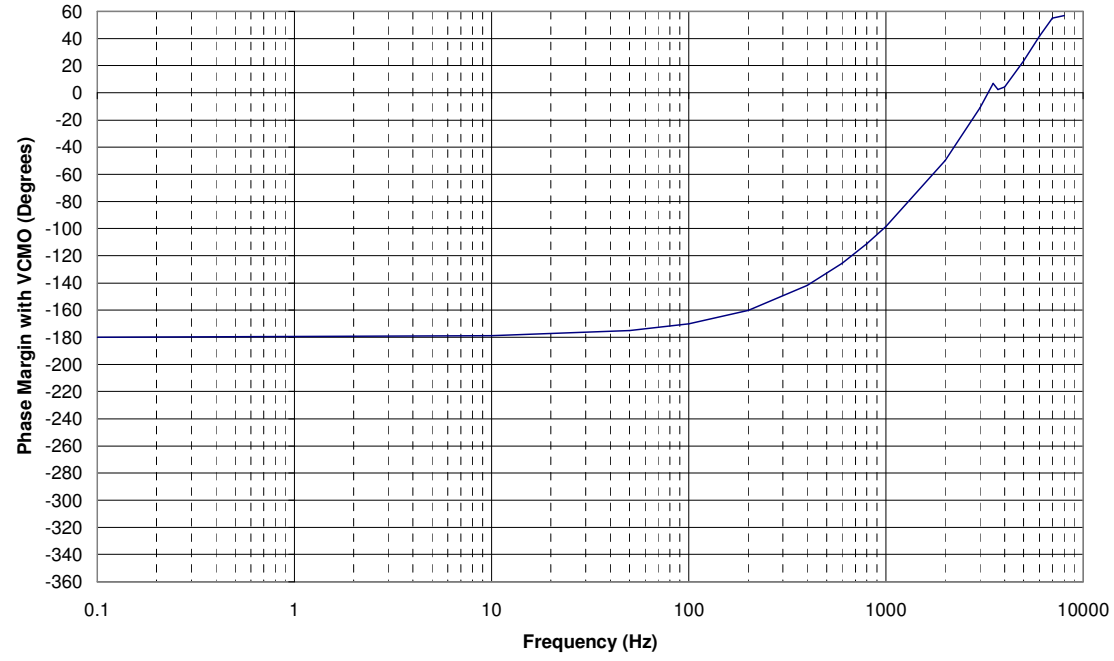

Figure 3.13b Open Loop Phase Margin Plot with 'Power Supply and Magnetron'

3.4 Spectral Performance of the magnetron with frequency locked loop

Frequency locking is achieved by implementing the setup shown in Figure 3.5. Spectra of the frequency locked magnetron output for different heater power levels are shown in Figures 3.14 to 3.19, along with corresponding amplitude demodulated outputs from a diode detector. Mean anode current was set to 340mA which is the maximum anode current for achieving a stable frequency lock. Above 380mA, it is not possible to obtain a frequency lock at all because the pushing curve flattens out. Operating at 340mA gives us a good anode current margin on the pushing curve.

Previously in Figure 2.8 large power dips tied to anode current ripple were seen at and above a heater power of 42W. In figure 3.14 one sees that the frequency control loop is able to remove these power dips and gives a greatly improved spectral output. It is interesting that frequency control can remove dips in amplitude. It is however the amplitude dip the causes the change in frequency hence the frequency feedback control is able to eliminate this instability and was able to do so for the heater powers below 46W.

For all heater powers except zero heater power Figures 3.14 to 3.19 show that the anode current ripple at 100 Hz is almost completely eliminated. Interestingly once the 100 Hz ripple has been removed the residual ripple has 50 Hz and 43 kHz components. The exception to this is for zero heater power shown in Figure 3.19 where there is no 50 Hz component but a 100 Hz component is re-introduced. The 43 kHz component remains as the loop bandwidth was just 2.7 kHz. The 50 Hz is a consequence of the control loop correcting the heater power frequency dependence shown in Figure 2.14.

Looking back at Figure 3.14 one sees that the power dips have a patterned repletion of 50 Hz which is likely to be tied to heater power ripple rather than anode current ripple. With frequency control not only does the frequency stay at the programmed value against typical perturbations but also there is a great reduction in bandwidth. The amplitude of the residual ripple on the anode current both at 100 Hz and 43 kHz contribute to the spectral bandwidth of the frequency locked magnetron. The spectral output of frequency locked magnetron with a heater power of 44W has a 3dB bandwidth of 200 kHz whilst the unlocked magnetron has a 3dB bandwidth of 1.5 MHz.

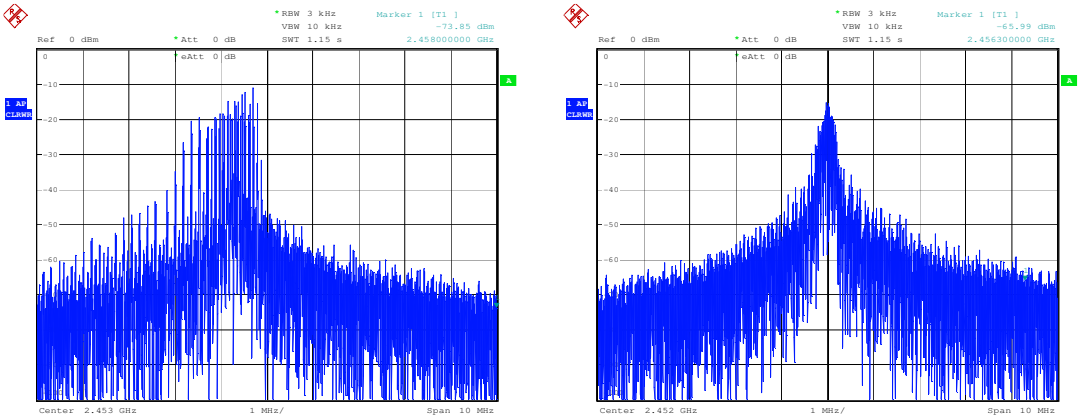

a With out frequency control With frequency control

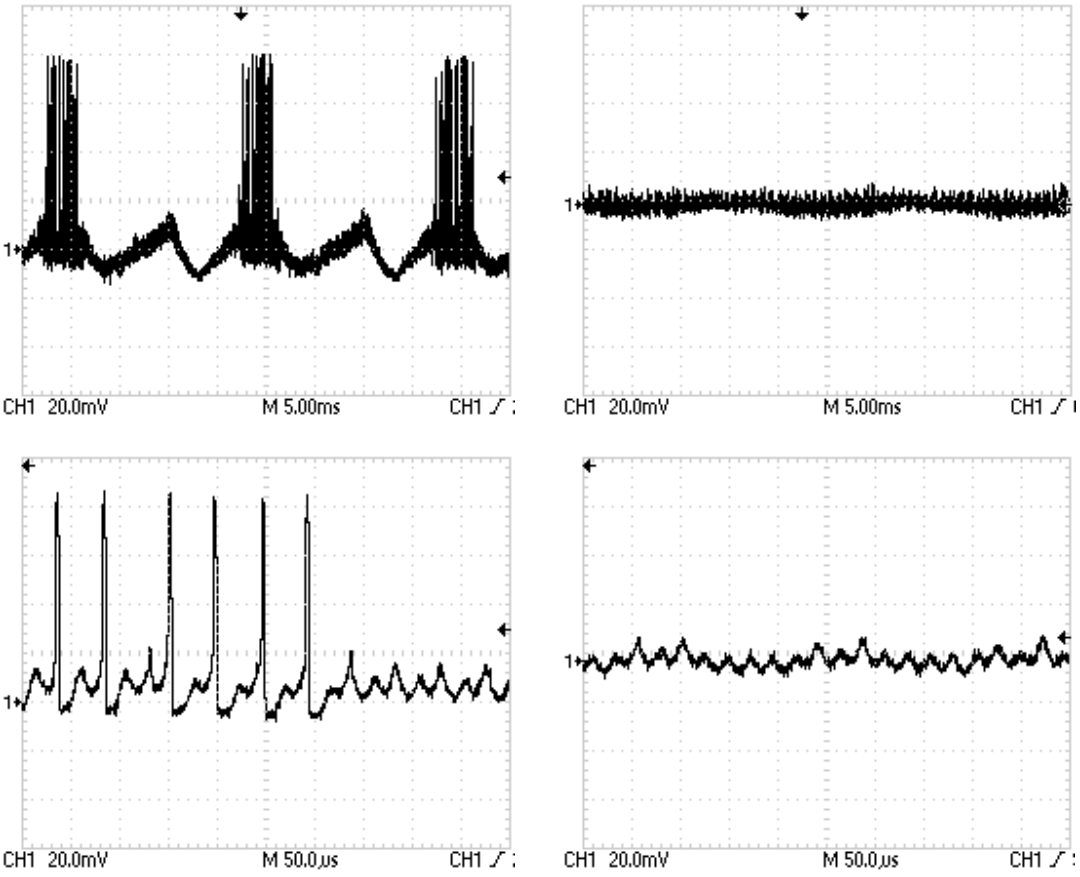

b With out frequency control With frequency control

Figure 3.14 Magnetron output with and without PLL control for **44W** heater Power

a: *Spectra for Magnetron RF output Power*

b: *Amplitude Modulation on RF Output (Diode detector) Top: @ 5ms/div Bottom: @ 50us/div*

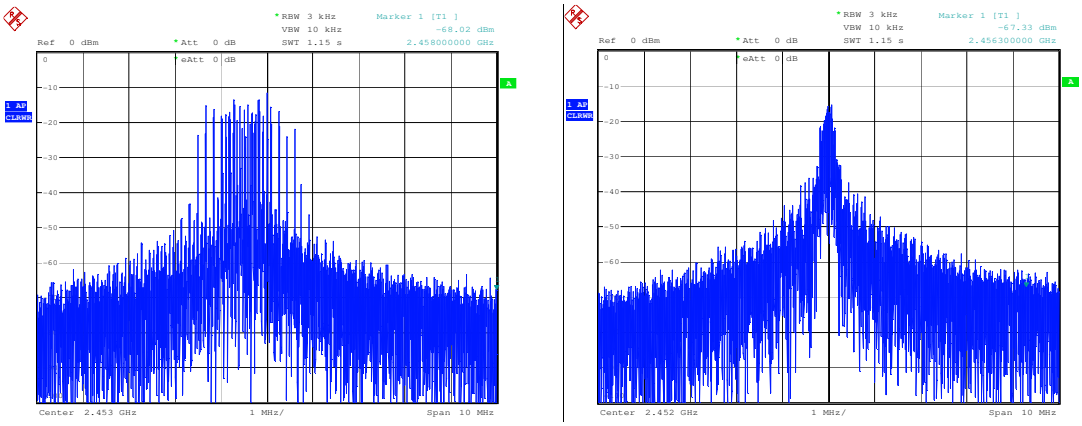

a With out frequency control With frequency control

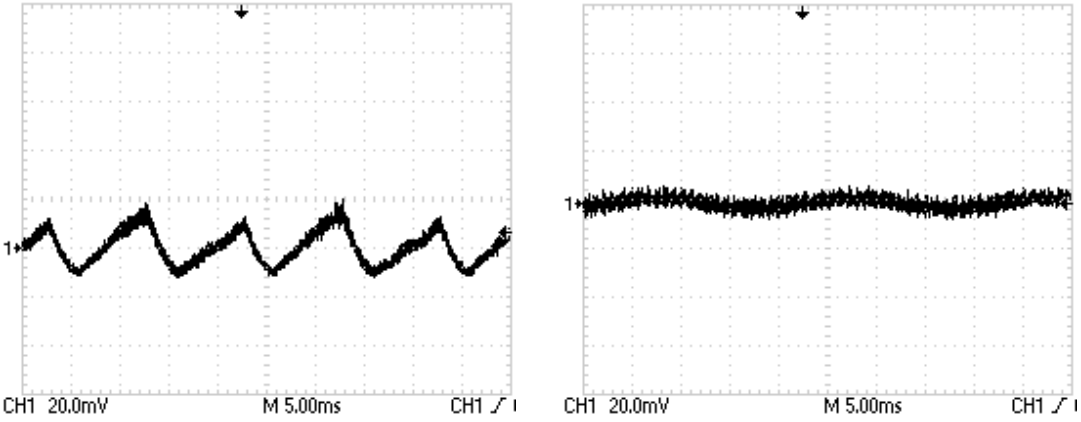

b With out frequency control With frequency control

Figure 3.15 Magnetron output with and without PLL control for **36W** heater Power

a: *Spectra for Magnetron RF output power*

b: *Amplitude Modulation on RF Output Power @ 5ms/div*

As determined by measurements presented in Figure 2.12 the region of heater power between 30W and 18W has a very unstable frequency response. It is not possible to acquire a frequency lock in this regime of the heater power and hence the Figures 3.14 to

3.19 omit this range. In Figure 3.16b, where the heater power is 18W, the scale is changed to *5mV/div (compared with 20mV/div in Figures 3.14b and 3.15b)* so that the effect of the anode current ripple as well as the heater mains ripple on the RF amplitude can be observed in greater detail as these levels are lower. Below 18W of heater power we have previously supposed that the cathode enters its temperature limited emission regime. As the excess electron cloud disappears, the effect of the fast anode current transients on frequency, such as the switching frequency ripple at 43 kHz is greatly reduced. In this heat power range and when the magnetron is frequency locked, the spectral spread is much less compared to that with 36W heater power. Additionally there is less correction in the anode current for the effect of 50 Hz heater ripple on the frequency. This might just be as a consequence of the heater power being lower.

The level of sidebands in the frequency spectrum at higher frequencies is also reduced greatly in the frequency locked state. At the heater power of 13W shown in Figure 3.17 the magnetron in its unlocked state has significant sidebands, which are reduced by the frequency feedback loop to a level below the noise floor of the spectrum analyser. At the heater power of 9W, the sidebands become very small in the unlocked state as shown in Figure 3.18a and with the frequency control these sidebands disappear from the instruments spectrum as they are presumably below its noise floor (-90 dBc). When the heater is completely off the sidebands are below the noise floor for both the unlocked as well as frequency locked state.

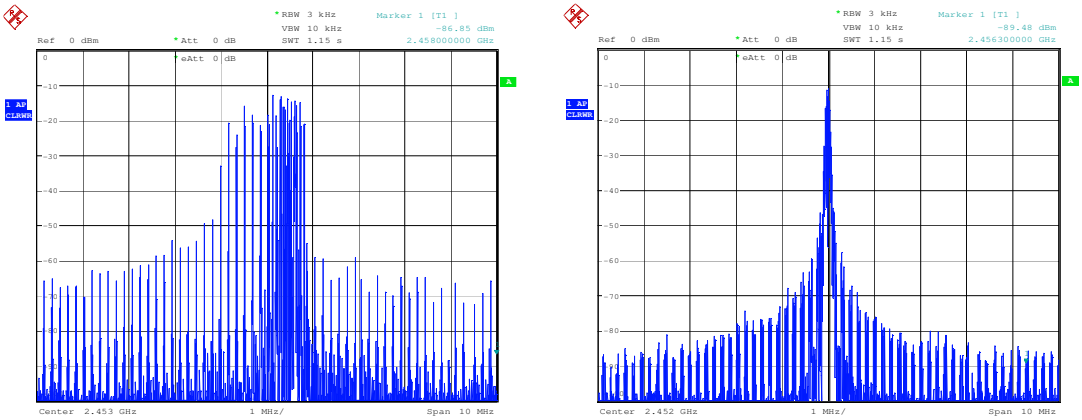

a With out frequency control With frequency control

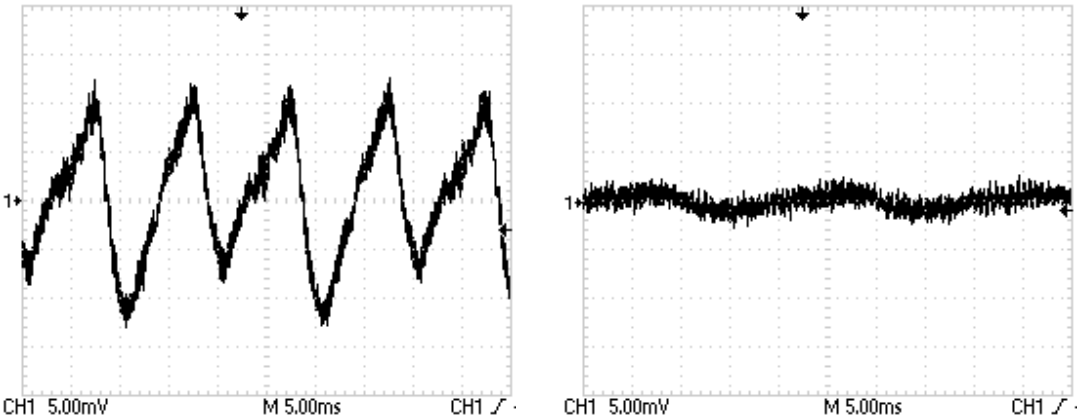

b With out frequency control With frequency control

Figure 3.16 Magnetron output with and without PLL control for **18W** heater Power

a: *Spectra for Magnetron RF output Power*

b: *Amplitude Modulation on RF Output power @ 5ms/div*

Note: *The scale/division on amplitude detector output is reduced to 5mV from 20mV for a better measurement*

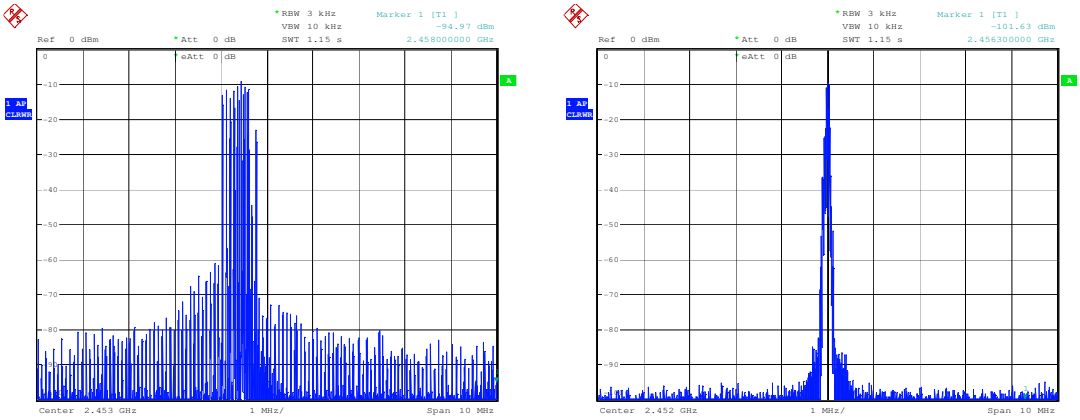

a With out frequency control With frequency control

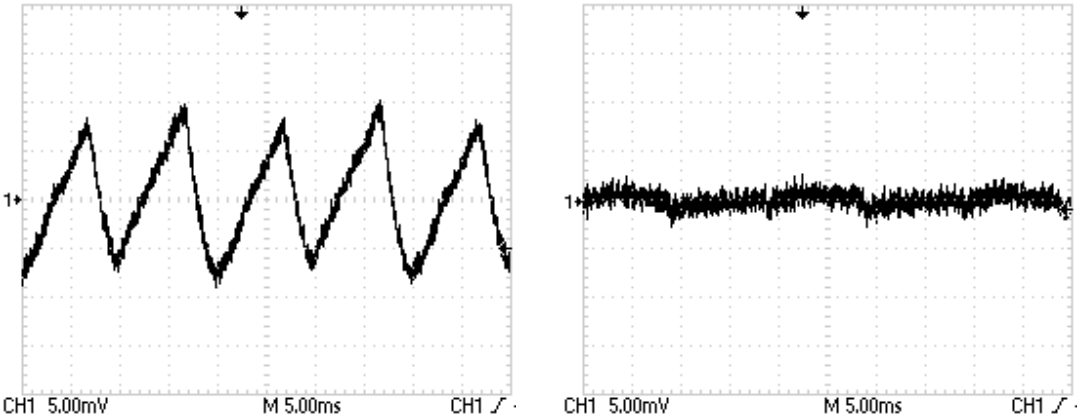

b With out frequency control With frequency control

Figure 3.17 Magnetron output with and without PLL control for 13W heater Power

a: *Spectra for Magnetron RF output*

b: *Amplitude Modulation on RF Output @ 5ms/div*

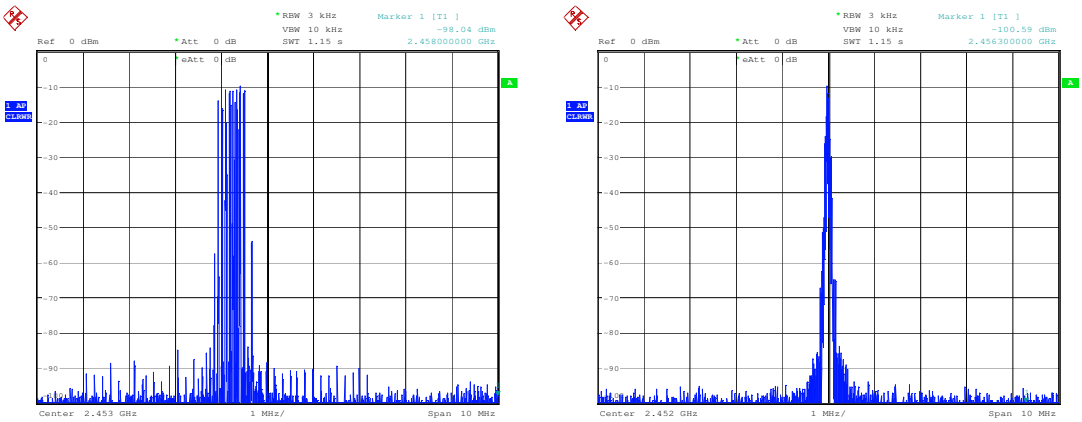

a With out frequency control With frequency control

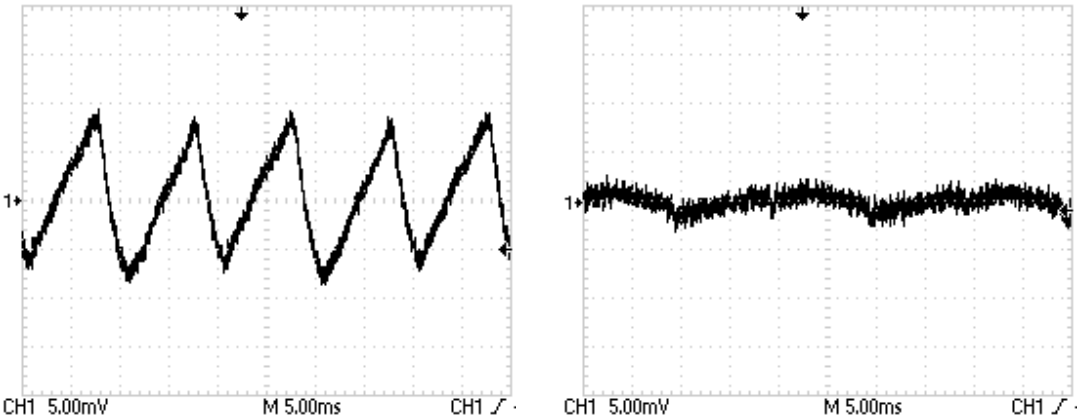

b With out frequency control With frequency control

Figure 3.18 Magnetron output with and without PLL control for 9W heater Power

a: *Spectra for Magnetron RF output*

b: *Amplitude Modulation on RF Output @ 5ms/div*

.

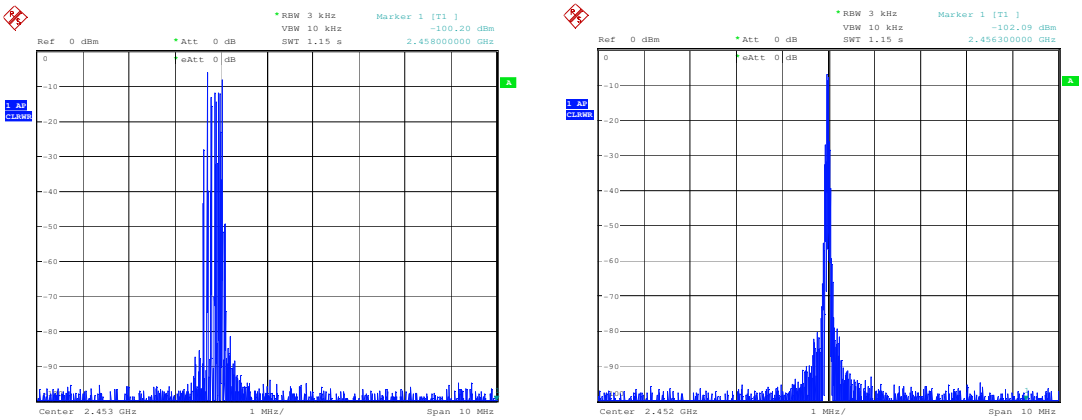

a Without frequency control With frequency control

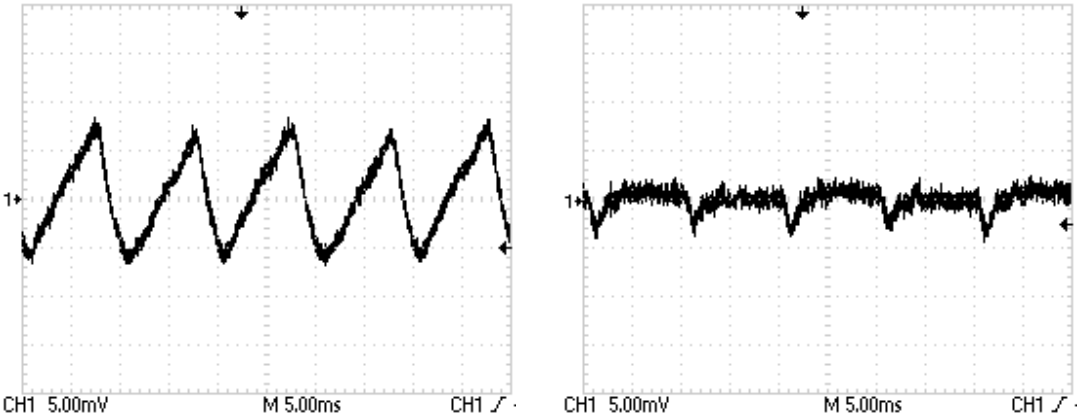

b Without frequency control With frequency control

Figure 3.19 Magnetron output with and without PLL control for No heater Power

a: *Spectra for Magnetron RF output*

b: *Amplitude Modulation on RF Output @ 5ms/div*

In figure 3.19b with frequency control we see that when the heater power is turned off the 100 Hz anode current ripple is not removed by the loop and residual spikes remain. If the frequency locked magnetron is operated with the filament heater off and with a lower anode current (e.g. 290 mA) the residual spikes become reduced.

Investigating further the anode current spikes for the frequency locked magnetron at zero heater power we measured DC voltage to the chopper alongside anode current. The oscilloscope was triggered on the 100 Hz ripple at 325V DC as it is the same for both unlocked and locked magnetron states. The results are shown in Figure 3.20. The mean value of the anode current with and without frequency control was nominally set to 340 mA. Moving along the voltage trace towards the lowest point of the 100 Hz ripple occurring at 297 V (peak being 325 V DC), we see a current surge (note that a current surge is a downwards transgression in the trace). It is likely that the loop is working effectively and the current surge is required to compensate a steeply rising voltage. The reason for this is not clear to us.

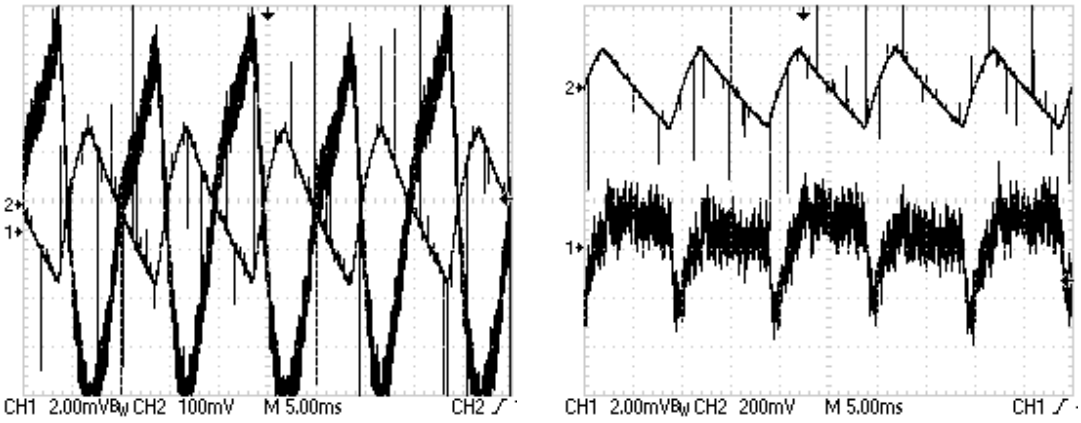

Without frequency control With frequency control

CH1 : Ripple on anode current, CH2 : Ripple on 325V DC

Figure 3.20 Ripple levels with and without frequency control (No Heater Power)

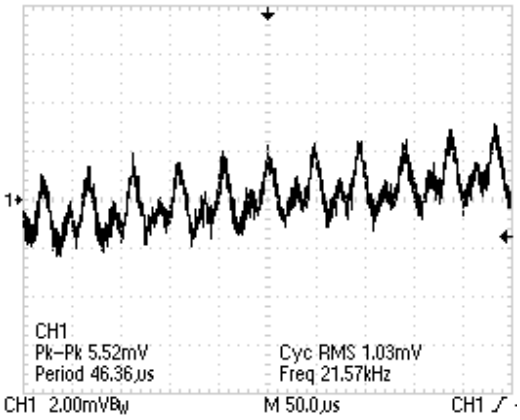

Without frequency control showing 43 kHz ripple and its sub-harmonic 21.5 kHz

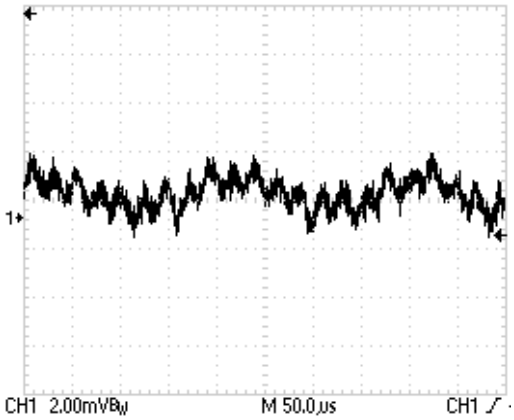

With frequency control showing the 43 kHz ripple and 2.7 kHz component at the loop natural frequency

Figure 3.21 Ripple levels with and without frequency control (No Heater Power)

As the feedback loop is not correcting the 43 kHz current ripple, component at the loop's natural frequency of 2.7 kHz should appear in all the anode current traces in figures 3.14 to 3.20. This ripple can be seen clearly in Figure 3.21.

Figure 3.21a and 3.21b show a comparison between the unlocked and locked spectra at 9W and no heater power respectively, on an expanded time scale.

Figures 3.14 to 3.20 show that when the magnetron runs with its PPL using the ADF4113 there is a great reduction in bandwidth with respect to the unlocked state and the centre frequency is locked to the 10MHz reference. This state has frequency lock but not phase lock. The frequency cycles in a range of about 50 kHz (for 10W heater power and below) as a consequence residual ripples at 43 kHz.

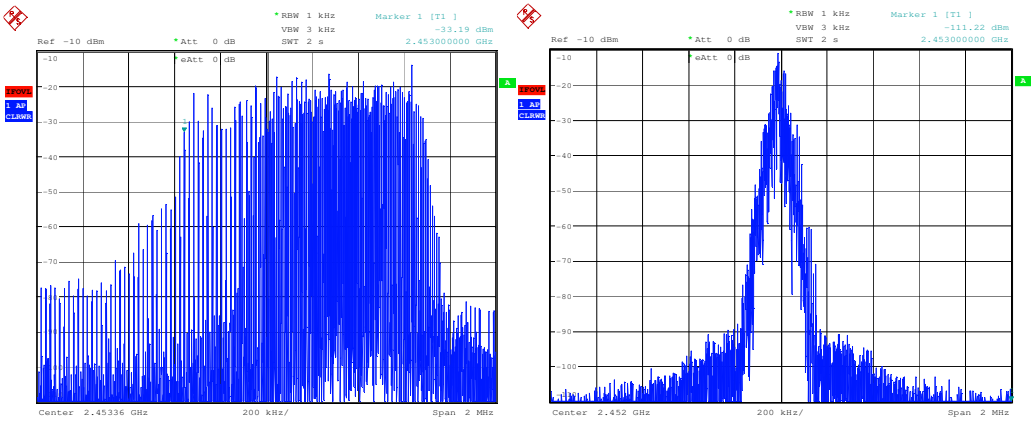

With out frequency control With frequency control

a Spectra with 200KHz/Div for better comparison 9W heater power

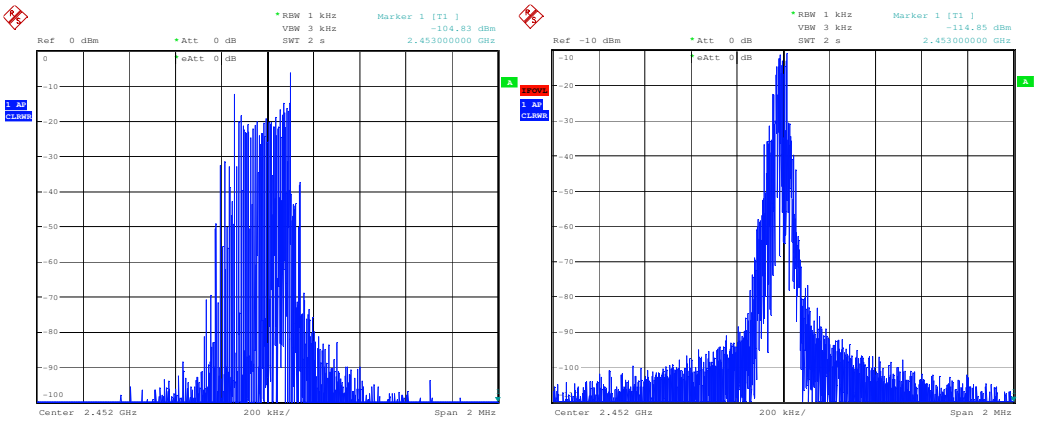

Without frequency control With frequency control

b Spectral Comparison @200kHz/Div for 0W Heater Power

Figure 3.21 Spectra with 200 kHz/Div scale for a better comparison

To phase lock the magnetron to the reference, the 43 kHz ripples must be managed and this is not possible due to the nature of the switch mode power supply and consequently the loop bandwidth. Phase locking can be achieved by introducing an injection signal at a frequency exactly equal to the centre frequency of the locked magnetron spectrum [25]. This method is discussed in detail in Chapter 4.

CHAPTER 4

FREQUENCY LOCKED OPERATION WITH SMALL INJECTION POWER

It was known soon after the development of the magnetron during WWII that it can be injection locked to an external source just like other oscillators [27], [29], [30]. Experiments on injection locking of the magnetron were difficult until high power circulators became available in the 1960s [37]. During the 1970's injection locked magnetrons were investigated for Doppler radar with the aim of achieving high powers and cleaner X and K band spectra for long pulse and CW operation [36]. In this paper phase noise performance of a highly stable magnetron was measured for injection levels as low as -55 dBc and phase locking was observed to -30 dBc. Ensuring a wide lock-in range against warm-up and ambient temperature related frequency drifts, load variations and pushing effects due to instability of the high voltage source was a problem for injection levels below -10 dBc. Different schemes were suggested to address this issue, such as tracking the magnetron natural frequency as it drifts using a frequency discriminator and keeping the injection frequency near enough to it, or using heavier VTM (voltage tuneable magnetron) instead and keeping its frequency close to the injection signal by varying its anode voltage. Practical implementation of such techniques and corresponding analysis of their performance is non-existent in the literature, due to

difficulty of obtaining precise control over very high voltages. In 1980's W.C Brown proposed and implemented this by controlling the anode current to keep the natural frequency of the magnetron output close to the injection signal through magnetic field as described in the beginning of Chapter 3 [8].

In this chapter, a novel method of keeping the magnetron's natural frequency the same as the injection signal is presented which makes use of a frequency feedback loop technique described in Chapter 3. The components used in its implementation are widely found in wireless and mobile communication devices and are very low cost, small in size and reliable in performance. We first look at the input injection power requirement and the magnetron output phase offset when the magnetron's natural frequency differs from the injection signal.

4.1 Power requirement for Injection Locking

Figure 4.1 gives the simplest circuit model representation of a magnetron that can predict injection locking performance Slater [29]. A justification of this model is given by David [30]. In this simplified circuit we associate an RF voltage with excitation of the π mode.

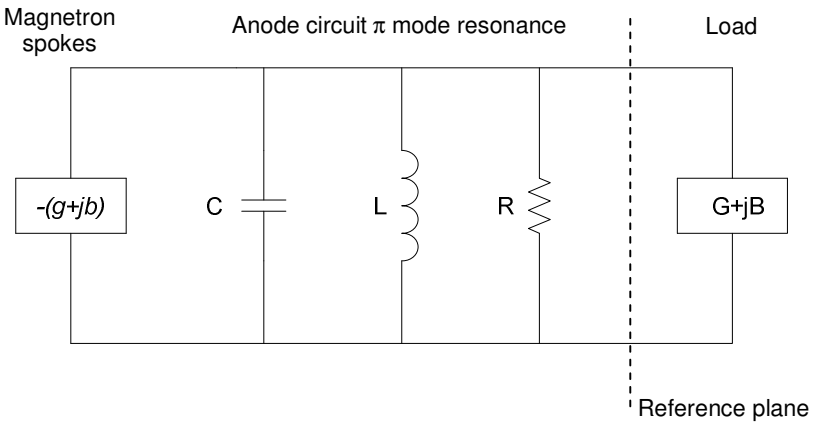

Figure 4.1 Simplified Magnetron Equivalent Circuit

Equating RF current from the magnetron spokes to current flowing in the anode circuit and the external load gives

$$\frac{g+jb}{C\omega_o} = j\left(\frac{\omega}{\omega_o}-\frac{\omega_o}{\omega}\right)+\frac{1}{Q_o}+\frac{G+jB}{Q_{ext}} \qquad (4.1)$$

where

ω_o = Resonant frequency of magnetron cavity π mode (Cold State)

ω = RF output frequency (Hot State)

$g + jb$ = Nonlinear admittance representing the effect of the charged spokes, normalised to the output waveguide characteristic impedance.

C = Effective capacitance of the magnetron cavity π mode (Hot state)

Q_o = Unloaded Q of the resonant magnetron cavity π mode (Cold state)

Q_{ext} = External Q of the cavity (Cold state), a measure of the coupling of the cavity to the output waveguide

$G + jB$ = Load admittance, normalised to waveguide characteristic admittance

If the magnetron is oscillating and generating RF current let

Voltage provided by magnetron = $V e^{j\omega t}$ (4.2)

Current from magnetron = $I e^{j\omega t}$ (4.3).

When an external signal is injected into the magnetron from its output side with a different frequency let

Voltage provided by injected source = $V_i e^{j\omega_i t}$ (4.4)

Current from injected source = $I_i e^{j\omega_i t}$ (4.5)

The admittance of the load at the reference plane marked in Figure 4.1 is given by

$$Y = \frac{Ie^{j\omega t} - I_i e^{j\omega_i t}}{Ve^{j\omega t} + V_i e^{j\omega_i t}} = \frac{I}{V}\left[\frac{1 - \frac{I_i}{I} e^{j(\omega_i - \omega)t}}{1 + \frac{V_i}{V} e^{j\omega_i - \omega)t}}\right] \quad (4.6),$$

note that the injection current I_i carries the opposite sign as it was defined from the injection source rather than from the magnetron.

If I_i/I and V_i/V are small then a Binomial expansion of (4.6) to first order gives

$$Y_L \approx Y_o\left[1 - \left(\frac{I_i}{I} + \frac{V_i}{V}\right) e^{j(\omega_i - \omega)t}\right] \quad (4.7)$$

where

$Y_o = I/V$ (4.8)

Dividing by the characteristic admittance of the waveguide gives and using out definition of the load impedance without the injection signal gives

$$Y_{eq} \approx (G + jB)\left[1 - \left(\frac{I_i}{I} + \frac{V_i}{V}\right) e^{j(\omega_i - \omega)t}\right] \tag{4.9}$$

Equation (4.1) applies when there is no injection signal. When the injection signal is added the effective admittance of the load is now given by (4.9) hence the current balance equation is obtained by replacing $G + jB$ in (4.1) with Y_{eq} in (4.9) to give

$$\frac{g + jb}{C\omega_o} = j\left(\frac{\omega}{\omega_o} - \frac{\omega_o}{\omega}\right) + \frac{1}{Q_o} + \frac{(G + jB)\left[1 - \left(\frac{I_i}{I} + \frac{V_i}{V}\right) e^{j(\omega_i - \omega)t}\right]}{Q_{ext}} \tag{4.10}$$

Defining θ as the phase difference between the magnetron and the external injection signal then we can write

$$\theta = \omega t - \omega_i t \tag{4.11}$$

and

$$\frac{d\theta}{dt} = \omega - \omega_i \tag{4.12}$$

The reason for reproduction of the mathematical work consisting of (4.1) - (4.19) from Slater's report [29] is to emphasize the way (4.11) and (4.12) are assumed in order to achieve the locking condition given in (4.18). It is a first order assumption which leads to a first order result in (4.18). We will see in Chapter 5 that if injection phase suddenly changes, the transient response of the magnetron RF output phase is of the second order. However for steady state condition above assumption remains valid.

Putting θ in (4.3) we may write

$$\frac{g + jb}{C\omega_o} = j\left(\frac{\omega}{\omega_o} - \frac{\omega_o}{\omega}\right) + \frac{1}{Q_o} + \frac{(G + jB)}{Q_{ext}} + \frac{A\,e^{-j\theta}}{Q_{ext}} \tag{4.13}$$

where

$$A = -(G + jB)\left(\frac{I_i}{I} + \frac{V_i}{V}\right) \tag{4.14}$$

We can choose the reference plane for the phase of the injection signal such that *A* is real

With *A* real equation (4.13) can be split into its real and imaginary parts to give

$$\frac{g}{C\omega_o} = \frac{1}{Q_o} + \frac{G}{Q_{ext}} + \frac{A\cos\theta}{Q_{ext}} \tag{4.15}$$

$$\frac{b}{C\omega_o} = \frac{\left(\omega^2 - \omega_o^2\right)}{\omega\omega_o} + \frac{B}{Q_{ext}} - \frac{A\sin\theta}{Q_{ext}} \tag{4.16}$$

when $\omega \approx \omega_o$ which is the case for injection locking equation (4.16) becomes

$$\frac{b}{C\omega_o} \approx 2\frac{(\omega - \omega_o)}{\omega_o} + \frac{B}{Q_{ext}} - \frac{A\sin\theta}{Q_{ext}} \tag{4.17}$$

Re-arranging (4.17) to get w on the LHS gives

$$\omega = \omega_o - \omega_o\frac{B}{2Q_{ext}} + \frac{b}{2C} - \omega_o\frac{A}{2Q_{ext}}\sin\theta \tag{4.18}$$

From (4.12), we have $\omega = \frac{d\theta}{dt} + \omega_i$ hence (4.18) takes the form

$$\frac{d\theta}{dt} = \omega_o\frac{A}{2Q_{ext}}\sin\theta + \left(\omega_o - \omega_o\frac{B}{2Q_{ext}} + \frac{b}{2C}\right) - \omega_i \tag{4.19}$$

The differential equation (4.19) describes locking process. In the absence of an injection signal θ would be zero hence equation (4.18) gives the magnetron frequency in this instance as ω' given as

$$\omega' = \omega_o - \frac{B}{2Q_{ext}}\omega_o + \frac{b}{2C} \tag{4.20}$$

where b determines pushing and B determines pulling.

When an injection signal is present and if the phase is locked so that $\frac{d\theta}{dt} = \omega - \omega_i = 0$ then equation (4.19) gives an expression that determines the phase difference between the injection signal and the magnetron output signal as

$$0 = \omega_o \frac{A}{2Q_{ext}} \sin\theta + \left(\omega_o - \omega_o \frac{B}{2Q_{ext}} + \frac{b}{2C} \right) - \omega_i \tag{4.21}$$

hence substituting for the frequency in absence of injection from (4.20) we get

$$\sin\theta = -\frac{2Q_{ext}}{\omega_o A}(\omega' - \omega_i) \tag{4.22}$$

From (4.22) we see that the phase between the magnetron's output and the injection input θ changes when the magnetron's natural frequency ω' drifts away from the injection frequency ω_i. If ω' differs from ω_i by a fixed frequency offset then the phase difference θ takes a fixed value provided that LHS of (4.22) is less than unity. From (4.14) and (4.22) we see that the value of the phase angle θ depends upon the reciprocal of the injection level determined from the injection current and voltage terms in A. The phase angle also depends on the load present at the magnetron output. As the injection level decreases or the difference between the injection frequency and the magnetron natural frequency increases then the magnitude of the RHS of (4.22) increases towards the value of one. When it reaches one the angle θ has moved away by +/-90^o. If the RHS of (4.22) increases further the argument of the inverse sine required to determine θ becomes greater than one and the magnetron will unlock from the injection signal.

4.2 Experimental setup for injection locking of the frequency locked magnetron

Figure 4.2 shows the setup to generate an injection signal which has a frequency equal to the centre frequency of the frequency locked magnetron. The 10 MHz reference has a 3dB split, one derived signal is used to lock the magnetron as described in Chapter 3, and the other provides the reference signal to another ADF4113 IC which controls the phase and the frequency of a 2.3-2.6 GHz VCO. The VCO is phase locked to the 10 MHz reference in a similar way as the magnetron is frequency locked to the same reference. The VCO is easily phase locked because there is no fast pushing present due to ripple on its power supply and no fast pulling as the load is constant. The frequency perturbations for the VCO mostly due to slow temperature drifts are well within the control loop bandwidth and easily corrected.

Both ADF4113 ICs are programmed with the same division ratios by two identical microcontrollers (AT89c4051). Both microcontrollers hold the same executable programme. The detailed circuit diagram and design of the injection source, which consists of the ADF4113, a loop filter and the VCO is presented in Appendix III.

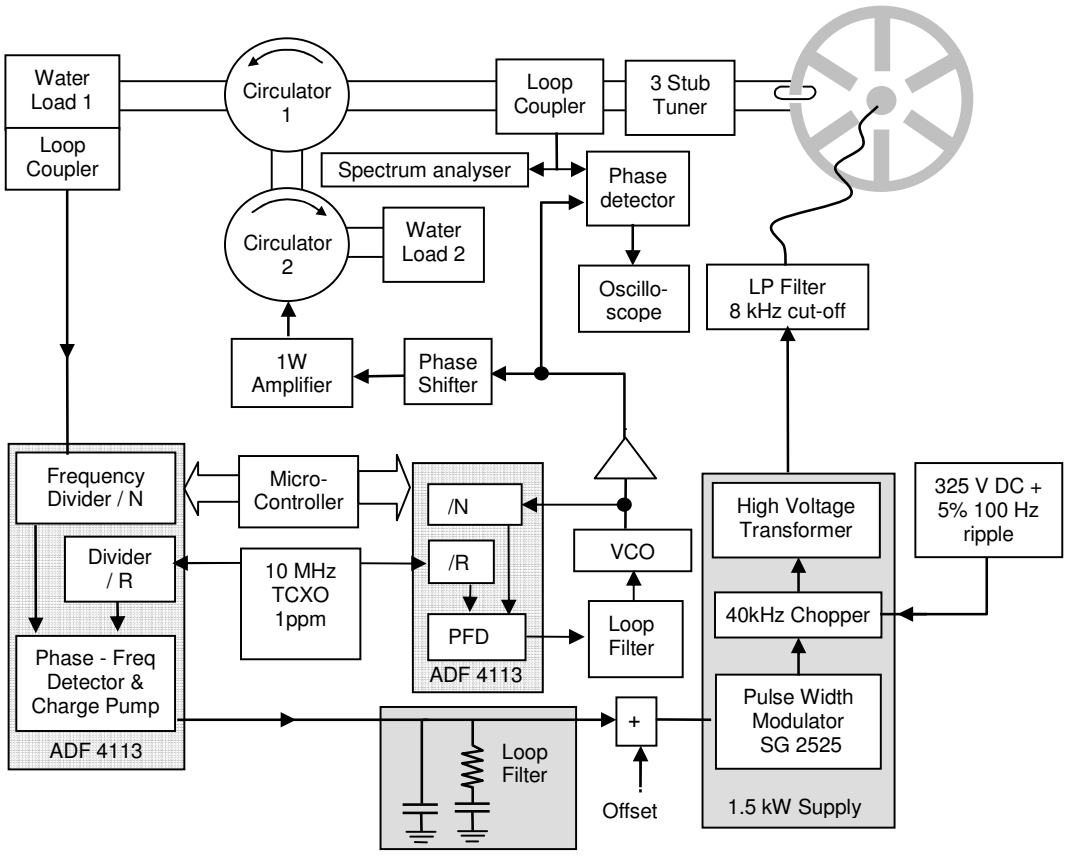

Figure 4.2 Experimental Setup for Injection of frequency locked magnetron

The injection signal is amplified through a 1W amplifier and then injected into the magnetron output via two circulators as shown in the Figure 4.2. Circulator 2 next to the 1W amplifier protects it from reflected power from the load 1. The power rating of circulator 2 depends upon the worst case power reflection from load 1. A 60 dB loop coupler and a 3-stub tuner are inserted between the circulator 1 and the magnetron. The 60 dB loop coupler samples the magnetron output which is then divided to provide input for spectral analysis and input for a phase detector. The phase detector compares the phase of the magnetron RF output with the injection signal. The phase detector output was amplified (typically by 10 dB) using a low noise op-amp (1 MHz bandwidth) and

recorded on an oscilloscope. The three-stub tuner provided differing loadings for the magnetron output as required by the experimental program. The rest of the magnetron frequency control circuitry is the same as described in Chapter 3.

4.3 Injection Signal's spectral purity

Phase jitter present in the injection source was analysed before evaluating the magnetron performance with frequency control and injection locking. Injection signal spectra are shown in Figure 4.3 with four different spans (1 kHz, 10 kHz, 100 kHz and 1 MHz) and appropriate resolution bandwidths.

The spurious sidebands at 100 kHz and 200 kHz offset from the carrier in Figure 4.3a are due to the PFD comparison frequency which is 200 kHz. In the phase locked state the PFD generates current spikes at the comparison frequency as its internal switches close to re-charge the integrating capacitor in the loop filter. These spikes leak through the later stages of the loop filter as the open loop bandwidth of the loop is set to about 30 kHz (as compared with $200kHz$). Note that the measurements are made with the magnetron turn off as complete isolation was difficult. Design and different parameters of the injection source are discussed in the Appendix III.

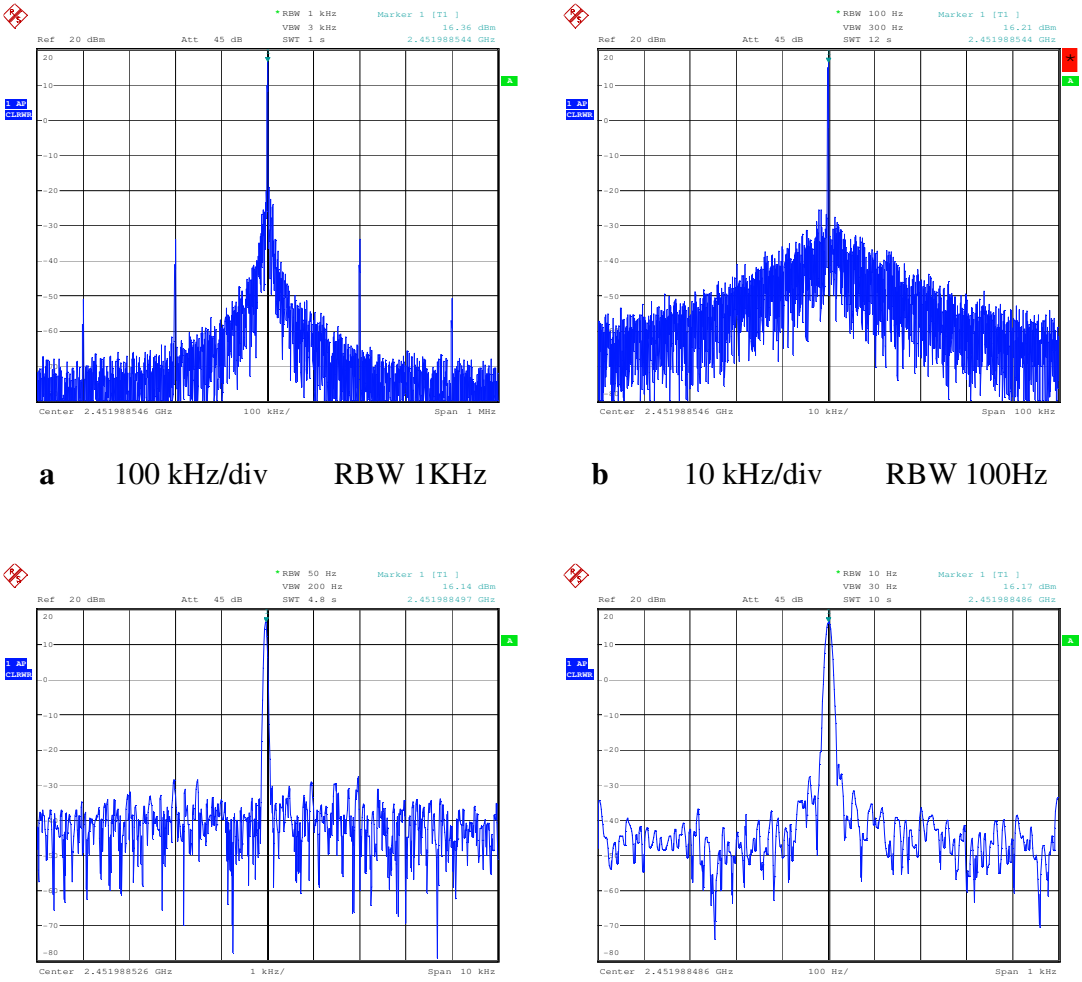

a 100 kHz/div RBW 1KHz **b** 10 kHz/div RBW 100Hz

c 1 kHz/div RBW 50 Hz **d** 100 Hz/div RBW 10 Hz

Figure 4.3 Injection signal frequency spectrum when the magnetron is switched off

4.4 Performance of the frequency locked magnetron with injection

In this thesis when the magnetron is frequency locked and the injection signal is introduced, we refer to the mode of operation as 'FLL + Injection Mode'. Figure 4.4 shows the change in the frequency spectrum when a -30 dBc injection signal is introduced with the filament heater completely turned off. The magnetron output spectrum over a span of 1 MHz is almost the same as the injection signal spectrum presented in

Figure 4.3a with the exception of spikes 43 kHz apart coming from the power supply switching frequency and its harmonics. These spikes are below -67 dBc for 100 kHz offset from the carrier and beyond.

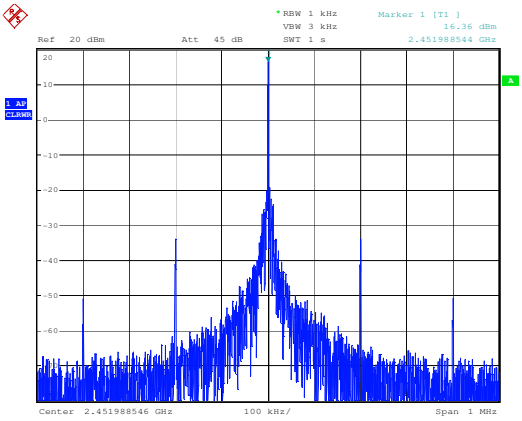

Figure 4.3a (repeated for comparison below) Injection signal 100 kHz/div

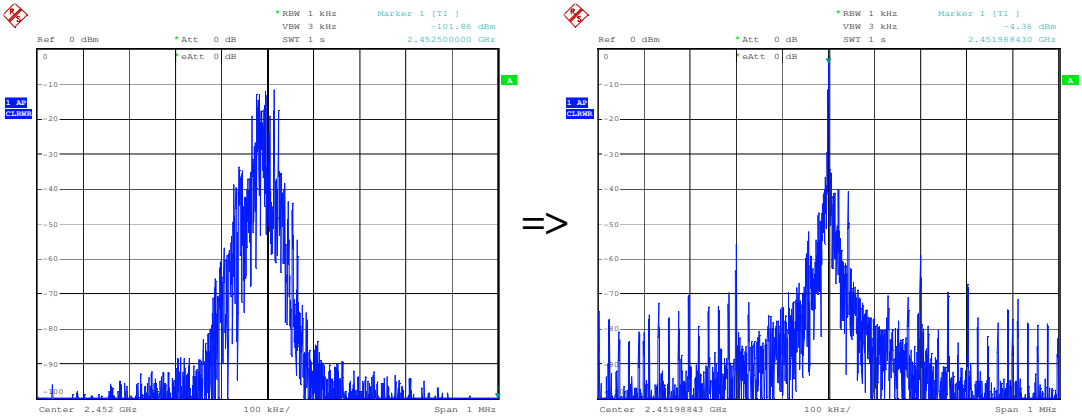

a 100 KHz/div RBW 1 KHz **b** 100 KHz/div RBW 1 KHz

Figure 4.4 **a**: Spectrum with frequency control only

b: Spectrum with FLL+ Injection (500mW)

Assuming a constant load and ignoring the effects of the anode temperature, the parameters most affecting the magnetron's natural frequency and hence phase jitter are injection level, heater power and anode current. This is discussed in sections 4.5 and 4.6.

4.5 Injection level effect on the spectral performance with the heater turned off

The effect of injection signal power was investigated with two different injection power levels of 500mW and 50mW and where the magnetron RF output was 800W corresponding to 330 mA anode current. The heater was turned off during these measurements. Frequency spectra shown in Figure 4.6 corresponding to the two power levels have been recorded for different spans and resolution bandwidths. Although the r.m.s. phase jitter can be estimated directly from the spectra using Fourier analysis techniques, time domain measurements are also required to evaluate the performance of the feedback control system. A 1.3 GHz Digital Phase Detector HMC439 was used to make these measurements and they are shown in Figure 4.7. A further direct validation of locking performance was made by direct observation of the magnetron output waveform using a high frequency oscilloscope. Snapshots from the oscilloscope are presented in Figure 4.8.

4.5.1 Spectrum Analyser results

Closer analysis of frequency spectra presented in Figure 4.6 reveals that there is about 5 dB overall reduction in the suppression of sidebands throughout the measured spans when injection power is decreased from 500mW to 50mW.

Injection Level : 500mW(-32 dBc) **Injection Level :50mW(-42 dBc)**

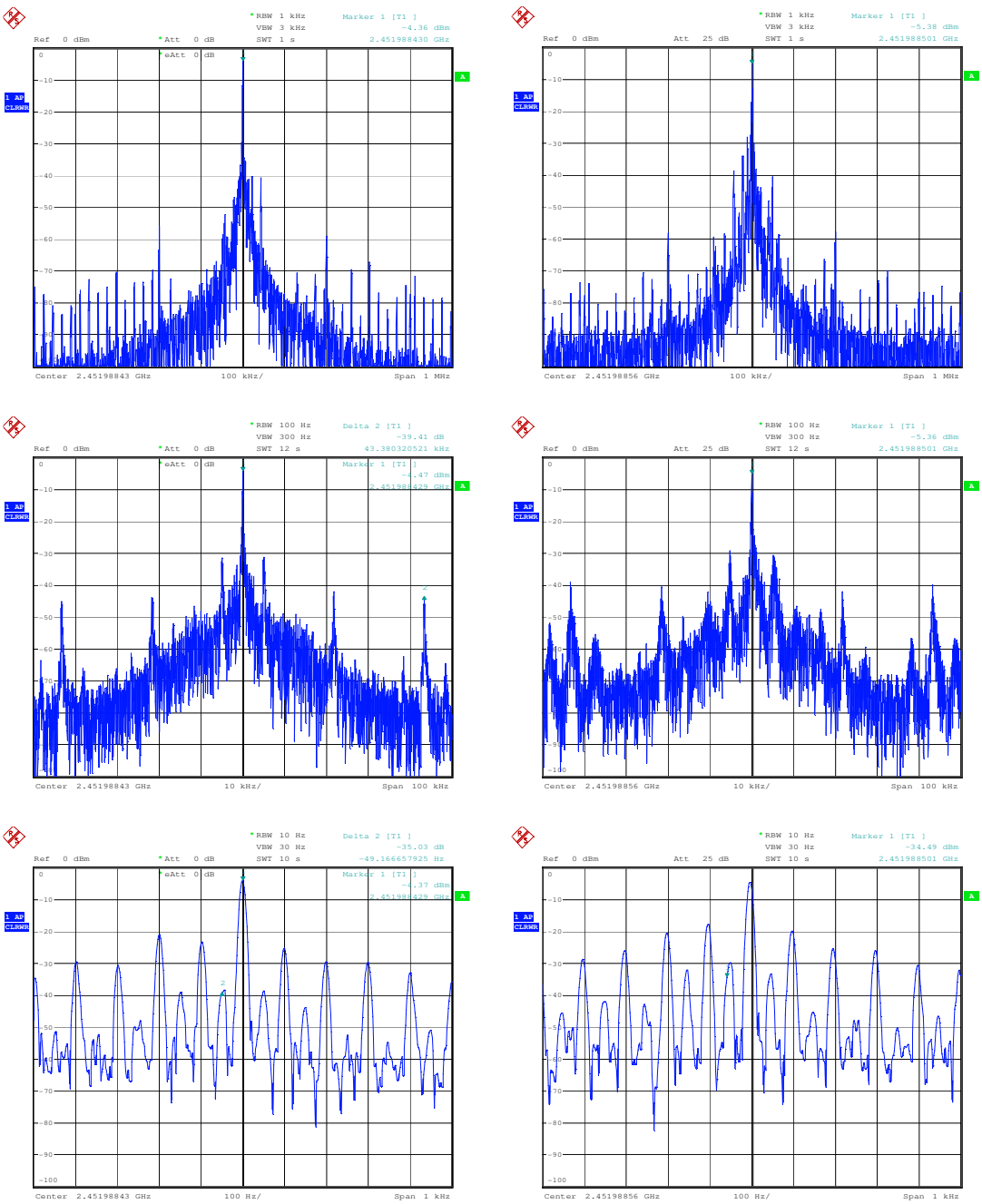

Figure 4.6 Injection locked spectra with different spans and two injection levels, 500mW and 50mW Top Trace: *100 kHz/div*, Middle Trace: *10 kHz/div* Bottom Trace: *1 kHz/div*

The 100 Hz anode current ripple shown in the top trace of Figure 4.7 for FLL + injection is about 13% which is similar to that for constant PWM operation given in Chapter 2 rather than for frequency lock operation given in Chapter 3. When injection locked, this ripple produces only small phase shifts as opposed to large frequency drifts when the injection signal is not present. As the error signal now becomes very small the loop gain drops excessively and the frequency feedback no longer corrects for associated phase shifts. More detail on this issue is given in the next section. The phase modulation produced by this ripple is shown in the bottom trace of Figure 4.6 where sidebands at 100 Hz and its harmonic frequencies can be observed.

4.5.2 Phase Detector results

In Figure 4.7a and 4.7b, the top trace is the anode current ripple (measured across the 47 Ω resistor) and the bottom trace is the Phase Detector output. One big division on CH2 represents a phase of about 12 degrees. We have 13 degrees peak to peak phase shift for 500mW injection level and 48 degrees peak to peak for 50mW injection level. It is important to notice that as the anode current is AC coupled in CH1 and it is a negative voltage, the lower peak represents a higher anode current.

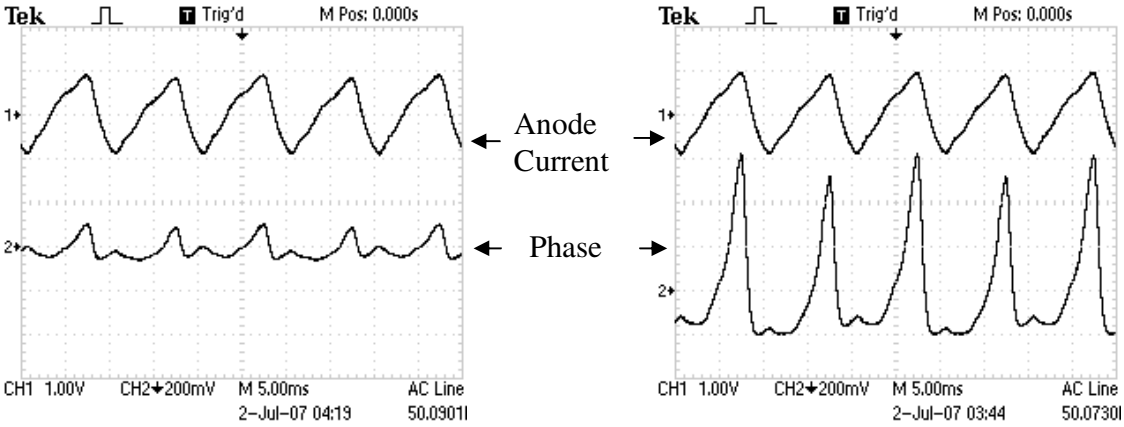

a 500mW Injection Level (-31.5 dBc) **b** 50mW Injection Level (-31.5 dBc)

Figure 4.7 Anode Current (CH1) and Phase Detector Output (CH2), for anode current 330mA and filament heater turned off

The shape of the phase shift depends upon the pushing curve and the effect of slope reversal of the pushing curve on the phase when anode current accounts for some of the complexity in CH2. Slope reversal at higher anode currents for small heater power was described in Chapter 2, Figure 2.6.

Apparent from Figures 4.6 and 4.7 is that the power supply ripples that produced frequency shifts in the absence of an injection signal, now with the magnetron injection locked only produce phase shifts (phase shifts that do not increase with time). The reason that the frequency feedback loop is not correcting these phase shifts to zero is as follows: In 'FLL + Injection' mode of operation the magnetron is locked to the 10 MHz reference first so that it has the same frequency as the injection source, then the injection signal is introduced. The division ratio on RF output feedback is very large (12250) in order to achieve a 200 kHz step size. When the injection is not present the feedback loop works fine as there is enough phase/frequency shift to produce a reasonable error signal. When

injection locked, the small phase shift due to the ripple is still divided by the same large number (12250), consequently 13 degrees of phase error (at injection level of 500mW) reduces down to about a milli-degree after the divider. Due to this, the loop gain becomes very small and the feedback control makes little contribution to mitigate the phase shifts. When the magnetron's natural frequency drifts enough due to a change in the anode temperature so that the magnetron is about to unlock, it is then that the phase detector gives out enough error signal again and the feedback loop acquires the lock back by changing the anode current and moving to a different point on the pushing curve.

Increasing the voltage gain at the phase detector output or reducing the frequency division would make the loop gain too high when the injection signal is not present, the feedback loop would become unstable and magnetron would not frequency lock. The solution to this problem is to introduce a second feedback loop using a small frequency division ratio and adding the error signal to the control input of the power supply after the injection signal is introduced. This method is described in section 4.7.

4.5.3 Real Time 8 GHz Oscilloscope

A third independent measurement of the phase jitter in real time has been made using a Tektronics TDS6804B 8 GHz bandwidth and 20 GHz sampling rate Digital Storage Oscilloscope, with a persistence time of 1 second. The top traces in Figure 4.8a and 4.8b are the injection signals and the bottom traces are the magnetron output signals. The time jitter seen on the injection source mainly comes from the oscilloscope itself, as its sampling rate is 20 GSPS, which is only 8 times the output frequency (2.45 GHz). Results

give confirmation of the phase jitter measurements made with the phase detector, i.e. 13 degrees peak-peak phase jitter for 500mW injection level and 48 degrees peak-peak phase jitter for 50mW injection level.

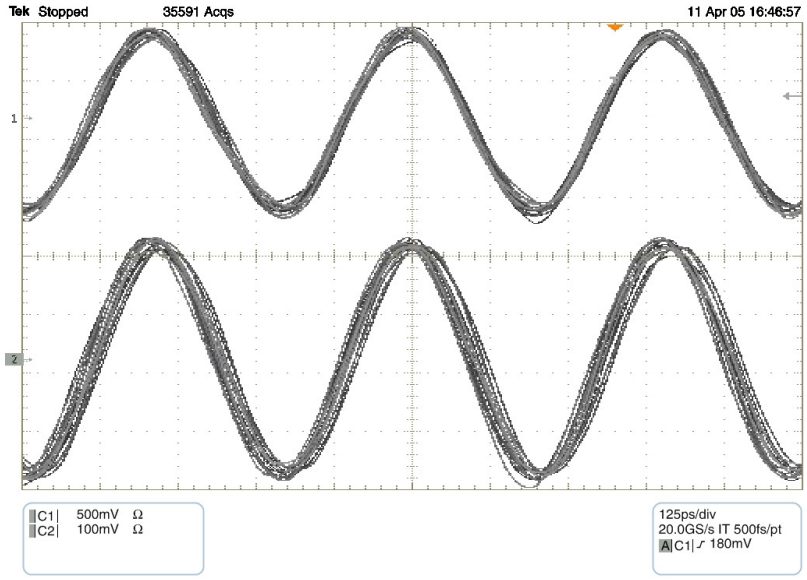

a (500mW Injection Level)

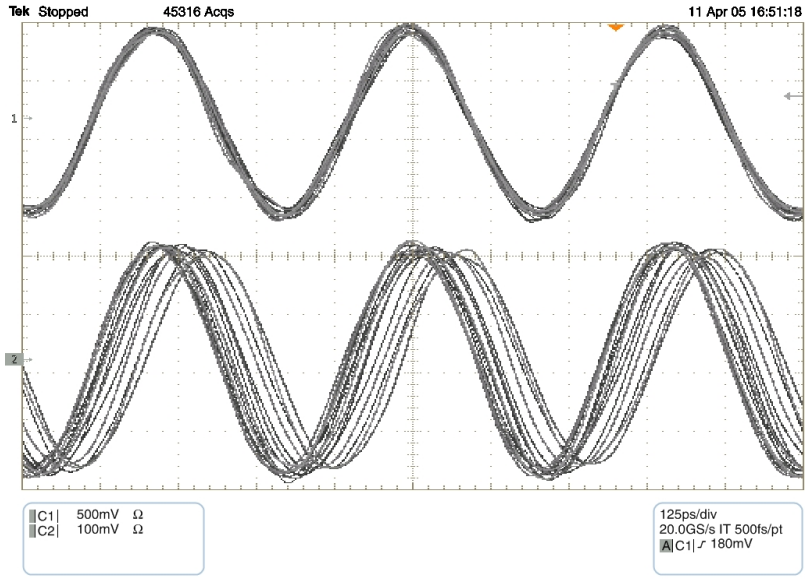

b (50mW Injection Level)

Figure 4.8 TDS6804B Results CH1 = Injection Signal CH2 = Magnetron Signal

4.6 Effect of the heater power on phase jitter

For the investigation of the effect of heater power on phase jitter an anode current of 280mA was chosen to allow injection locked FLL operation over almost all of the heater power range. An associated injection level of 1W (-29 dBc) was needed for the same reason.

Figures 4.9a, 4.9b and 4.9c show the frequency spectra of the magnetron output when working in a 'FLL + Injection' mode, for spans of 1 MHz, 100 kHz and 1 kHz. Noise present at 100 kHz offset from the carrier is -70 dBc when there is no heater power. Further away from this the noise floor decreases to -100 dBc at 500 kHz offset however there are sidebands at -75 dBc which are about 21.5 kHz apart from each other. This is half the switching frequency. They appear around and after the 200 kHz spikes which are due to the PFD comparison frequency. In Figure 4.9b for the 100 kHz span, the sideband at 43 kHz caused by the switching frequency of the power supply is -40 dBc and its sub-harmonic at 21.5 kHz is also at the same level. There are -30 dBc spikes 5 kHz from the centre and they seem to have shadows either side of the 43 kHz peaks. A value of 5 kHz is about the 8^{th} sub harmonic of the switching frequency and at high heater powers all sub harmonics are present. For the span of 1 kHz in Figure 4.9c the 100 Hz spikes at -20 dBc come from the rectified mains ripple. The 50 Hz component at about -40 dBc when the heater is off comes as a sub-harmonic of the 100 Hz ripple.

Turning the heater power up to 10W, does not add much noise in a wider span compared with the spectra with no heater power, and only contributes a couple of dB to the level of switching ripple and its sub-harmonics. However the 50 Hz component becomes 15 dB higher than before, and 100 Hz ripple also gains about 7 dB in its amplitude.

When the heater power is further raised to 32W the magnetron enters its space charge limited region. The sidebands at higher multiples of 43 kHz gain about 30 dB now bringing them to about -50 dBc. The switching ripple at 43 kHz only increases by 10 dB. There is about 6 dB increase in the 50 Hz spike, whereas the 100 Hz ripple only increases by 2 dB with respect to its level at 10W of heater power. The noise floor rises by 20 dB all the way from near carrier to 1 MHz.

As the heater power is further increased to 44W there is no significant change in the level of any of the sidebands. However we see an increase in random noise around the spikes and asymmetry of the spectrum increases.

Figure 4.9d shows the corresponding time domain plots of the phase difference between the magnetron output and the injection signal, measured with the digital phase detector HMC439. The Fast Fourier Transform (FFT) of the phase detector output is also shown on the right hand side of the Figure 4.9d. The top trace in each snapshot on the left in Figure 4.9d is the AC coupled anode current ripple labelled as CH1. The bottom trace labelled as CH2 is the digital phase detector output which is also AC coupled and 20 mV represents one degree of phase difference in this trace. With this scale (1^{o} / 20 mV) we get 4 degrees peak to peak phase shift due to 100 Hz ripple when there is no heater power, for an anode current 280mA and injection level of 1W (-29 dBc). The phase shift becomes

16^{o} peak to peak at 10W heater, 36^{o} peak to peak at 32W heater and drops to 32^{o} peak to peak at 44W heater power. The 50 Hz mains ripple from the heater power supply appears clearly both in the anode current and the phase detector output as the heater is turned up. Although not very significant but it is interesting to see the reduction in the peak to peak value of the phase difference when the heater is turned up from 32W to 44W. It can also be seen in the spectrum in Figure 4.9c where sidebands at 100 Hz and 50 Hz for 44W are a couple of dB less than that for 32W on the RHS of the carrier. The amount of phase shift we get for a change in the anode current depends upon the corresponding change in the magnetron's natural frequency which is determined by the slope of the pushing curve for that range of the anode current. Figure 4.10 shows pushing curves as a function of the heater power measured with an injection locked magnetron. Correction for increasing anode temperature with anode current has not been made. The pushing curve for 33W heater power has a bigger slope for the anode current in the region 270 mA to 300 mA compared with 36W heater power. This explains the reduction in the peak to peak phase jitter for 36W heater power as compared to that for 32W in Figure 4.9d (anode current is 280 mA).

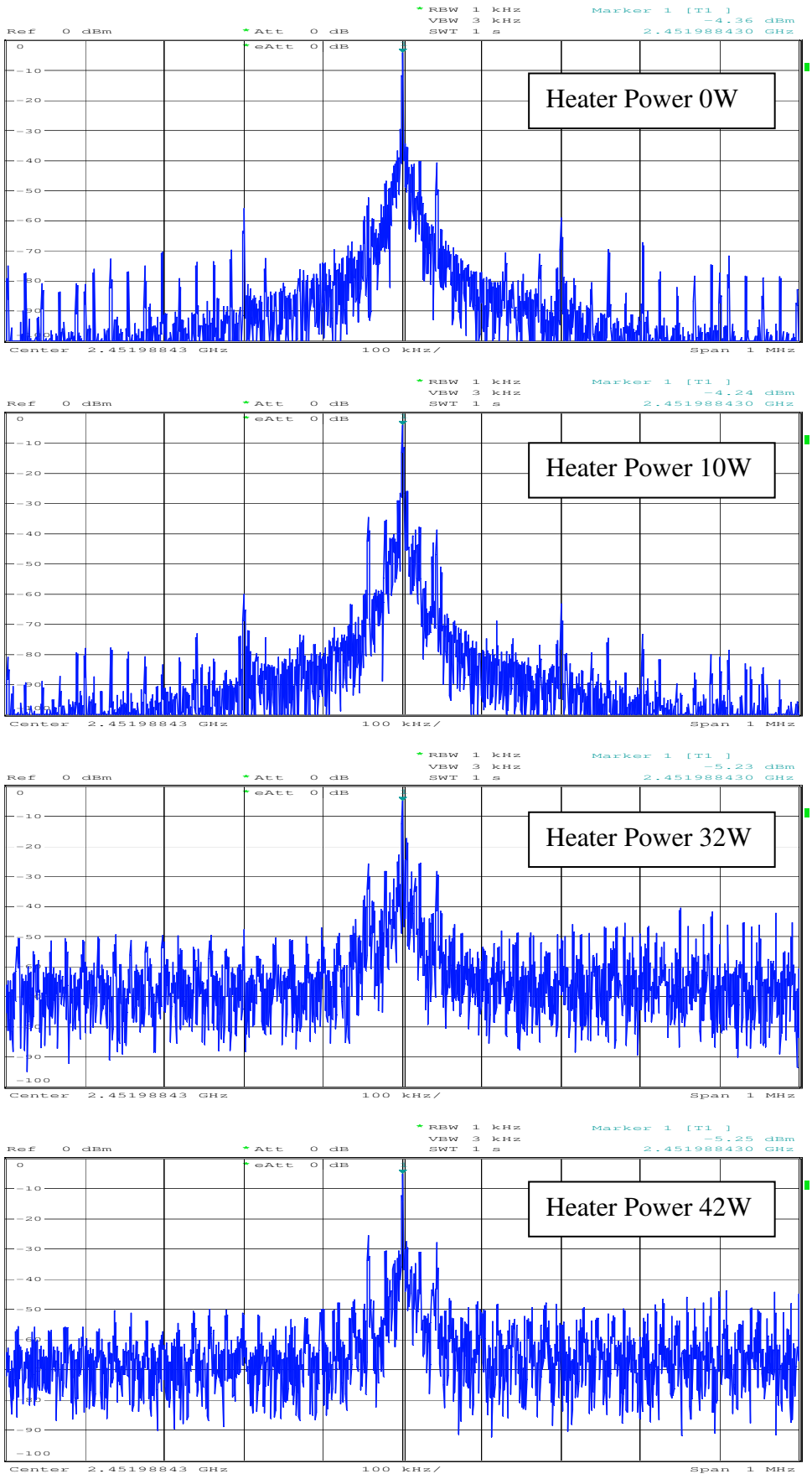

Figure 4.9a Effect of Heater Power FLL + Injection Mode, Span 1 MHz, 1W Injection Level(-29 dBc)

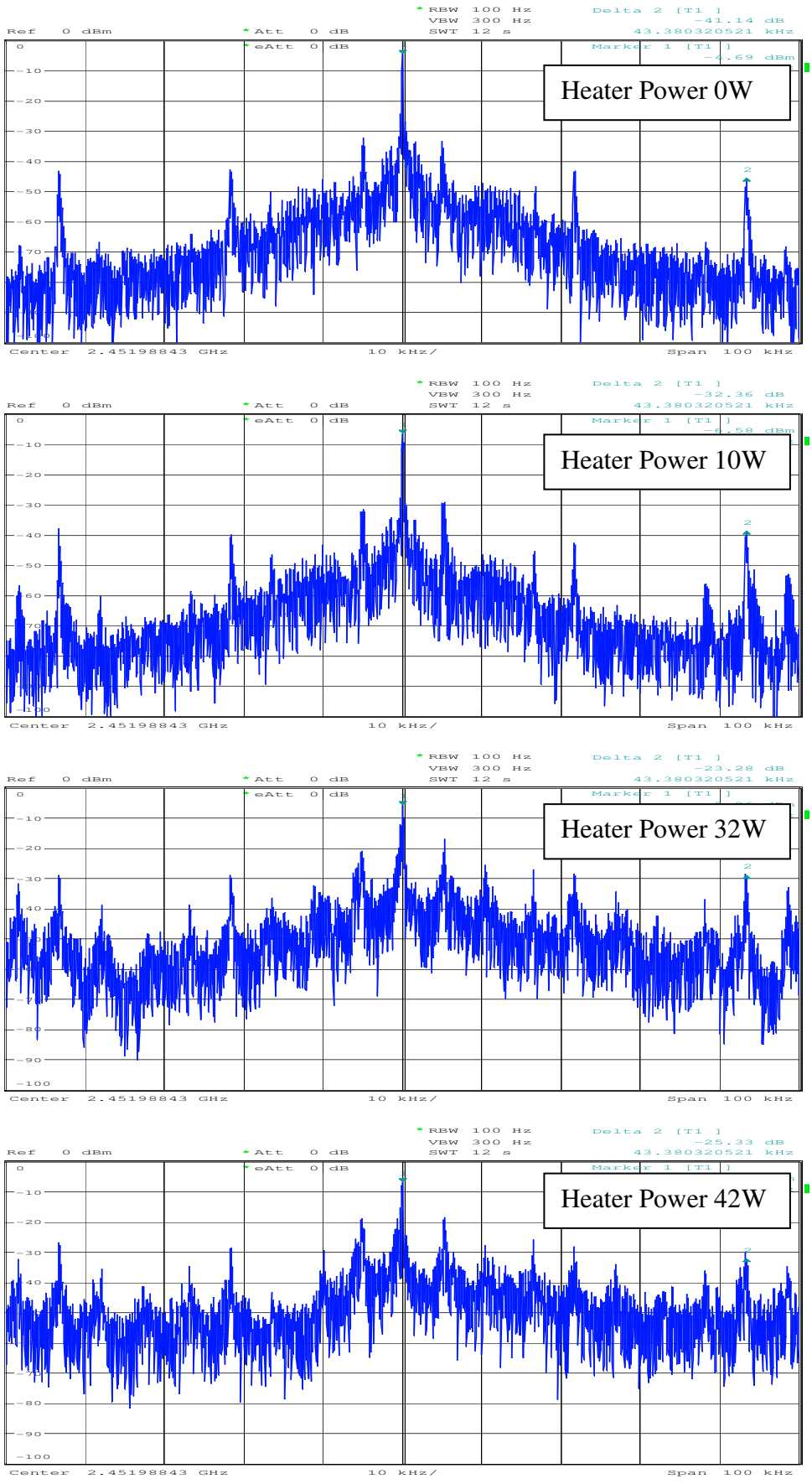

Figure 4.9b Effect of Heater Power, FLL + Injection Mode, Span 100 kHz, 1W Injection Level (-29 dBc)

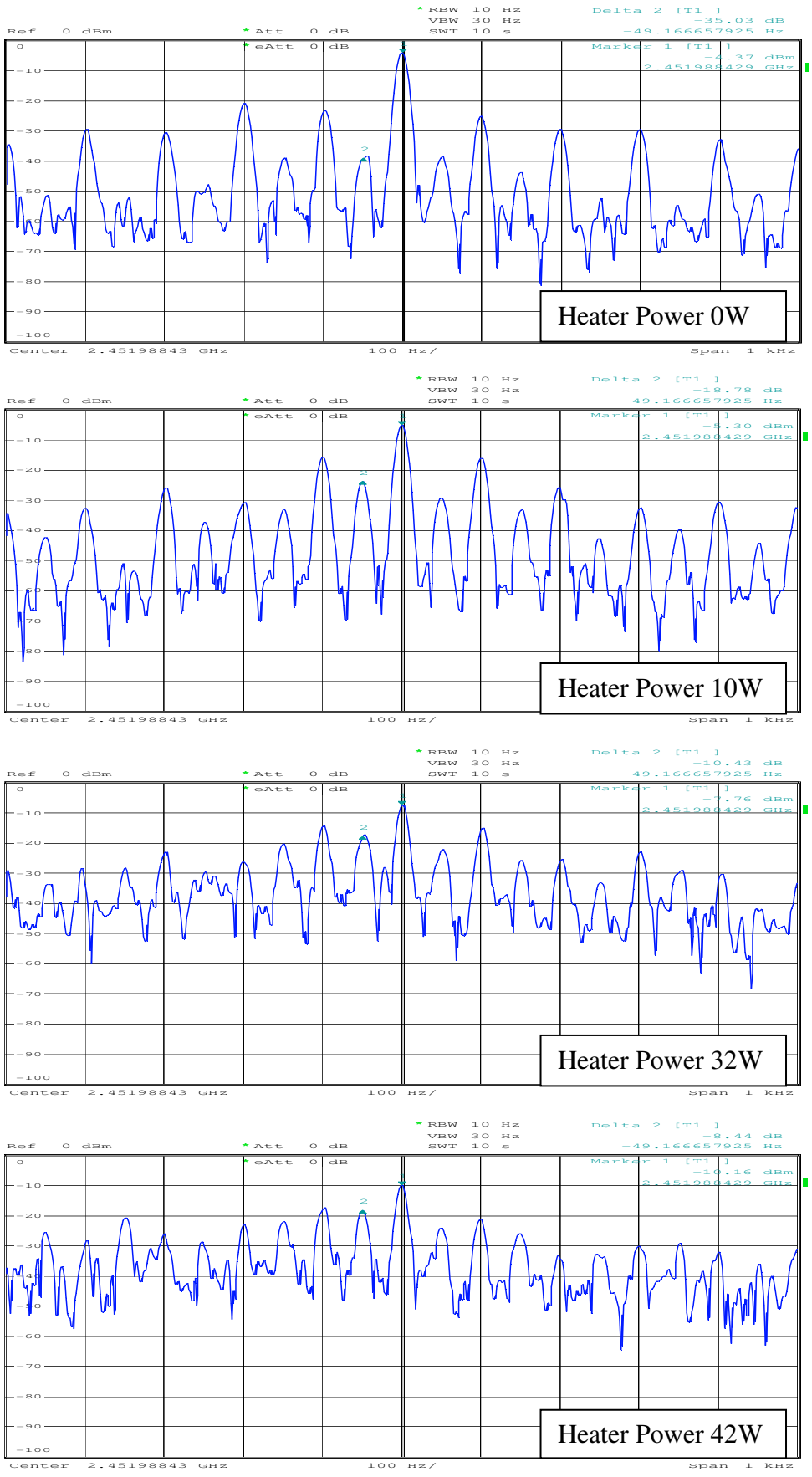

Figure 4.9c Effect of Heater Power FLL + Injection Mode, Span 100 Hz, 1W Injection Level(-29 dBc)

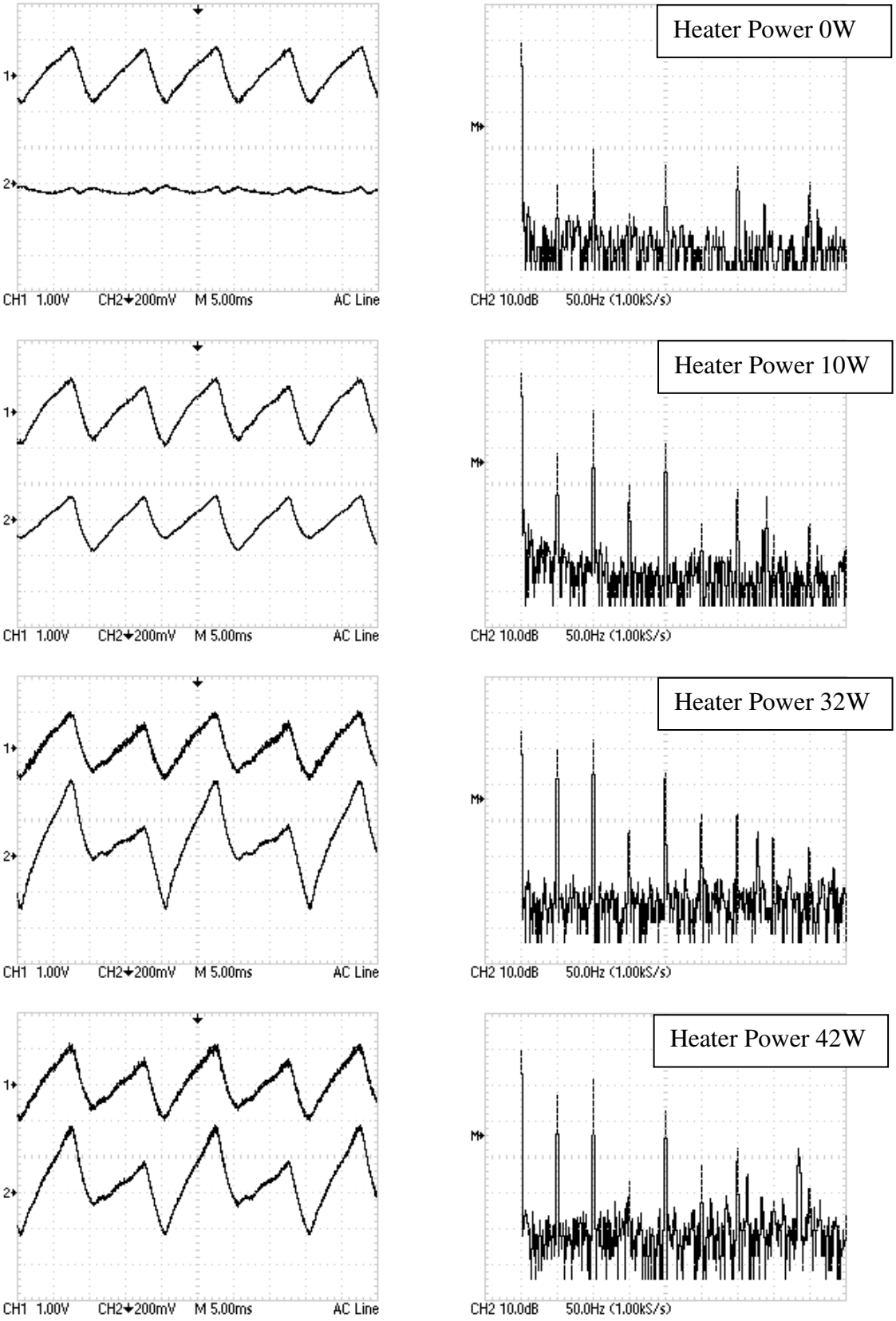

CH1 = Anode current in time domain

CH2 = Phase in time domain CH2 = FFT of CH2 on LHS

Figure 4.9d Effect of Heater Power FLL + Injection Mode, (Scale : 20mV = 1 degree)

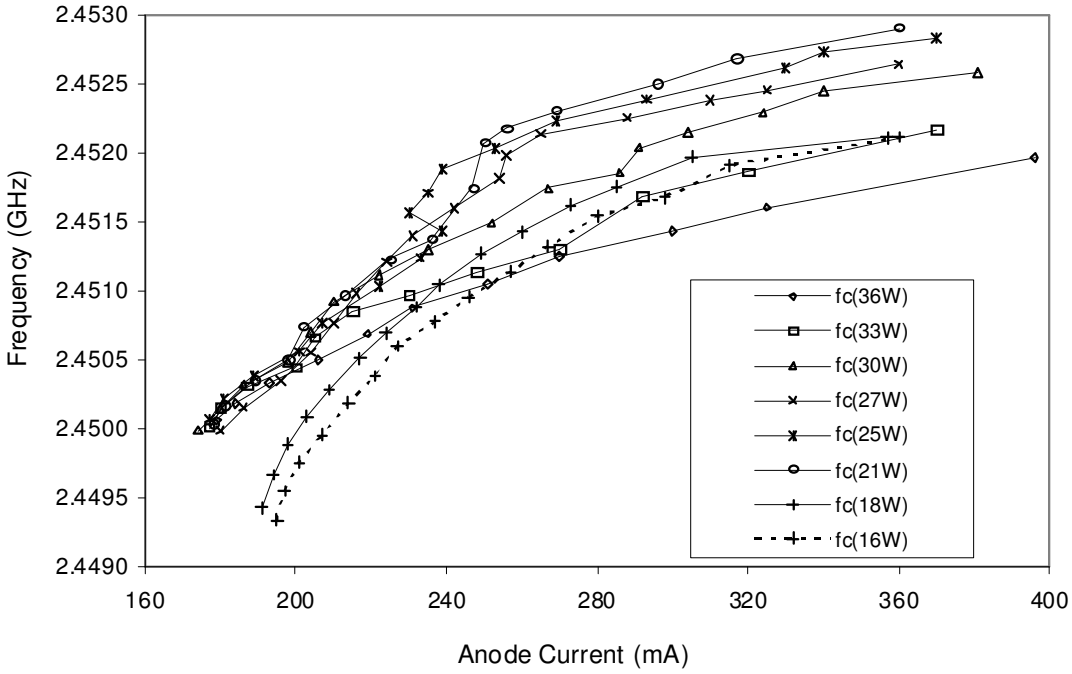

Figure 4.10 Pushing curves as a function of heater power for an Injection locked magnetron

4.7 Second Feedback Loop to control for the phase jitter

As mentioned in section 4.5 the frequency feedback loop gain becomes very small due to a high division ratio on the magnetron RF output frequency when the injection signal is introduced, hence it cannot correct for the phase shifts produced by the anode current and heater power ripples. This problem is solved by incorporating a second feedback loop which consists of a high speed 1.3 GHz digital phase detector HMC439 from Hittite Microwaves, along with two frequency dividers as shown in Figure 4.11. A division ratio for the magnetron RF output is set to two so that the input frequency to the detector is nominally 1.225 GHz. This division is required as the maximum input frequency of operation for the phase detector is 1.3 GHz.

The gain of the loop is too high for frequency locking operation without injection hence a switch shown as ‘S’ in Figure 4.11 is provided to make sure that the second loop is turned on after the injection signal is introduced. A manual phase shifter is placed between the injection signal and 1W amplifier. For Proportional Integral control, an RC integrator is introduced at the output of the phase detector. The phase error signal after the integrator is applied to the power supply input through a voltage adder circuit. An adjustable resistor R1 is provided to obtain a suitable voltage level for the power supply input.

For a heater power of 10W and an anode current of 280 mA results are shown in Figure 4.12. The top trace is the anode current ripple, the middle trace is the phase error at the phase detector output when the switch S is open (second feedback loop not operating). The bottom trace is the phase error when switch S is closed (i.e. second feedback loop is operating). Residual phase error in the bottom trace is due to the limited bandwidth set on the RC integrator so that it is much less than the power supply switching frequency. The loop bandwidth for the second loop is about 2 kHz with R = 1 kΩ and C = 80 nF. The frequency is high when the 100 Hz ripple changes the direction of its slope and we get only a correction factor of 10 on the peak to peak phase error with 2 kHz bandwidth.

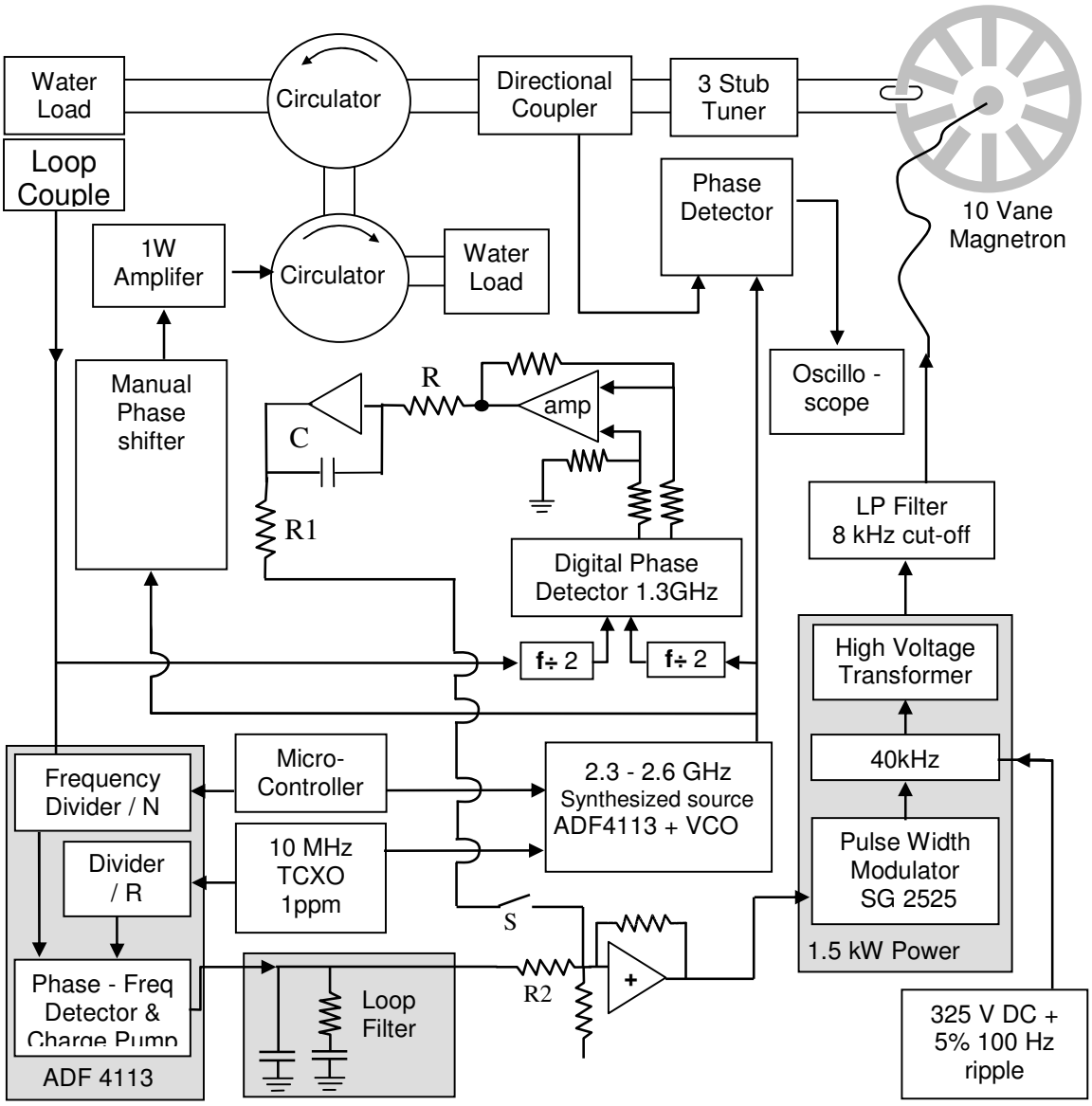

Figure 4.11 Experimental Setup for the second feedback loop

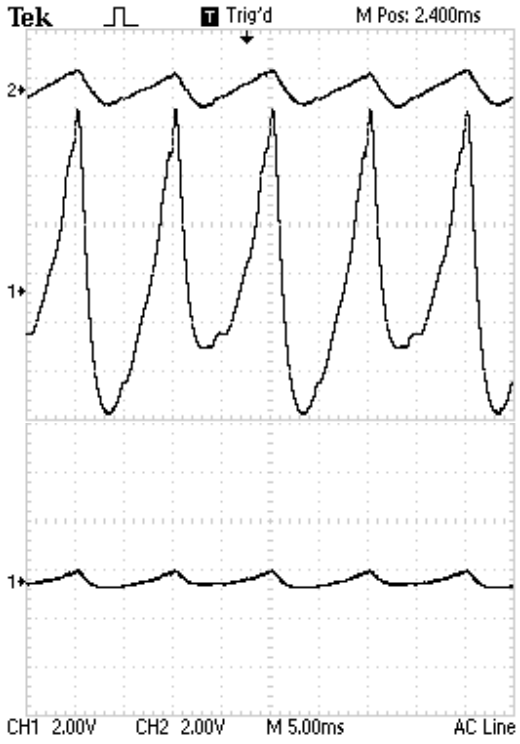

Figure 4.12 Effect of the second feedback loop on phase error.

Top trace: Anode current ripple,

Middle Trace: Phase error without 2nd feedback loop, +/-18° Peak-peak

Bottom Trace: Phase error with 2nd feedback loop, +/-1° Peak-Peak

(CH1 Scale: 6° degrees / Big Division)

In this chapter we have seen the effects on the injection locked magnetron phase when its natural frequency drifts away from the injection signal's frequency. It would be interesting to find out the magnetron response when the injection signal phase is changed or stepped from its previous steady state value. This is discussed in detail in Chapter 5.

Chapter 5

PHASE MODULATION OF THE MAGNETRON

We have seen in chapter 4 that when an injection signal is introduced into the magnetron output and the lock occurs the difference of phase angle between the magnetron output and the injection signal θ is determined by a solution of (4.19). Substituting (4.14) and (4.20) in (4.19) gives

$$\frac{d\theta}{dt} = -\frac{\omega_o (G + jB)\left(\frac{I_i}{I} + \frac{V_i}{V}\right)}{2Q_{ext}} \sin\theta + \omega' - \omega_i \tag{5.1}$$

If the injection source has an approximate match to the characteristic impedance of the magnetron anode then

$$\frac{V_i}{I_i} \approx \frac{1}{Y_o} = \frac{V}{I} \tag{5.2}$$

where Y_o was previously defined as the ratio I/V in (4.8). This means that

$$\frac{I_i}{I} \approx \frac{V_i}{V} \tag{5.3}$$

hence for a matched injection source (5.1) can be written

$$\frac{d\theta}{dt} \approx -\frac{\omega_o (G + jB)\frac{V_i}{V}}{Q_{ext}} \sin\theta + \omega' - \omega_i \tag{5.4}$$

Equation (5.4) shows how the angle θ will vary if the injection phase is perturbed from its steady state value. By stepping the injection phase between two values, we can obtain

important information about the speed at which the magnetron can follow the injection signal's phase. The experimental setup for this is shown in Figure 5.1.

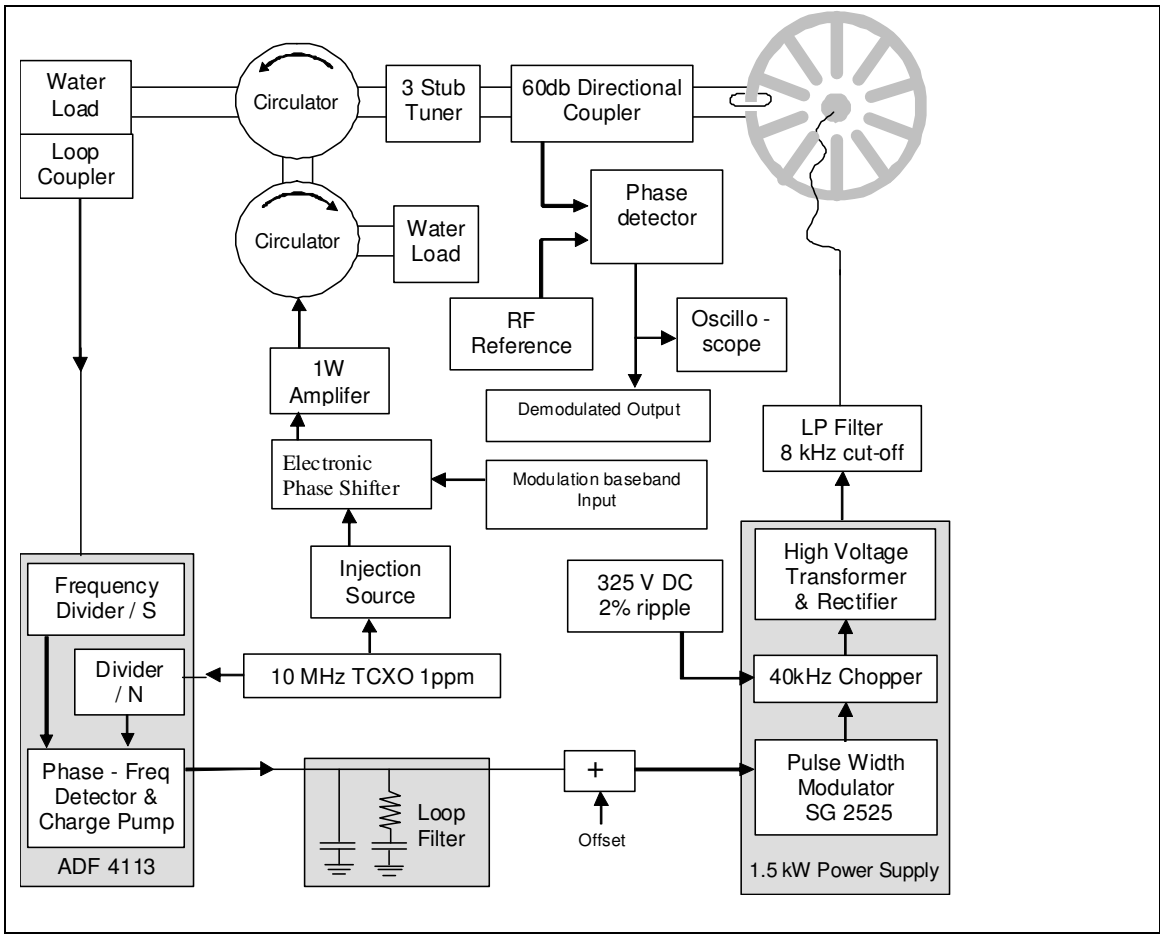

Figure 5.1 Experimental setup for the phase modulation of the magnetron

5.1 Effect of input parameters on Phase Modulation with Matched Load

Injection source used in the setup of Figure 5.1 is the same as described in Chapter 4. For the purpose of phase modulation an electronic phase shifter is inserted after the source. A control signal applied to the phase shifter control input modulates the phase of the RF

signal passing through it. The control signal used is a square wave at 0.5 MHz which, in telecommunication terminology, can be regarded as 1 MBPS data input rate. The upper trace in Figure 5.2 gives the voltage levels of the square wave applied to the phase shifter and the bottom trace is the phase detector output when the phase modulated injection signal is compared with the RF source.

When the voltage on the phase shifter input, top trace (channel 1) in Figure 5.2, goes low, the phase is retarded (delayed) through the phase shifter and when it goes high, the phase is advanced. The peak-peak voltage levels and the DC offset of the control input are adjusted (as shown in top trace Figure 5.2) so that a 90^{o} of peak-peak phase shift across the phase shifter is obtained.

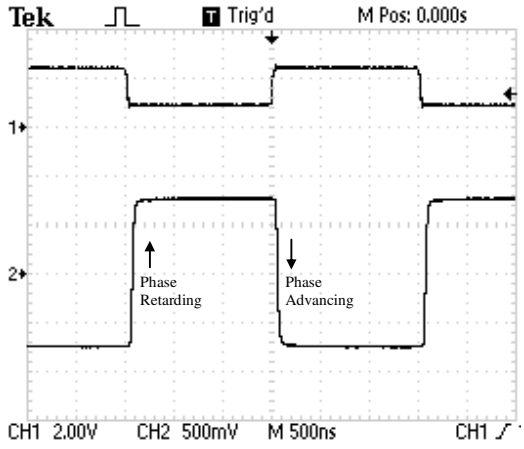

Figure 5.2 Control input of the phase shifter (CH1) and corresponding phase shift through the electronic phase shifter (CH2) (measured between the phase shifter output and the injection source by the Digital Phase Detector)

The frequency spectrum of this 90^{o} phase modulated Injection signal is shown in Figure 5.3. Two side bands with magnitudes the same as the carrier amplitude appear at an offset equal to the modulation frequency when the phase modulation has a square wave format with very small rise and fall time. (Note that were the modulation to move from being square towards being a symmetric triangular shape then spectral analysis would show sidebands with reduced amplitude; were the triangular wave form to become asymmetric then one sideband become higher in amplitude than the other.)

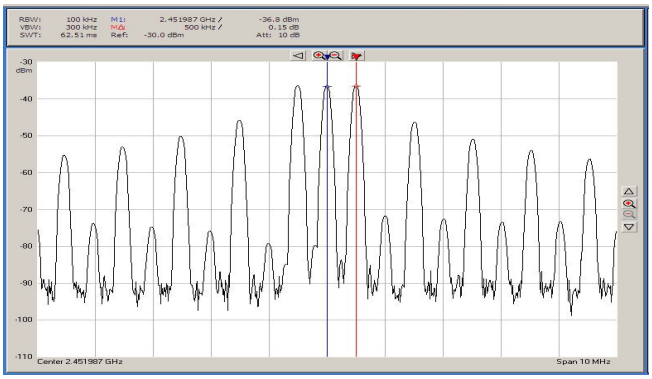

Figure 5.3 Spectrum of the magnetron injection signal associated with Figure 5.2

The phase modulated signal is amplified and injected into the magnetron output waveguide through two circulators as shown in the arrangement in Figure 5.1. The magnetron output was matched with a 3-stub tuner so that the reflection level was -50 dBc. The anode current and magnetron output phase were measured for different magnetron input parameters and the results are summarised in Figures 5.4 – 5.9. In these figures the top trace is the phase difference between the modulated injection signal and the RF source. The second trace is the phase difference between the RF source and the

magnetron output taken through a 60 dB loop coupler. The third trace (solid) is the corresponding anode current measured across a 47 Ω resistance placed between the magnetron anode and the ground (the zero for this trace is the dashed line). The fourth trace is anode current again but on an expanded scale which allows us to clearly see the changes in the anode current as the injection phase is changed. It is important to note the encircled label (Volts/Div) for the fourth trace because a different scale has been used to show the best possible resolution on the anode current. For the third trace the scale (Volts/Div) is the same in all the figures. All the traces were triggered with respect to the control input (base-band) applied to the electronic phase shifter, top trace in Figure 5.2. Phase offsets due to the 50 Hz heater ripple and the 100 Hz mains ripple are filtered out at the phase detector output with a high pass filter and only desired phase modulation results are recorded.

5.1.1 Effect of rate of change of Injection Signal's phase

The rate of change of phase of the injection signal shown in Figure 5.2 is very high. In order to interpret our observations of the phase modulated magnetron RF output we begin by considering a triangular phase modulation rather than a square modulation so that the injection phase varies steadily. A steady variation of the injection phase implies that the injection frequency is higher/lower than the reference frequency by a fixed step. For the results of Figure 5.4a we have used symmetric triangular waveform where the phase retards from 0 to $\pi/2$ in 1 μs and then advances from $\pi/2$ back to 0 again in 1 μs. This gives us $0.5\pi/\mu s$ rate of change in phase for both advancing and retarding.

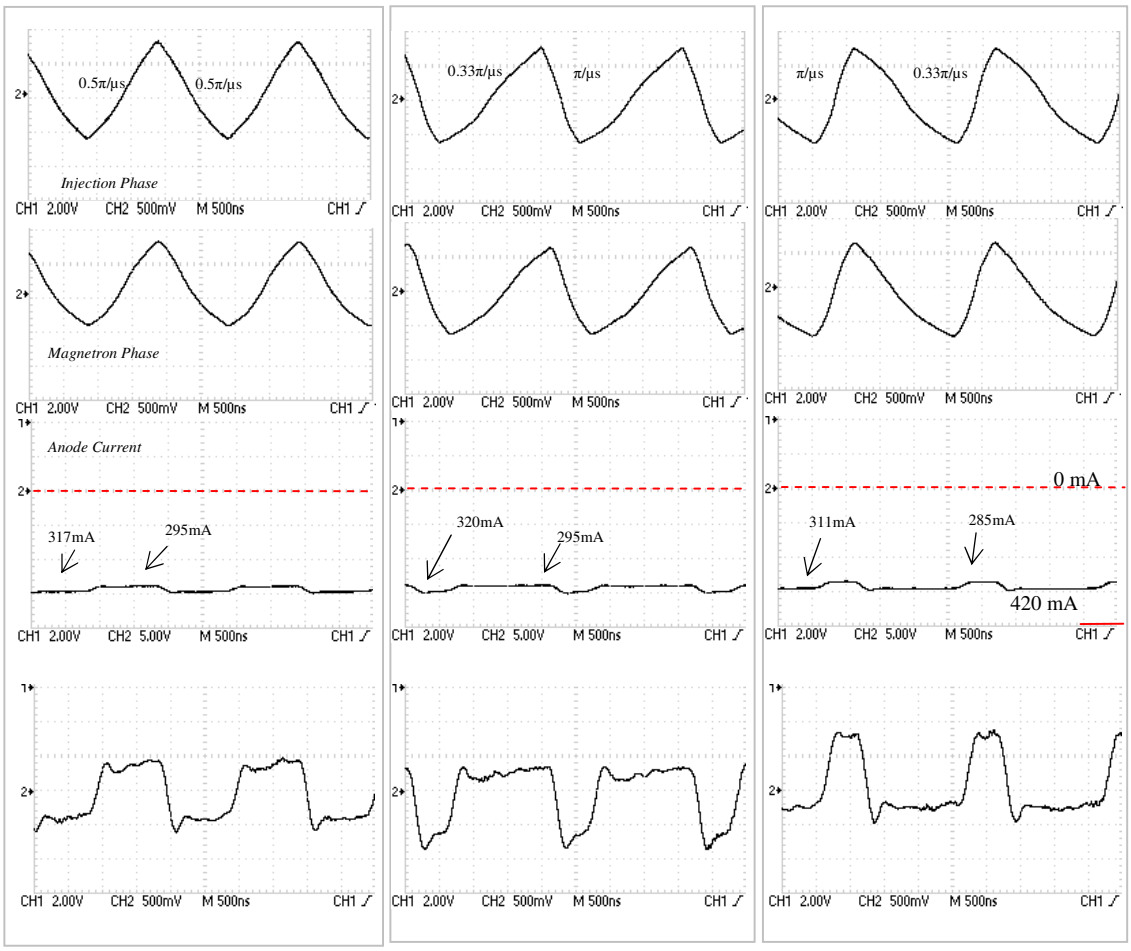

(a) (b) (c)

Figure 5.4 Phase ramping at different rates (Heater 44W, -29dbc Injection level)

We observe a step increase in the anode current as the injection phase switches its gradient in the triangular waveform i.e. the frequency changes by a fixed step. The magnetron acquires the new frequency of the injection signal in a short period and the anode current's final value changes. One might expect that this change can be predicted by the pushing curve. In Figure 5.4a the total frequency step between the increasing and the decreasing phase is 500 kHz and anode current changes between 295 mA and

319 mA. From the steady state pushing curves for a free running magnetron as given in Figure 2.4 there is only about 200 kHz frequency change for this anode current change. Figure 2.4 has a different (steady) anode current for each frequency and hence the anode temperature will be different for each point. This pushing curve does not apply for rapid changes in the anode current. Temperature independent pushing data can be determined as the dependence of frequency on temperature has been measured to be 40 kHz per degree Centigrade, (see Chapter 2). Figure 5.5 gives temperature independent pushing curves derived from the data of Figure 2.4. Near to 300 mA the gradient in this figure is 17 kHz per mA, hence for a frequency step of 500 kHz we expect an anode current change of 30 mA. An anode current change of 22 mA was measured.

In Figures 5.4b and 5.4c an asymmetric rate of change is used for injection phase advancing and retarding so as to illustrate the magnetron response at higher and lower injection phase gradients. Figures 5.4b and 5.4c show anode current response for phase gradients of 0.33 $\pi/\mu s$ and 1.0 $\pi/\mu s$. These phase gradients correspond to 165 kHz and 500 kHz respectively, hence a total frequency difference of 665 kHz. From the pushing curves of Figure 5.5 we expect an anode current variation of 39 mA. An anode current change of 26 mA was observed.

Figure 5.4 also shows that it takes the anode current about 150ns (about 360 RF cycles at 2.45 GHz) to settle to a new value after the frequency has been changed. Interestingly the time taken for the anode current step remains about the same for all the cases in Figure 5.4 and Figure 5.6. The anode current peak values are labelled with arrows in all figures.

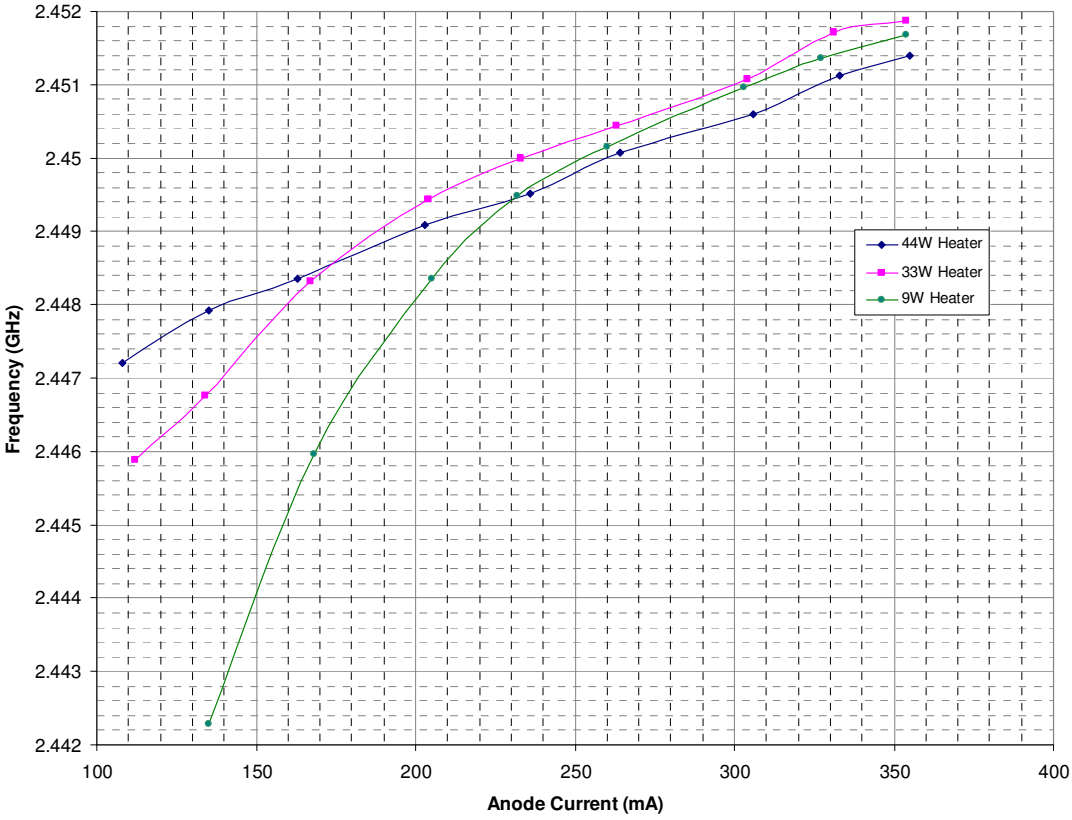

Figure 5.5 Pushing Curves with matched load (Temperature corrected)

Figure 5.6 gives results for 2π/μs and 0.25π/μs and hence a frequency step of 1125 kHz. From the pushing curves of Figure 5.5 we expect an anode current variation of 66 mA. The phase advance of 2π/μs is not held for a long enough period for the associated anode current to be determined. In this figure overshoot of the anode current when it settles to a new value is larger compared to Figure 5.4.

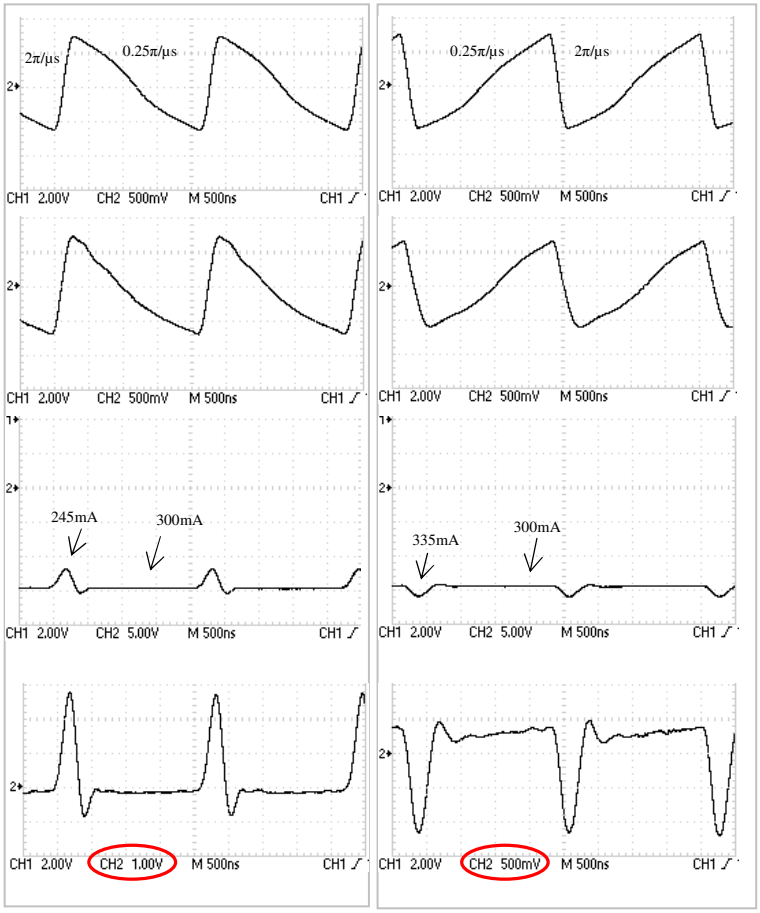

(a) (b)

Figure 5.6 Phase ramping at different rates (Heater 44W, -29dbc Injection level)

In Figure 5.6 when the phase retards with the gradient of 2π/μs the anode current drops by 65mA whereas when the phase advances with the same rate the anode current increases by only 35mA.

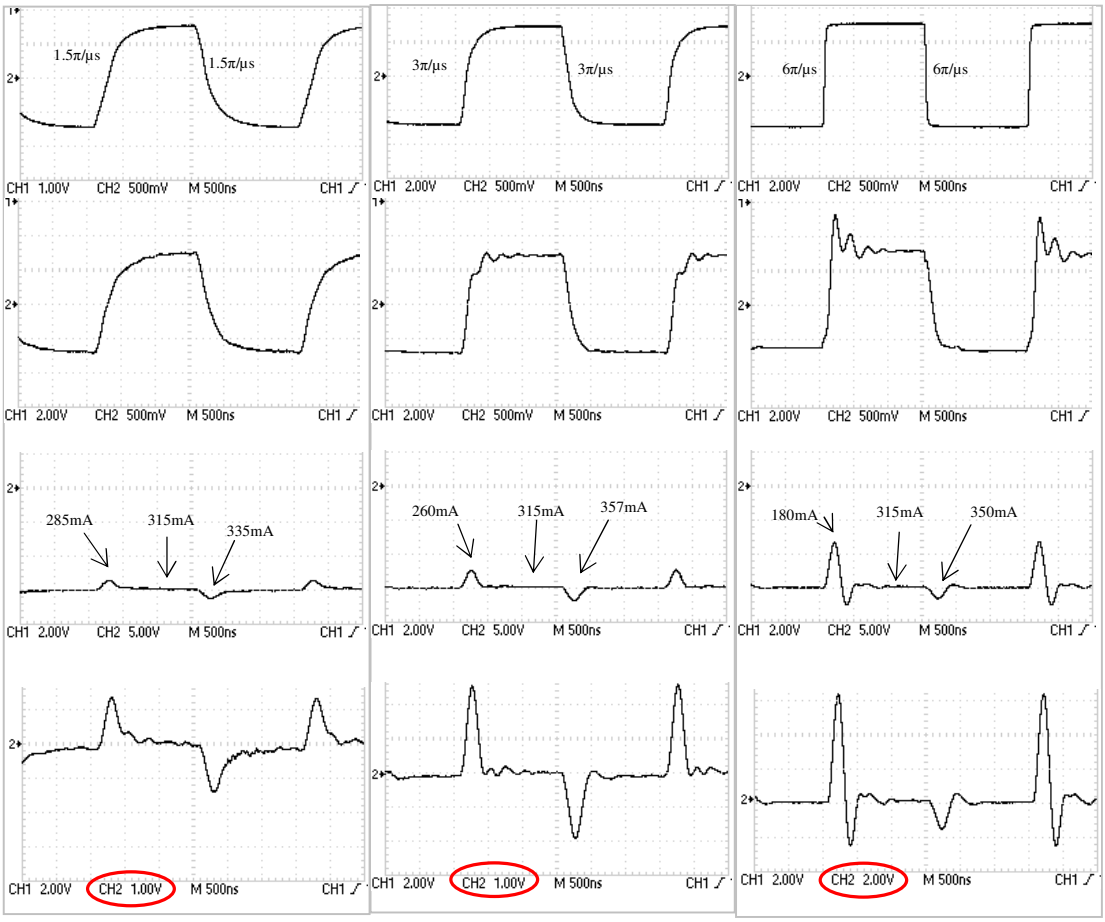

(a) (b) (c)

Figure 5.7 Injection Phase stepping at different rise and fall rates (Heater 44W, -29dbc Injection level)

In order to further investigate the transient response of the injection driven magnetron, the effect of 90^{o} phase switching with deducing rise and fall times was recorded as shown in Figures 5.7a-c. In Figure 5.7a where the phase change rates is 1.5π/μs the magnetron follows the injection phase both for phase advancing and phase retarding. When the phase is switched faster at 3π/μs (1.5 MHz) as shown in Figure 5.7b the magnetron's phase follows injection phase for advancement (downwards) and has a transient departure on

retardation (upwards). When the phase is switched faster still at 6π/μs (3 MHz), as shown in Figure 5.7c, the magnetron's phase lags the injection phase for advancement (downwards) and has large a transient departure with a smaller lag on retardation (upwards).

When the phase is retarded at the rate of 6π/μs (3 MHz) the magnetron responds at 4π/μs (2 MHz). When the phase is advanced at the rate of 6π/μs (3 MHz), the magnetron responds at 3π/μs (1.5 MHz). The time taken by the anode current to reach its peak in either case remains the same as mentioned previously which is 150 ns. The anode current comes back to its centre value as the magnetron phase becomes equal to the new injection phase. For phase retardation we see an under-damped oscillatory response in the anode current which is similar to that of a second order system when perturbed from equilibrium.

5.1.2 Effect of the heater power

Further experimental observations revealed that the damping of the injection driven magnetron response (both RF and anode current) also depends upon heater power, injection signal level and steady state anode current. Results for phase modulation with three different heater powers 44W, 33W and 9W are presented in Figure 5.8. There is less damping in the anode current oscillation when the heater power is higher. As the heater power decreases one expects the Brillouin hub (sub-synchronous charge layer) to shrink and this is likely to be why the damping increases. The magnetron output phase changes faster when the anode current oscillation is bigger and vice versa.

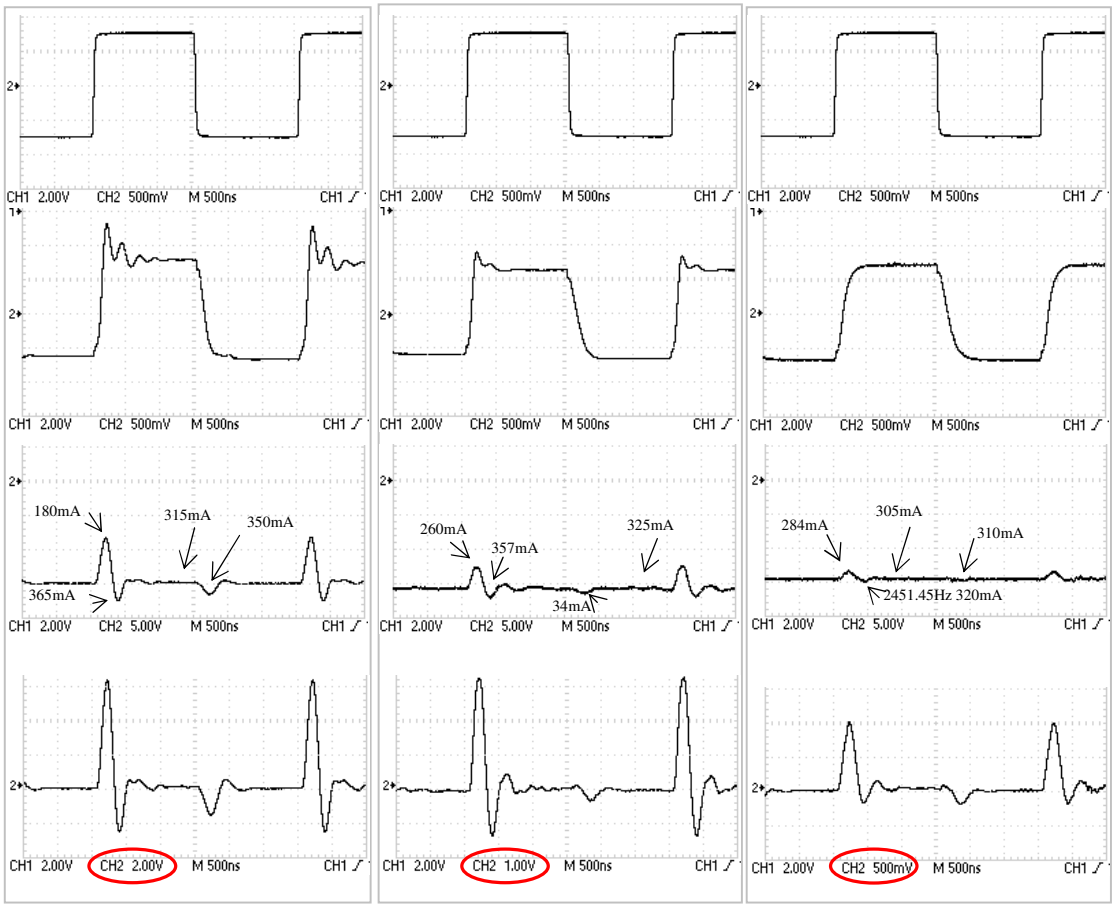

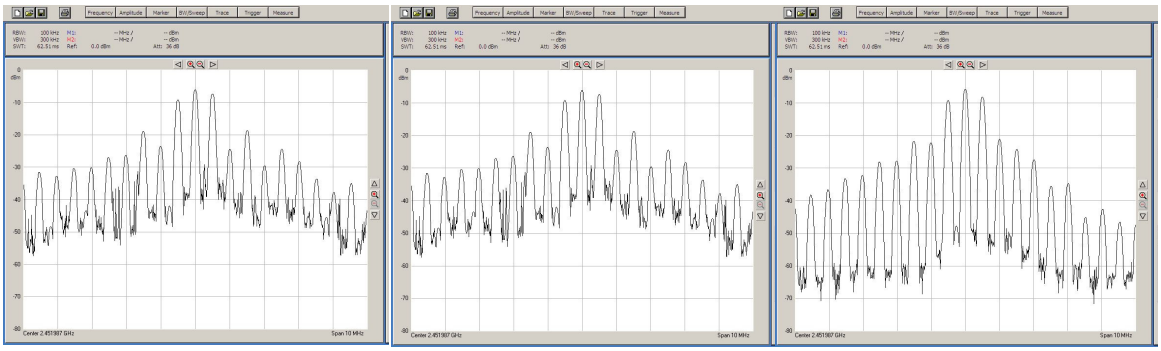

(a) 44W (b) 33W (c) 9W

Figure 5.8 Phase modulation with different heater power levels (Injection Level -29dBc, Anode current 315mA)

Spectral plots for the magnetron output are also shown in Figure 5.8. Notice that the two side peaks are lower than the centre peak as a consequence of the magnetron output not being a perfect square wave. The two side peaks are not equal because of the difference in the rate of phase change for advancing and retarding. The expanded ac-coupled anode current in 4th trace gives further illustration of the shape and frequency of the oscillatory response. The time for the quarter cycle of this under-damped oscillation is still roughly 150 ns. This behaviour is in fact very similar to the response of an RC network to a step change in the applied voltage where the time to reach the steady state remains constant irrespective of the amplitude of the voltage step. The oscillation appearing on the phase is synchronised to that on the anode current.

The oscillations in the anode current as well as the magnetron phase are due to the complex nature of the interaction between the space charge in the Brillouin hub and the RF wave. The process as best we understand it proceeds in the following order. As the injection phase starts to ramp the phase of resultant field in the anode resonant circuit also starts to ramp but with a greatly reduced rate. The phase change in the anode circuit is the same as a phase change for the RF hence the angle between the RF peak and the charged spoke (defined as angle α in Chapter 2) changes by a very small amount. This has two simultaneous effects, one is a small change in the net effective capacitance of the anode block hence a further small change in the natural frequency of oscillation, the other is a small change in the anode current due to the position of the spoke with respect to the RF peak. The change in the natural frequency changes the angle α a bit more, resulting in a further change in the anode current and a further change in the natural frequency. This

process of growth of the natural frequency carries on till it acquires the new injection phase (or injection frequency if the injection phase continues to ramp)

The interdependency of the angle α (defined in Chapter 1) and the instantaneous phase difference between the magnetron oscillation and the injection signal (defined as θ in Chapter 4) has been mentioned by Chen [63] who modelled frequency pushing effects in magnetron phase locking using the lumped circuit model of Chapter 4. Chen modelled the magnetron's admittance as

$$g = \frac{1}{R}\left(\frac{V_{DC}}{V_{RF}} - 1\right) \tag{5.5}$$

$$b = b_o - g.\tan\alpha_c \tag{5.6}$$

suggesting that α_c is very closely related to the angle α between the RF wave and the spoke. Slater justifies the use of (5.5) and (5.6) from experimental measurements [29]. Welch's model [3] where the effective capacitance between the spoke and the anode depends on α suggests that $\alpha \propto \alpha_c$ for small α.

Equation (5.5) (the ratio of RF current and RF voltage) gives the in-phase component of the RF current which governs the time varying RF growth. The value of b given by (5.6) affects the output frequency via (4.20).

Introducing (5.5) and (5.6) into (4.15) and (4.19) one obtains equations governing the amplitude and frequency evolution of the injection locked magnetron as:

$$\frac{V_{DC}}{V_{RF}} = 1 + \omega_o RC\left(\frac{1}{Q_o} + \frac{G}{Q_{ext}} + \frac{A\cos\theta}{Q_{ext}}\right) \tag{5.7}$$

$$\frac{d\theta}{dt} = \omega_o \frac{A}{2Q_{ext}}\sin\theta + \left(\omega_o - \omega_o \frac{B}{2Q_{ext}} + \frac{b_o - g\tan\alpha_c}{2C}\right) - \omega_i \tag{5.8}$$

Equation (5.8) still contains g hence using (4.15) gain gives

$$\frac{d\theta}{dt} = \frac{\omega_o}{2}\left\{\frac{A}{Q_{ext}}\sin\theta + 2 - \frac{B}{Q_{ext}} + \frac{b_o}{C\omega_o} - \left(\frac{1}{Q_o} + \frac{G}{Q_{ext}} + \frac{A}{Q_{ext}}\cos\theta\right)\tan\alpha_c\right\} - \omega_i$$

hence

$$\frac{d\theta}{dt} = \frac{A\omega_o}{2Q_{ext}}\frac{\sin(\theta - \alpha_c)}{\cos\alpha_c} + \frac{\omega_o}{2}\left\{2 - \frac{B}{Q_{ext}} + \frac{b_o}{C\omega_o} - \left(\frac{1}{Q_o} + \frac{G}{Q_{ext}}\right)\tan\alpha_c\right\} - \omega_i \tag{5.9}$$

Equation (5.7) shows that instantaneous RF voltage of the injection driven magnetron depends upon $\theta(t)$ (difference between injection phase and magnetron phase). Assuming $\alpha \approx \alpha_c$ then from (5.4) we see that $\theta(t)$ itself depends upon the angle a between the spoke and instantaneous RF voltage peak. Equation (5.9) does not appear as a second order equation for θ however one expects the angle α to have an independent time constant that depends on the dynamics of the space charge.

It is interesting to notice the asymmetry of the anode current oscillation for phase retarding and advancing in Figure 5.8. When the phase is advanced, there is a step increase in frequency and the spoke moves towards the middle of the cavity. It is interesting to note from Figures 5.7 and 5.8 that there is an overshoot in the magnetron phase when peak of the anode current oscillation is more than 13%. We do not see an effect of the anode current oscillation in the magnetron phase when it is less than 13%.

5.1.3 Effect of the Injection level

The rate at which the magnetron acquires the new step change in the injection phase also depends upon the level of the injection signal which is obvious from Equation (5.4). Figure 5.8 shows the magnetron response with 3 different injection levels -29 dBc (1W), -32 dBc (500mW) and -35 dBc (250mW). The heater power of 33W for this part of the experiment is chosen because injection locking does not work very well for 44W heater power when the injection level is below 1W. The effect of 50 Hz and 100 Hz ripples in the magnetron output phase becomes too high and makes it almost impossible to record presentable results. Working with injection levels significantly higher than -30 dBc would have been a diversion from the main aim of the thesis, i.e. to investigate phase performance of a weakly driven injection locked magnetron with pushing based frequency control.

As the injection level drops, the rate of change of the magnetron phase reduces and the level of oscillation in the anode current also decreases. A larger injection level results in a slightly bigger resultant field in the anode circuit and perhaps due to this the time varying growth process reaches its set point quicker than it would with a lower injection level.

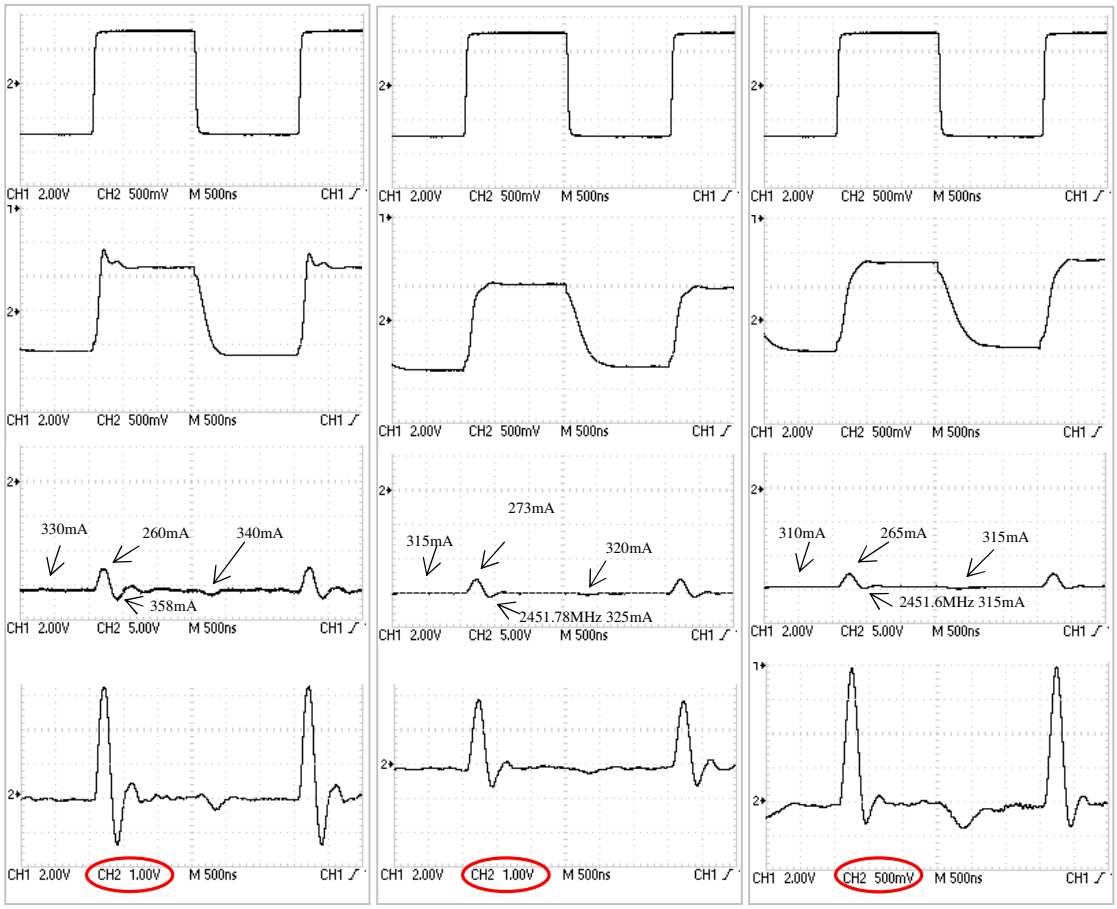

(a) -29 dBc (b) -32 dBc (c)-35 dBc

Figure 5.8 Phase Modulation with different Injection levels (Heater power 33W)

5.1.4 Effect of the anode current level

Figure 5.9 shows this transient response for differing anode currents of 317 mA, 265 mA and 210 mA.

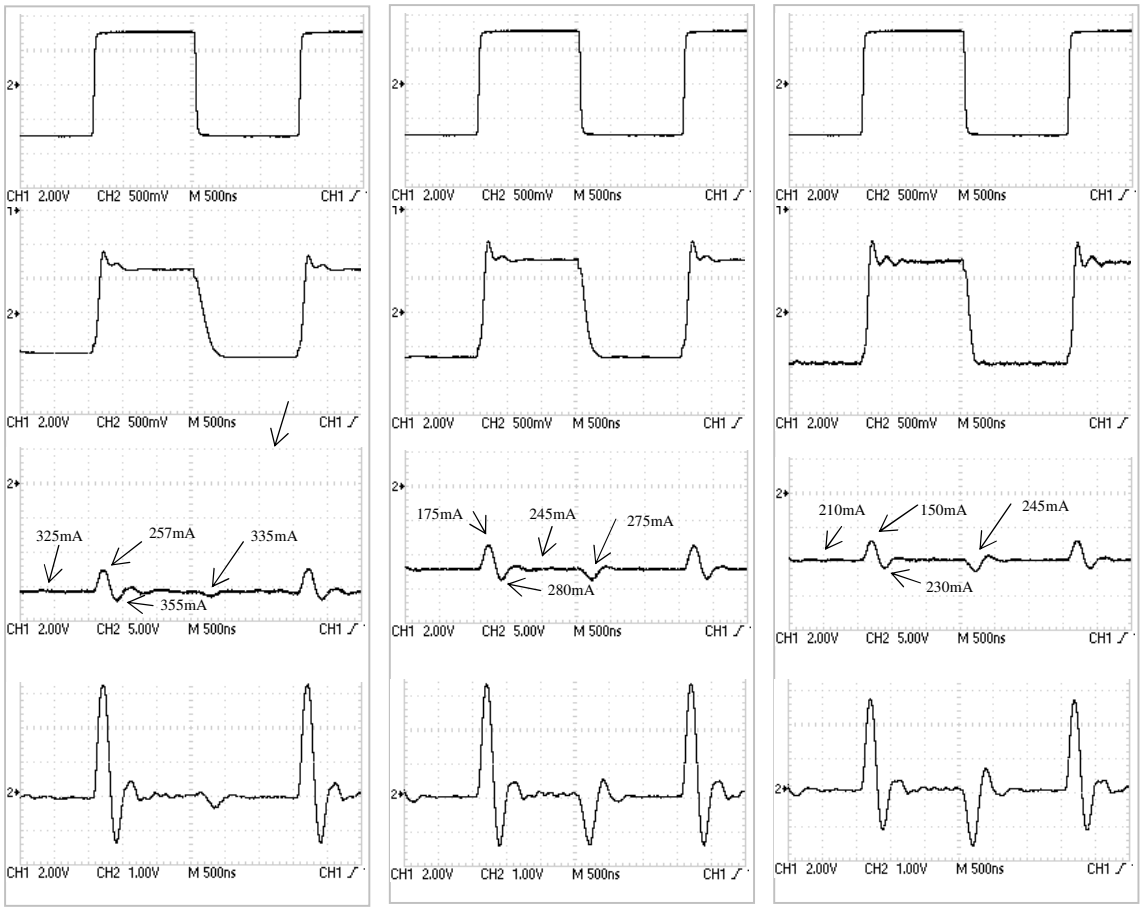

(a) 317 mA (b) 265 mA (c) 210 mA

Figure 5.9 Phase modulation with different anode currents,

Heater Power 33W, Injection Level -29dbc

A heater power of 33W is used again because the effect of 50 Hz and 100 Hz ripples becomes very large on the injection locked magnetron phase at higher heater power. It was not possible to obtain stable phase shift keying for anode currents below 200 mA. In

this region the pushing curve has a high gradient hence the frequency modulation for our level of anode current ripple (~l13%) was very large.

For low anode currents, the oscillation amplitude of the phase is somewhat higher when the injection phase is advanced compared with when the injection phase is retarded.

5.2 Phase Modulation with Un-matched Load

When the magnetron output is loaded and a certain amount of power is reflected back, it is observed that the transient behaviour of the magnetron RF output varies depending upon the phase angle of the reflected power. Some dependency of $d\theta/dt$ and $V_{RF}(t)$ on the load $(G+jB)$ is obvious from equations (5.4) and (5.7). Experimental results in this regard are shown in Figure 5.10 where 10% of the output power is reflected back into the magnetron with differing reflection angles set apart by 30^o steps (appropriate for encompassing the complete load dependent behaviour).

The top of each plot is labelled with reflection angles with respect to the magnetron's plane of reference (where the magnetron efficiency is at its maximum). As described in Chapter2, the magnetron is maximally efficient at the reflection angle about 135^o w.r.t. waveguide launcher. Hence $0.1\angle 0^o$ on top of Figure 5.10a represents 10% reflection from the stub tuner at 135^o w.r.t. to the waveguide launcher. The heater is kept at 44W and results were recorded for two different anode currents near to 340mA and 270mA. An injection level of -29 dBc has been used for all the plots in Figure 5.10. These plots

are 180^{o} phase shifted compared with the plots in the previous section in order to obtain a good coverage of the DC coupled anode current and the magnetron output phase at the same time.

The load effect on the phase modulation of the driven magnetron can be divided into three categories, in-phase reflection, quadrature phase reflection and out of phase reflection. When part of the magnetron output is reflected in phase or within +/- 30^{o} of this region, the peak-to-peak oscillation in the anode current is considerably less, about half as much, compared with the case when the load is matched. Also the overshoot in the magnetron output phase response is relatively small.

As the phase of the reflected signal becomes in quadrature with the magnetron plane of reference, the level of the anode current oscillation increases and keeps increasing until it reaches the out of phase reflection region, as shown in Figures 5.10c and 5.10d. A very interesting thing to notice in the phase quadrature zone is that the response tends to become quite symmetric for phase retard and phase advance when the anode current is low. The phase of the reflected wave has an effect on the net field in the anode cavities and hence on the relative movement of the charge spokes (w.r.t. the RF peak). It is also interesting that the oscillations in the anode current and more prominently in the magnetron phase take longer to decay for low anode currents. For higher anode currents i.e. when the spokes experience higher Retarding field (spoke near the middle of the cavity and α is minimal) the magnetron phase response still remains asymmetric for phase retard and advance just like when the load is matched.

The level of oscillation in the anode current is the highest when the reflected signal is nearly out of phase (close to 180^o w.r.t. magnetron's plane of reflection), a bit more than when the load is matched. For the reflection angles $0.1\angle 150^o$ and $0.1\angle -150^o$ Figures 5.10f and 5.10h show that we have very large oscillation of the anode current. This anode current oscillation becomes so large at the reflection angle $0.1\angle 180^o$ that the corresponding shift in the natural frequency of the magnetron is beyond the lock in range of the Injection level (-29dBc) and destabilises the Digital frequency control on the magnetron, hence the Injection + FLL system stops working altogether. This effect of extremely large overshoot in the anode current is more pronounced at lower anode currents where the pushing curves slope is greater. It is represented as 'No Result' in Figure 5.10g. Interestingly we do not see a large overshoot in the magnetron phase response in the region of anti-phase reflection (reflection angles $0.1\angle 150^o$ to $0.1\angle -150^o$), albeit large anode oscillations

From Figures 2.4 and 2.5 we see that the pushing curves have a significant frequency shift as the phase of reflected power is varied close to quadrature. This dependency could be relevant to explaining some aspects the oscillatory response.

$0.1\angle 0^{o}$ w.r.t.. magnetron plane of reference (135° w.r.t. Waveguide Launcher)

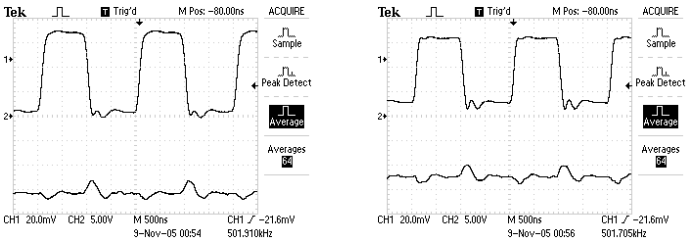

(a) 339mA 265mA

$0.1\angle 30^{o}$ w.r.t.. magnetron plane of reference (105° w.r.t. Waveguide Launcher)

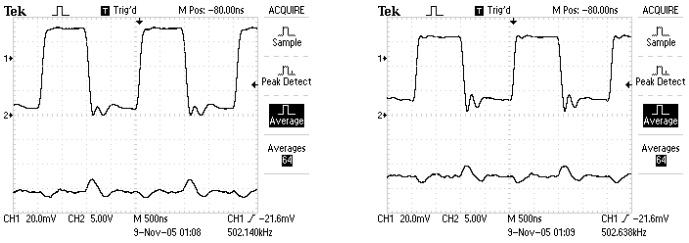

(b) 335mA 268mA

$0.1\angle 60^{o}$ w.r.t.. magnetron plane of reference (75° w.r.t. Waveguide Launcher)

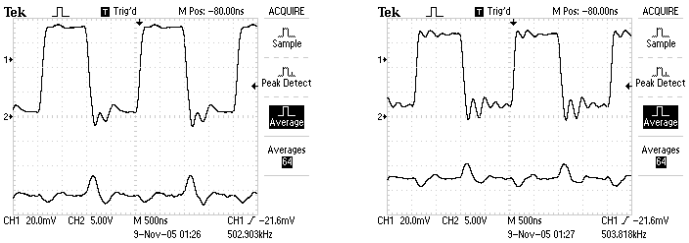

(c) 342mA 267mA

Figure 5.10 Effect of unmatched load on Phase modulation of the injection locked magnetron *(Continued)*

$0.1\angle 90^{o}$ w.r.t.. magnetron plane of reference (45^{o} w.r.t. Waveguide Launcher)

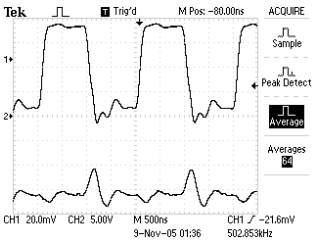

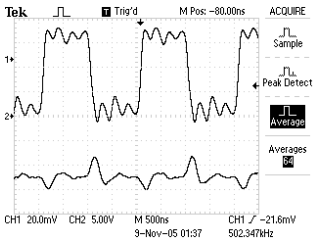

(d) 342mA 265mA

$0.1\angle 120^{o}$ w.r.t.. magnetron plane of reference (15^{o} w.r.t. Waveguide Launcher)

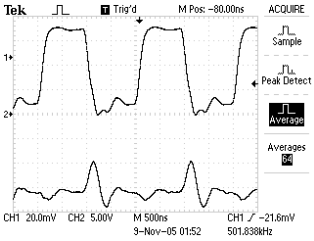

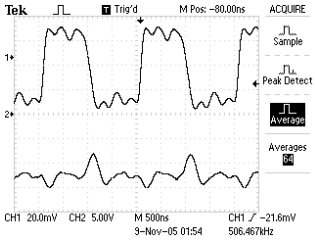

(e) 338mA 267mA

$0.1\angle 150^{o}$ w.r.t.. magnetron plane of reference (-15^{o} w.r.t. Waveguide Launcher)

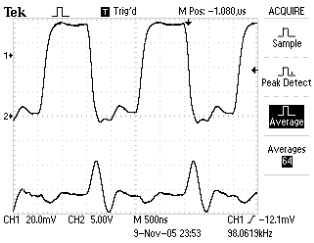

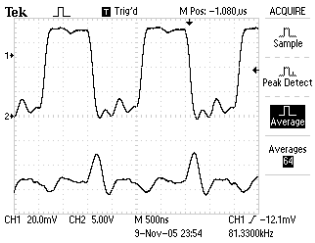

(f) 335mA 276mA

Figure 5.10 Effect of unmatched load on Phase modulation of the injection locked magnetron *(Continued)*

$0.1\angle 180^{o}$ w.r.t.. magnetron plane of reference (-45^{o} w.r.t. Waveguide Launcher)

No Result	No Result

(g) Injection+ FLL stops working at this load

$0.1\angle -150^{o}$ w.r.t.. magnetron plane of reference (-75^{o} w.r.t. Waveguide Launcher)

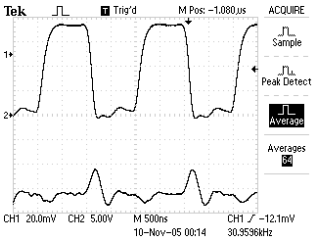

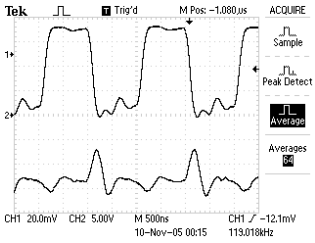

(h) 335mA 280mA

$0.1\angle -120^{o}$ w.r.t.. magnetron plane of reference (-105^{o} w.r.t. Waveguide Launcher)

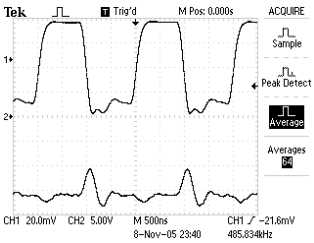

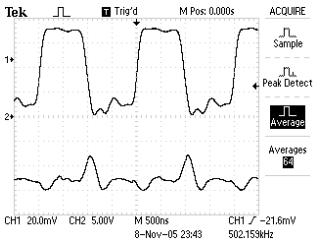

(i) 339mA 275mA

Figure 5.10 Effect of unmatched load on Phase modulation of the injection locked magnetron *(Continued)*

$0.1\angle -90^{o}$ w.r.t.. magnetron plane of reference (-135^{o} w.r.t. Waveguide Launcher)

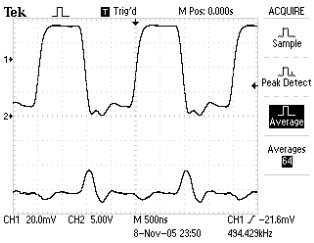

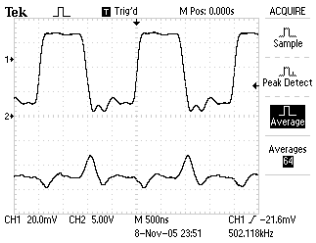

(j) 336mA 265mA

$0.1\angle -60^{o}$ w.r.t.. magnetron plane of reference (-165^{o} w.r.t. Waveguide Launcher)

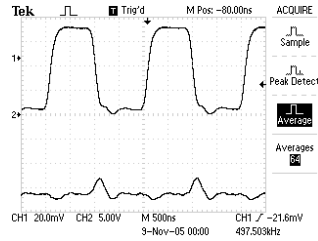

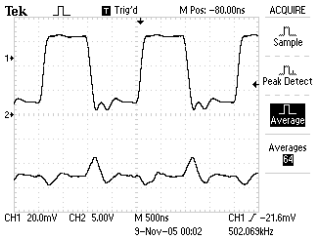

(k) 348mA 270mA

$0.1\angle -30^{o}$ w.r.t.. magnetron plane of reference (165^{o} w.r.t. Waveguide Launcher)

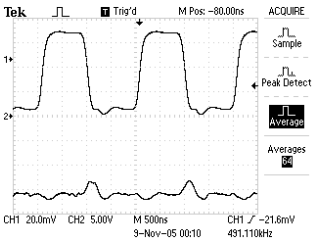

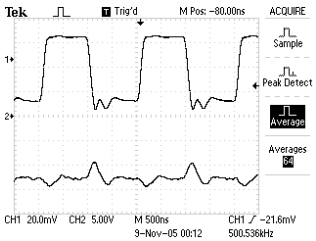

(m)342mA 270mA

Figure 5.10 Effect of unmatched load on Phase modulation of the injection locked magnetron

Digital frequency control on the magnetron through the power supply does not have an effect on the second order response of the driven magnetron phase as the loop bandwidth is very small (a few KHz) and it cannot contribute to the large sub-microsecond phase transitions. It only kicks in when the anode current (hence the natural frequency of the magnetron) shifts by a large amount and it is beyond the lock-in range of the injection signal power. This is explained earlier in this chapter for Figure 5.10g.

Results presented in this chapter add a new dimension towards understanding the behaviour of an injection locked magnetron. Although not fully understood and explained yet, they can be used to develop a complete model for the dynamic behaviour of the magnetron when driven by an external injection source. We have seen that the phase of the magnetron output follows the phase of the injection signal and the rate of change of phase mainly depends upon the heater power, injection level and the anode current. This feature can be used for many applications such as fixed power long distance data transmission and phase stable RF sources by correcting the effect of the power supply ripple and other inputs on the magnetron output phase via the injection phase. The latter is discussed in detail in the next chapter.

Chapter 6

USE OF DSP AND FAST FEEDBACK FOR ACCURATE PHASE CONTROL OF THE INJECTION LOCKED MAGNETRON

We have seen in Chapter 4 that the frequency feedback and injection locking can be used together, to ensure that the magnetron stays locked to the external reference source for its operating range. Residual phase jitter in the RF output due to the ripple on the power supply and heater source, can be reduced by a second feedback loop on the anode current.

Investigation of the transient response of the magnetron in Chapter 5 when the phase of the injection signal is stepped from a steady state value shows that the magnetron follows the phase of the injection signal at a rate determined by the heater power and the injection level. Even for very low injection levels, such as -30dBc or below, a rate of 180^{o}/ microsecond is achievable. Hence by controlling the phase of the injection signal it is possible to eliminate the phase jitter generated by the power supply and heater ripples. This type of control system to eliminate phase jitter is commonly employed with klystrons driving accelerator cavities. In this chapter it is shown that the same type of control system is applicable to a magnetron provided frequency is controlled by variation of its anode current. [42]

6.1 Injection phase control Setup

In Section 5.4 we describe how the magnetron can respond to a change of about 2π radian in 1 microsecond (0.36 degrees / ns) without an overshoot in its response. This technique can be used to correct influences which cause phase drifts. Using a digital phase detector, a proportional-integral controller and an electronic phase shifter, a phase locked loop can be implemented and the magnetron phase can be locked to the same external reference signal which provides the injection source. There are two different ways of implementing a proportional-integral controller; one is to use an RC network with an operational amplifier and the other is to use a digital signal processor along with analogue to digital and digital to analogue converters. Experimental setup with both methods is described below.

6.1.1 Injection phase control setup with an analogue controller

The experimental scheme with analogue controller is shown in Figure 6.1. Most of the scheme is the same as described in Chapter 4. It makes use of two digital phase detectors, ADF4113 to control the power supply input and an HMC439 fast 1.3 GHz phase detector to control the injection phase. The RF signal for feedback purpose is sampled from the loop coupler at the water load. This signal is split and taken to two separate digital phase

detectors. Each phase detector gives an error output ε that is proportional to phase difference between the reference and the RF input [42].

$$\varepsilon = \left(\omega_{mag} - \omega_{ref} \right) T + \phi_{mag} - \phi_{ref} \tag{6.1}$$

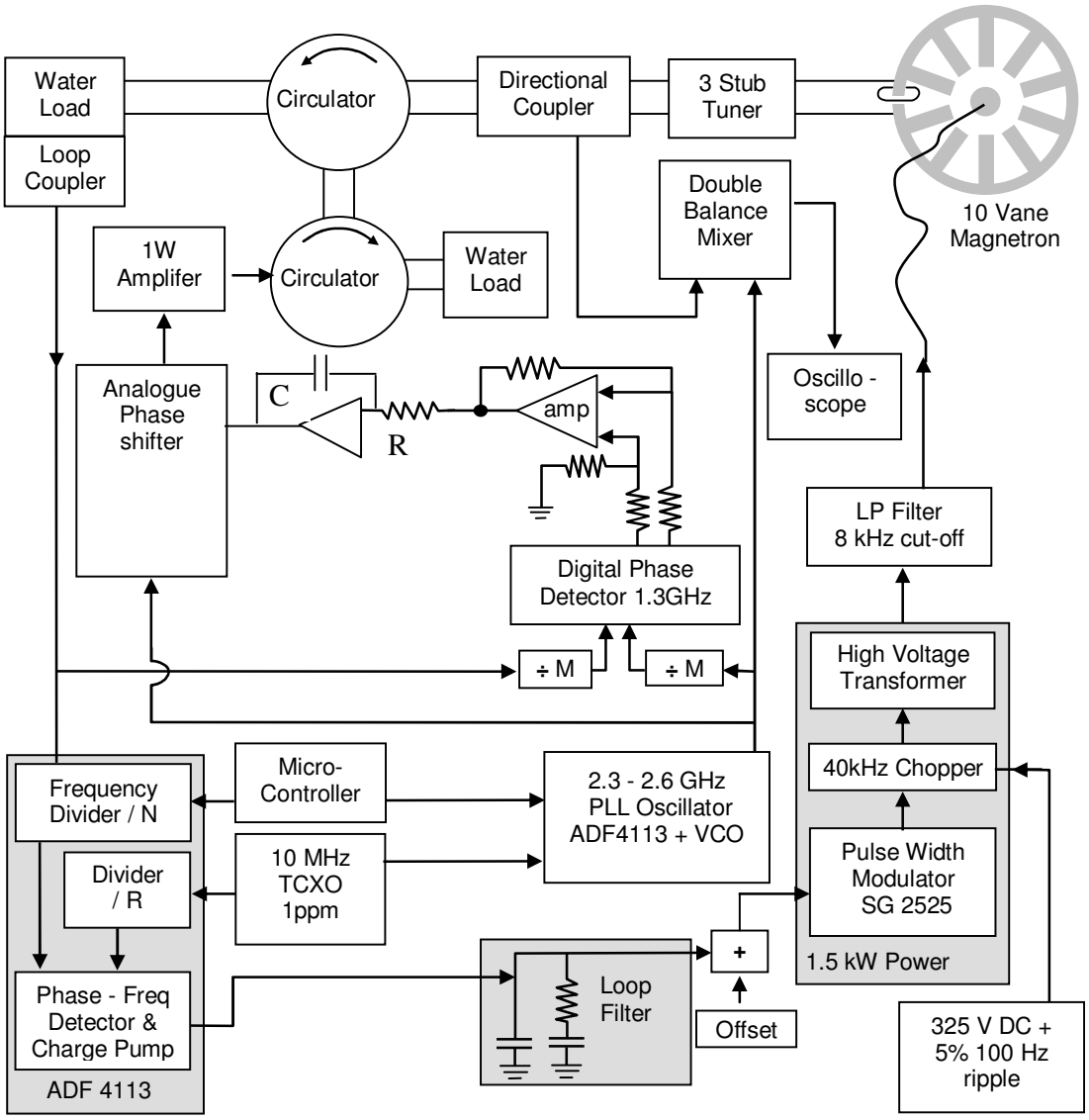

Figure 6.1 Setup for feedback control on injection with analogue controller

Where ω_{mag} and ω_{ref} are the angular frequencies of the magnetron and the reference, T is the time period over which the phase is measured. The time T is given by the division ratio N or M times the RF period. For the ADF4113 phase frequency detector N is large (12250) hence the detector is sensitive only to the average frequency difference. For the fast 1.3 GHz HMC439 phase detector $M = 2$ hence the output is half the instantaneous phase difference. The ADF4113 operates on the switched mode power supply control input through a passive loop filter in order to lock the magnetron frequency to an external 10 MHz reference. Whereas the HMC439 drives an electronic phase shifter through an active integrator and locks the magnetron phase to the 2.45 GHz source driven by same 10 MHz reference. The values of R and C were adjusted so that a loop bandwidth of about 50 kHz was achieved.

6.1.2 Injection Phase Control with a Digital controller

The scheme shown in Figure 6.1 works well in terms of controlling the phase, however for more sophisticated applications such as RF sources for accelerators, advanced feedback control is provided with digital signal processing. This allows the use of more complex control algorithms and feed forward techniques. This approach is commonly used for the control and compensation of micro-phonics and Lorentz forces in superconducting cavities [44].

Our digital control scheme is shown in Figure 6.3. It consists of a floating point DSP from Texas Instruments TMS320 C6713, one 80 MSPS 16 bit Analogue to Digital Converter (ADC) and two 30MSPS 16 bit Digital to Analogue Converter (DAC). The ADC samples the phase detector output and converts it into a parallel 16 bit digital signal.

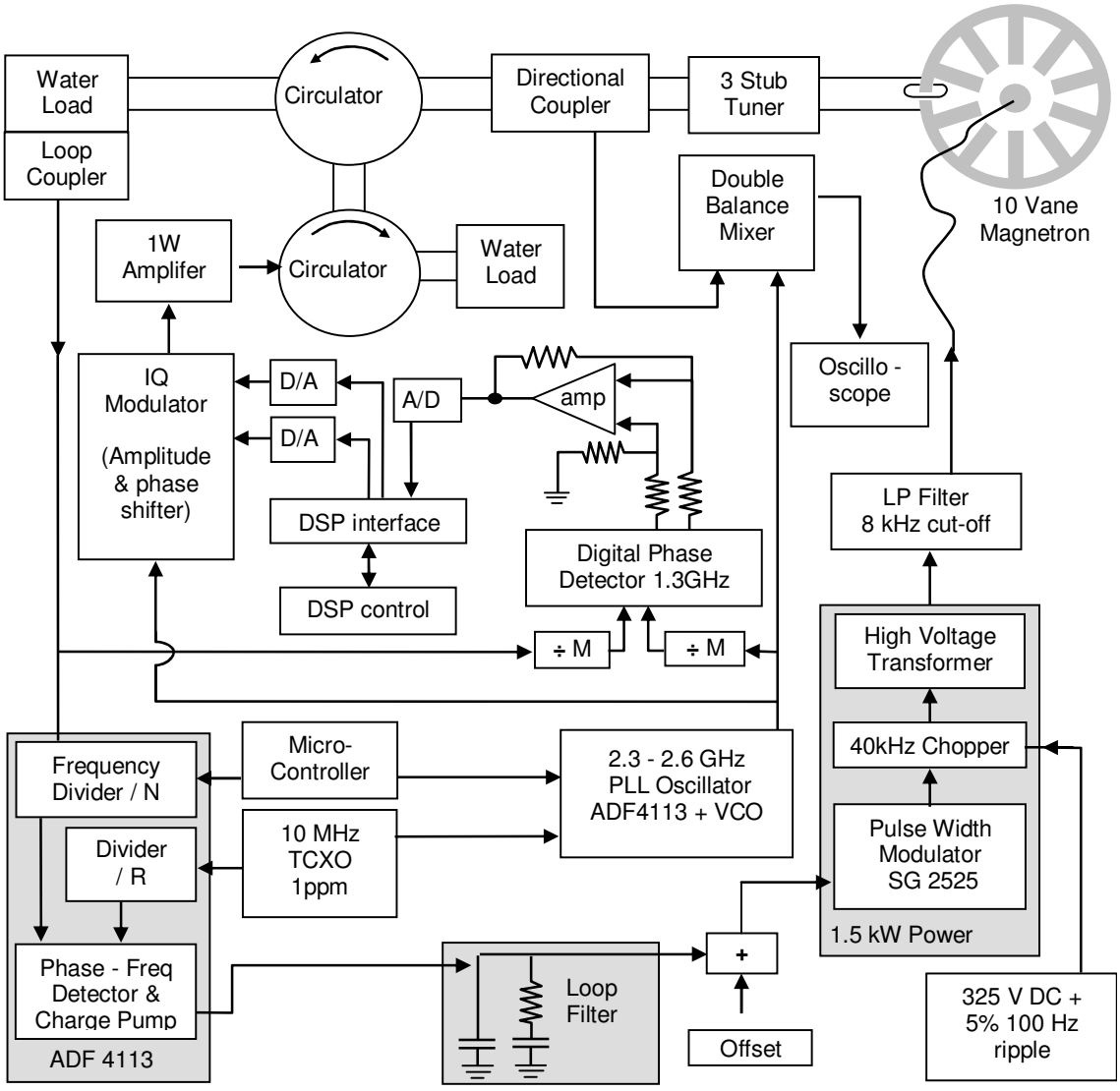

Figure 6.2. Experimental setup for feedback control on injection with Digital analogue controller

The DSP reads the ADC output through a 16 bit data bus and after applying a simple PI algorithm on the phase error, it generates a control signal. The control signal is converted into its in-phase (I) and quadrature (Q) components by the DSP and the resulting values are written to two DACs via same 16 bit data bus. These DACs drive I and Q inputs of a vector modulator, HMC497. The vector modulator advances or retards the injection phase in order to correct the phase error, keeping the amplitude at a set-point. The DSP takes about 1 micro-second to fetch data from ADC and apply a proportional-integral control algorithm on it. With the integral term $1/20^{th}$ of the proportional term, we get a loop bandwidth of about 50 kHz.

6.2 Phase control results

With the basic PI controller whether implemented in the form an RC integrator (Figure 6.1) or in the DSP software (Figure 6.2), the phase control performance for both techniques is the same as shown in Figure 6.3a and 6.3b. The traces in Figure 6.3a were obtained using averaging function on the oscilloscope to filter out the electromagnetic interference and phase jitter due to 43 kHz switching ripple on both anode current and the phase detector output. The top trace in Figure 6.3a is the anode current ripple (~13%), the middle trace is the phase detector output without fast feed back (± 14^{o} Peak-Peak), the lower trace is the phase detector output with fast feedback (± 0.6^{o} Peak-Peak). Figure 6.3b was obtained with the averaging function turned off. The top trace in Figure 6.3b is the phase detector output and lower trace is the anode current ripple. We see a +/-3 degrees peak-peak phase jitter due to the switching ripple. Because the loop bandwidth is about

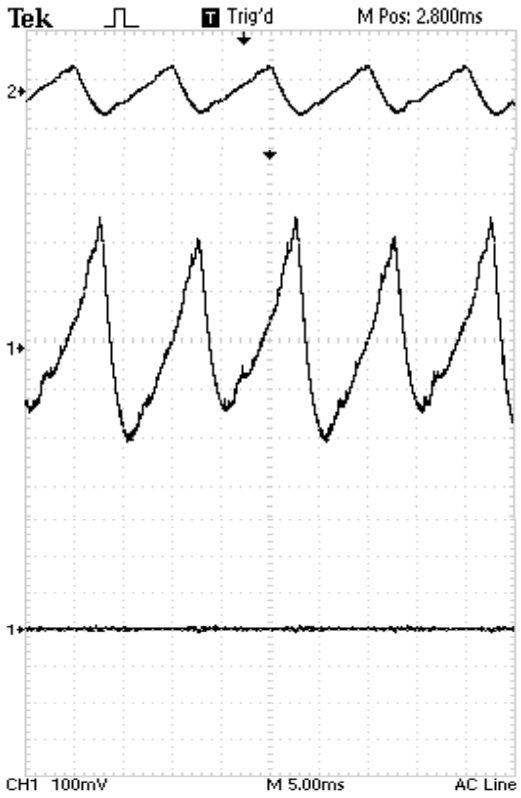

Anode Current Ripple

Phase detector (HMC439) output
Without Injection Phase Control
(± 14° Peak-Peak)

Scale: 6 degrees / Big Division

Phase detector (HMC439) output
With Injection Phase Control
(± 0.6° Peak-Peak)

Figure 6.3a Results with feedback control on the injection signal Phase with oscilloscope's averaging function

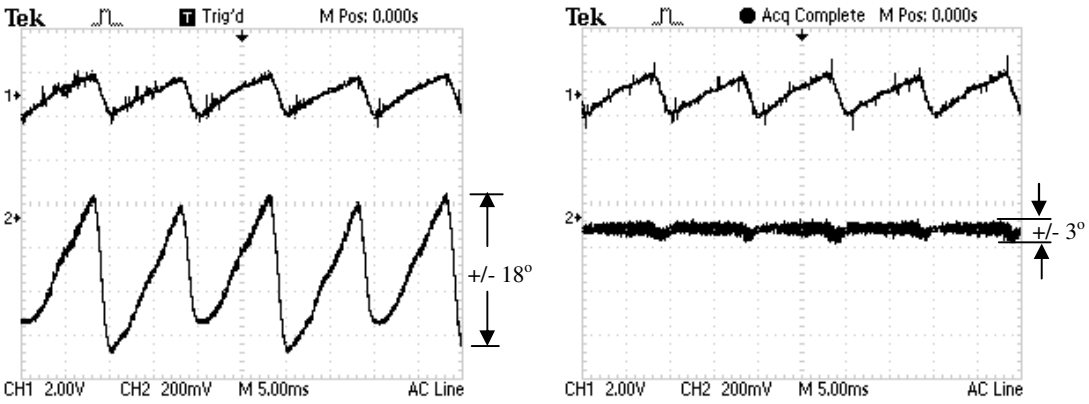

Without control on injection phase With control on injection phase

Figure 6.3b Phase detector output without oscilloscope's averaging function (CH1: Anode current ripple , CH2: Phase Detector output)

50 kHz, there is not enough gain at 43 kHz for the loop to correct the effect of this ripple. This ripple can be reduced, however, by adding more capacitance at the output of the high voltage power supply.

Precise phase control of the magnetron makes it suitable for many sophisticated applications. It can be used as an RF source for many types of particle accelerators. Phased arrays can be implemented for wireless power transmission. It can be used to send data for long distance communications using phase modulation techniques.

Many magnetrons driven by independent switched mode power supplies can be phase synchronized and scalable microwave power sources can be constructed for industrial heating and processing applications. Given that switched mode technology is now common place now a day, the cost factor for the implementation of the phase control techniques described in this thesis are minimal. All the components we have used come from the telecommunication and other commercial industries and are mass manufactured. Wherever high power CW microwave sources with excellent spectral performance are required, CW magnetrons phase stabilized by these techniques offer an unparalleled solution.

Conclusions

Our work has demonstrated that the magnetron's pushing response provides adequate opportunity for the frequency locking of a cooker magnetron over a range of anode currents. We have found that locking performance is highly dependent on heater power. An investigation of this dependency has been made and results used to perfect performance and data transmission by phase shift keying. The work has identified a region of heater power where frequency locking is very difficult. Dependency of pushing curves on heater power and magnetron output load has been investigated.

A novel circuit layout using a digital frequency synthesiser IC has been devised for controlling magnetron frequency by variation of the switched mode power supply pulse width. The thesis presents full details of the commercial power supply modifications that were required for frequency control. A high quality frequency lock to an external 10 MHz reference source has been demonstrated taking into account the loop bandwidth limitations due to switching frequency of the power supply and the high level of the switching frequency ripple.

As a consequence of our ability to control the natural frequency of the magnetron through its pushing curve and our new understanding of the relationship between heater power and frequency locking performance, we have been able to injection lock the magnetron with injection levels 43dB below the magnetron output power. This has been achieved in

the presence of power supply ripple, heater power ripple and thermal cycling of the anode; under these conditions the achievement is a world first.

The frequency locked magnetron's response with injection locking has been studied with different injection levels and heater powers. Frequency spectra and phase demodulated output for the magnetron RF output show a phase jitter of the order of 13^{o} peak to peak. A third feedback loop controlling the anode current has been implemented to demonstrate the reduction of this jitter by a factor of 10.

The response of the injection locked magnetron to a step change in the injection signal phase has been investigated with differing rates of change of the injection phase, heater power, injection level, anode current and load. The detailed set of results presented depicts a second order response of the magnetron phase when the injection signal is suddenly changed from its previous value, this is a new observation. (Injection locking is possible for all oscillators as a consequence of the pulling effect but normally gives a first order response.) Equations have been derived to show the dependency of injection locking on pushing as well as pulling. As yet we do not have a dynamic model for injection locking hence we only have a qualitative understanding of the second order response

Precise sub-degree phase control of the magnetron output has been achieved by fast control of the injection phase to correct unwanted phase shifts. This implementation is another world first.

Detailed observations of the magnetron RF amplitude have been presented along with frequency spectra throughout the thesis. The main focus of the research work, however, has been to achieve high quality phase and frequency control of the magnetron. To this end we have been extremely successful. Methods for simultaneous amplitude control were not pursued during the course of the research but will be important in the future.

This research work leads to the potential use of industrial CW magnetrons for applications where high power microwaves with excellent phase and frequency stability is desired. As a consequence of this work magnetrons could now prove to be suitable as RF sources for long pulse particle accelerators needing multiple high power RF amplifiers operating in phase synchronism. The work opens the possibility of developing scalable high power microwave supplies for industrial processing by combining power from a number of small, mass produced, low cost magnetrons. Most remarkably the work shows an opportunity of using CW magnetron for fixed power data transmission with high data rates using various forms of phase shift keying. Important applications would include those requiring, high power, with high efficiency and light weight.

Appendix I

THE MAGNETRON POWER SUPPLY AND OTHER WAVEGUIDE COMPONENTS

This Appendix gives a brief description of the power supply and other waveguide components used for the experimental work in this research.

AI.1 The Switched Mode power supply

The power supply used to drive the magnetron is SM445, made by Aalter Technologies Italy and supplied by Richardson Electronics UK [51]. A lot of modification work was done in the power supply to make it suitable for frequency feedback control. Many circuit boards inside the power supply were replaced with our own and some filter and control circuits were deployed outside the power supply. The block diagram of our modified power supply is shown in Figure AI.1.

This Switched Mode Power Supply employs Full Bridge Converter topology to convert DC voltage into AC. The DC voltage for the IGBT Bridge is obtained by direct full wave rectification of the mains. The full bridge converter has four IGBTs. These IGBTs are driven by a Pulse Width Modulator (PWM) whose pulse width is controlled by a reference voltage input. The PWM IC is isolated from the high voltage (325VDC) system through Opto-couplers. The output from Opto-couplers drives two IGBT/MOSFET driver ICs which further drive the IGBT Bridge. The output from the IGBT Bridge goes to the transformer primary through a series LC tank circuit which provides Zero Voltage Switching (ZVS) in order to minimize switching losses and

hence stress on IGBTs. The 325VDC, IGBT bridge and its drivers have their own common point which is isolated from ground because mains are directly rectified without a transformer. The secondary output of the transformer is full wave rectified and filtered to get about-8KV DC when there is no load. Under load conditions the power supply is capable of delivering a maximum of 500mA at about -4KV DC.

AI.1.1 Pulse Width Modulator

The pulse width modulator is the part of the power supply which generates pulses to drive the inverter (DC to AC converter) section. The width of the pulses decides the conduction period of the power device and hence the output voltage and current. [48] The PWM IC in the power supply is UC2525. This is a dual output PWM, which is the fundamental requirement for the Full-Bridge topology. The block diagram of the IC is shown in Figure AI.2. The IC has an on-chip RC oscillator whose frequency can be set by an external resistor and a capacitor C_T. The oscillator frequency is set to 43 kHz, a limitation posed by IGBTs rise and fall time.(A sync input to the oscillator can allow multiple units to be slaved or single unit to be synchronised to external system clock.) A single resistor between the C_T and the discharge terminal provides a wide range of dead time adjustment. It has a built in soft start circuitry which requires only an external timing capacitor. A shutdown terminal controls both the soft-start circuitry and the output stages, providing instantaneous turn off through the PWM latch with pulsed shutdown, as well as soft-start recycle with longer shutdown commands [50].

When a constant reference voltage is applied to the pin 9 of the IC, the comparator (essentially an op-amp) compares the triangular waveform from the oscillator with the reference input in order to generate constant pulse width, as shown in Figure AI.3.. Pin 9 can be connected to the output of an external error amplifier for current feedback control or voltage feedback control. The IC provides two output pulses as required for a full bridge converter driven by IGBT/MOSFET driver ICs. One output turns a pair of transistors ON while the second keeps the other two transistors OFF. The pulse width modulator is the heart of the power supply. Any small change in pulse width is directly translated into change in output voltage and current, depending upon the load conditions.

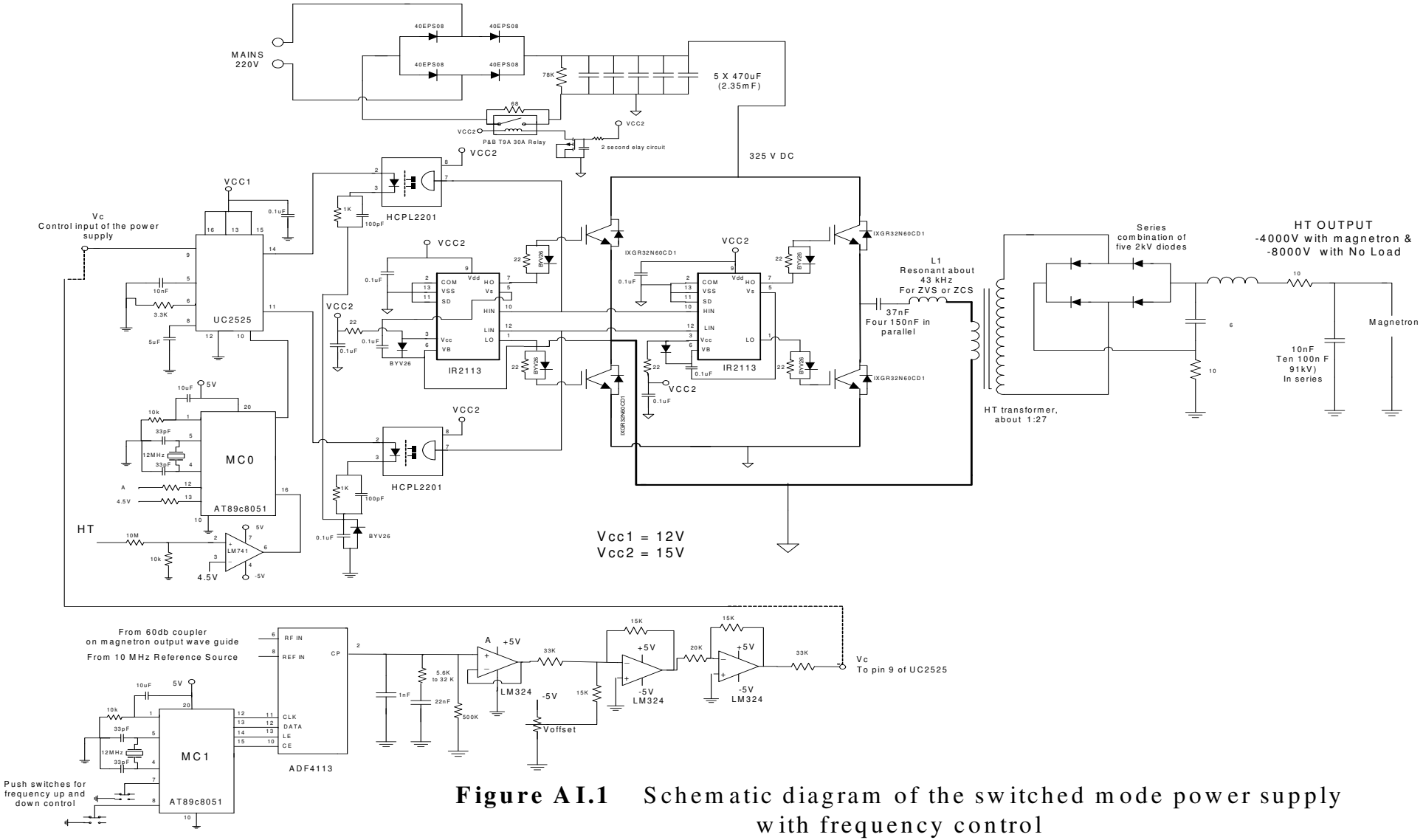

Figure AI.1 Schematic diagram of the switched mode power supply with frequency control

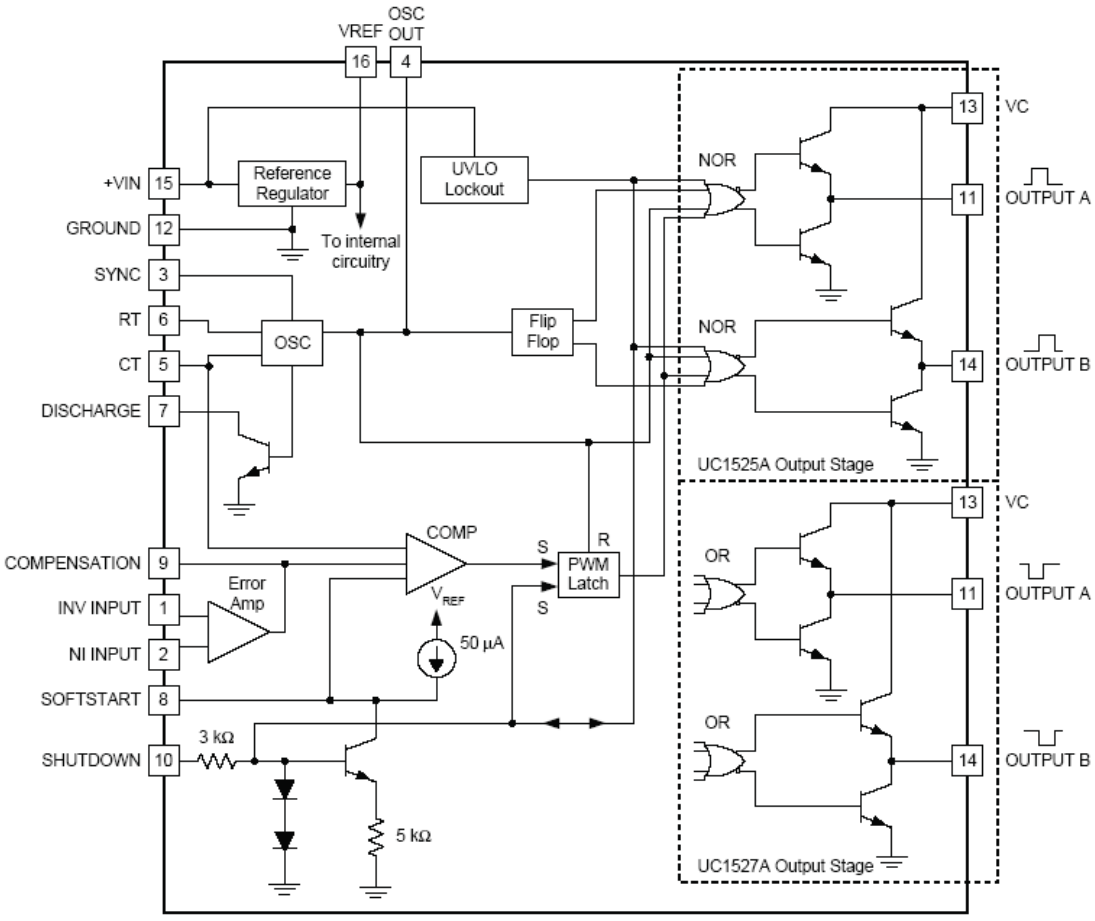

Figure AI.2 *Block* Diagram For UC2525.(Reprinted from Texas Instruments device datasheets [50])

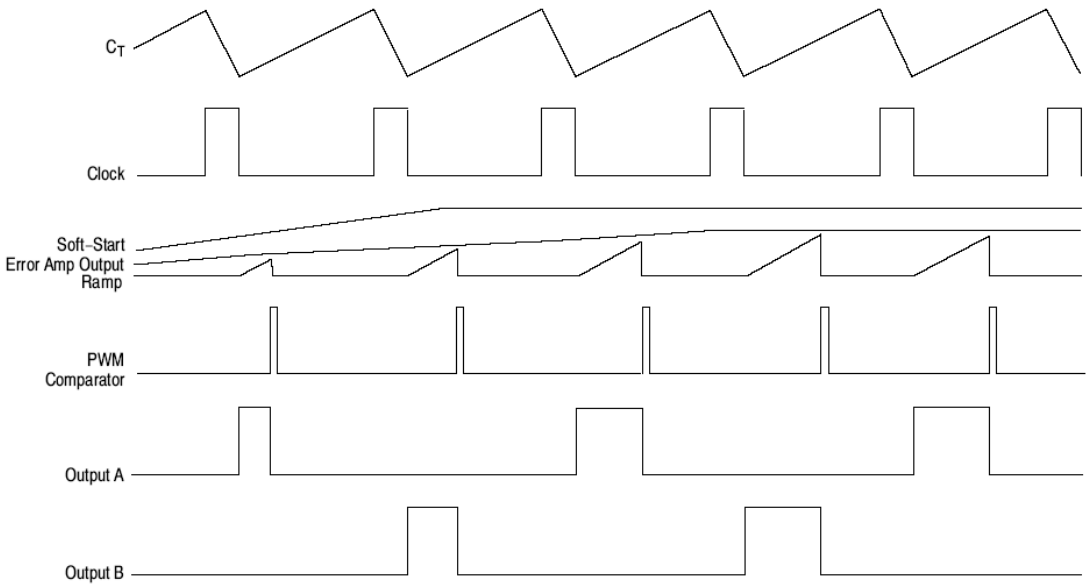

Figure AI.3 Process Waveform (Reprinted from Texas Instruments device datasheets [50])

AI.1.2 325VDC Source

The mains input is directly (without a transformer) full wave rectified to achieve 325V DC, as shown in Figure AI.1. The total capacitance inside the power supply for mains smoothing is 2.35 mF (obtained by putting five 4700 uF capacitors in parallel). At switch on the 2.35 mF capacitance would draw an unacceptably large amount of current hence a 68Ω resistance is placed in series with the capacitors to limit the current surge. Once the capacitors are charged after about 3 seconds this 68Ω resistance is shorted by a relay. A 78kΩ resistor is connected from rectified mains DC to a Common Point to bleed charge from the capacitors when power supply is shut down [51].

AI.1.3 Opto-Couplers

It is necessary to keep the PWM and rest of the control circuitry isolated from the power circuitry on primary side of HT transformer. That's why opto-couplers are used to deliver pulse width modulated signals to the MOSFET/IGBT drivers. Two HCPL2211 opto-couplers are used in the power supply. Figure AI.4 shows the block diagram for the IC.

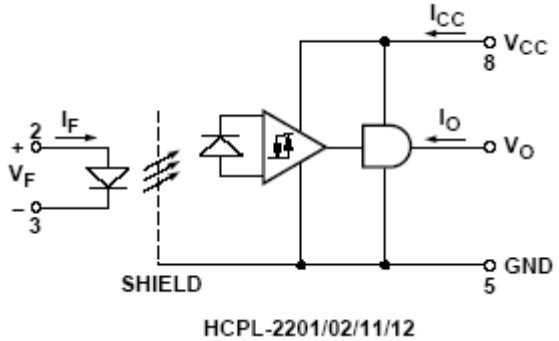

HCPL-2201/02/11/12

Figure AI.4 The opto-coupler used in the power supply (Reprinted From device datasheet [51])

AI.1.4 The Switching Section

The primary components in the switching section are four IGBTs in H Bridge configuration, a drive circuit and a switching loss minimizing circuit.

i) IGBTs & The H Bridge

The IGBT used for the full bridge converter is an IXGR 32N60CD1 from IXYS. The transistor is rated at 600V DC across the collector emitter junction with 45A. It can cope with 140W dissipation at room temperature. the total turn on time is in the region of 50ns and the turn off time is in the region of 200ns. [53]

As shown in Figure AI.1, two IGBTs have their collectors connected to 325V DC where the other two have their sources connected to common point. Output terminals are taken from the points where collector of one transistor meets the source of the other transistor. In H Bridge (Full Bridge) topology, during one pulse period, transistor 1 and 3 turn on, and 2 and 4 remain off so that the current flows through the primary of the transformer in one direction. In the next pulse period transistor 1 and 4 turn on while 3 and 2 stay off such that the current flows through the primary in the opposite direction.

As the transformers primary input is made resonant to minimize switching losses, we achieve a sinusoidal waveform at 43 kHz at the output of the transformer. The H Bridge in the power supply is made a series resonant converter in order to achieve soft

switching. Soft switching means that semiconductor devices are switched at zero crossing of their voltage or current waveforms. In order to achieve soft switching a series or parallel resonant LC tank circuit is used at primary side of the transformer. Soft switching can mitigate some of mechanism of switching loss and possibly reduce the generation of EMI.

ii) IGBT Driver IC

IGBT drivers are a necessary requirement for a full bridge converter. It is because two out of four IGBTs conduct at a time, and other two remain off. While an IGBT whose collector is connected to 325V DC is ON, the 325 DC voltage appears at the source terminal. As the control input is applied between gate and source, the output circuitry of the device providing with the modulated pulse to the IGBT gate should be able to float at high DC voltages (typically up to 600V DC). As can be seen in the functional block diagram of the IC, it takes two inputs, HIN and LIN referenced to a common point and provides with two outputs, HO for the IGBT whose source becomes live at 325VDC while conducting (IGBTs 1 & 4 in Figure AI.1) and LO for the IGBT whose source stays connected to the common point while conducting (IGBTs 2&3 in Figure AI.1).

The Driver IC used in the power supply is IR2110 from international Rectifiers. The IC's block diagram and a typical connection for a half bridge converter is shown in Figures 2.5 and 2.6 respectively.

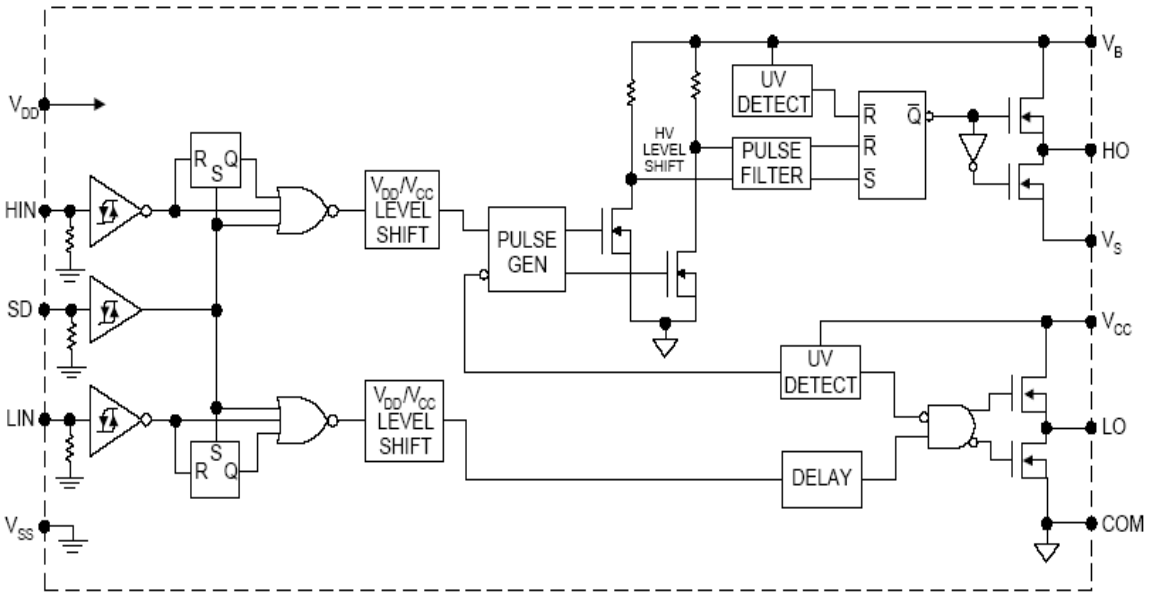

Figure AI.5 Block diagram of the IGBT driver IC IR2110

(Reprinted from International rectifier Datasheets[54])

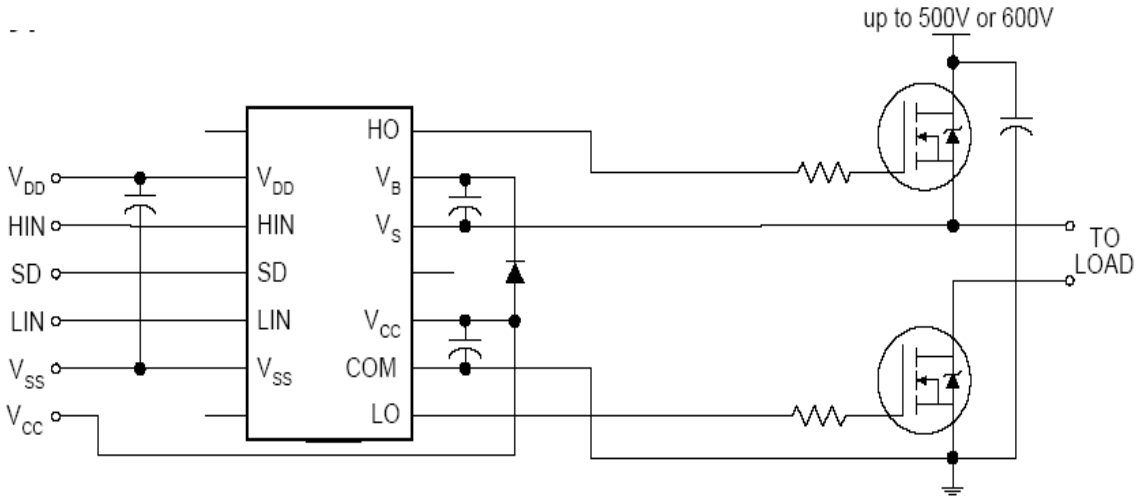

Figure AI.6 A typical Connection diagram between IR2110 and IGBTs

(Reprinted from International rectifier Datasheets [54])

iii) Switching Loss Minimizing Circuit

If an IGBT starts conducting (turns ON) while there is still voltage across it, or full DC voltage appears across it (turns OFF) while still current flowing through it, it would cause a large amount of loss in the device, reducing the efficiency and life of the device and its possible destruction. An LC tank circuit in series with H Bridge output is present inside the power supply, in order to achieve either ZCS or ZVS [49].

a) Zero Current Switching (ZCS)

This means that a transistor turn-off transition occurs at zero current. In order to achieve this the LC tank's resonant frequency is kept below the switching frequency so that input tank current leads the tank input voltage.

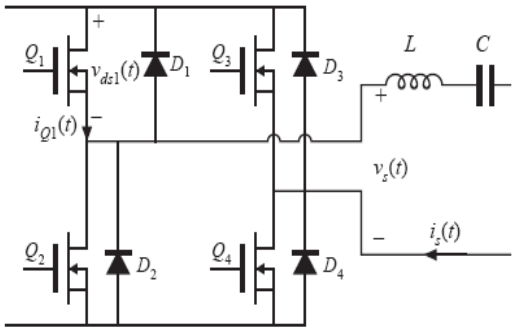

Figure AI.7 LC tank circuit between IGBT's and load(Reprinted from[49])

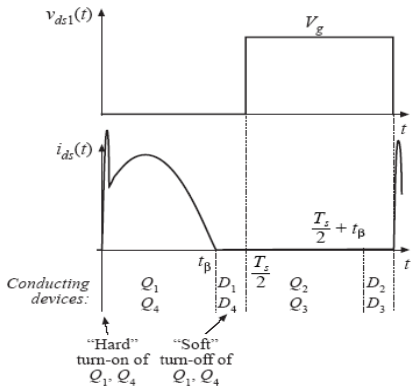

Figure AI.8 Zero Current Switching(Reprinted from[49])

As shown in Figure AI.8, Q1 and Q4 turn on while D2 and D3 are conducting. So turn-on transition is still a hard turn-on. However turn-off of Q1 and Q4 is soft. Similar is true for Q2 and Q3. Soft turn off eliminates switching loss caused by IGBT current tailing at turn-off and stray inductance of the device.

b) Zero Voltage Switching(ZVS)

This means that transistor turn-on transition occurs at zero voltage. In this case, the resonant frequency of the tank circuit is greater than the switching frequency. So input tank current lags the input tank voltage.

In Figure AI.10, When Q1 and Q4 turn off, D2 and D3 begin conducting in order to remove stored charge. Voltage across Q1 and Q4 increases to Vg. So transistor turn-off transition is hard.

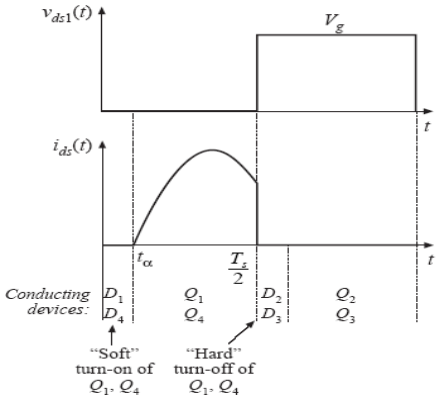

Figure AI.9 Zero Voltage Switching (Reprinted from[49])

However in practice the Vg takes some time to reach its maximum value, as shown in Figure AI.10. It means that loses at turn-off in ZVS can be reduced by increasing the commutation interval. This can be achieved by introducing extra capacitances across the switches (if their parasitic output capacitance is not enough to do the job).

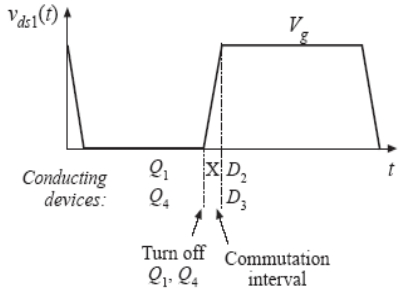

Figure AI.10 Avoiding Hard Turn Off in ZVS.(Reprinted from [49])

AI.1.5 HV OUTPUT SECTION

Secondary output of the transformer is full wave rectified and filtered to get a high DC voltage, as shown in Figure AI.1. A number of diodes are put in series so that it can cope with the high voltages across it. Then five of 22nF capacitors, each rated at 2KV DC, are put in series in order to make one 5nF capacitance. A big choke follows the capacitor in order to make the output smooth. Still there was a large amount of

43 kHz (switching frequency) so an additional 0.1uf capacitance is put across the output after the choke L2 in Figure AI.1, by putting ten of 1uF capacitors, each rated at 1KVdc, in series. This whole setup makes a π filter, providing us with a satisfactory 43 kHz ripple level.

The open circuit output voltage can be calculated using the formula,

$$V_o = V_{in}\left(\frac{N2}{N1}\right)\left(\frac{t1}{T}\right)$$

Where

V_o = Output voltage,

V_{in} = 325V DC,

t1 = ON duration of the pulse,

T = Time period of switching frequency,

t1/T is the duty cycle of the pulse,

N2/N1 is the transformer winding ratio.

The duty cycle of this converter may theoretically increase to 100%. In practice this is not possible because the serial connected transistors *IGBT 1 and IGBT 2* in Figure AI.1 have to be switched with a time difference in between, to avoid a short circuit of the input supply.

AI.2 The magnetron and other waveguide equipment

A brief description of the magnetron and other waveguide components connected to its output is as follows:

i) The Magnetron

Magnetron used for the research work presented in this report is 2M137 manufactured by Panasonic, normally used in commercial microwave ovens. General specifications of the magnetron are:

Output Power: 1.2KW

Frequency: 2.45GHz

Maximum Anode Current: 450mA

Heater Voltage: 4.4V

Further details of the magnetron can be found in Appendix VI.

ii) The Magnetron Head

Magnetron head (TMA 1.2V01 from Aalter Technologies) consists of forced air cooling system for the magnetron, step-down transformer for the cathode filament heater (which can provide up to 10kV isolation between cathode and mains), a temperature sensor, an arc detector and a waveguide launcher for the magnetron.

iii) The Three-Stub Tuner

3-stub tuner (WR340TUNERA-IB from Richardson Electronics) consists of three adjustable stubs with position markers, and can deliver reflection coefficient from 0 to 0.8 and reflection angles within 180^{o}. It has a VSWR of 3:1. The 3 stub tuner is rated at 6 KW as maximum power.

iv) The Directional Coupler

60 dB directional loop coupler (WR340DDCN from Richardson Electronics) was used to measure both forward and reflected power accurately. Also it provides magnetron output signal for frequency feedback control. Its directivity is greater than 20db. The loop coupler is rated at 3KW as maximum power.

v) The Circulator

The circulators/Isolators (2722-162-10471 from Richardson Electronics) were used to isolate the low power injection source from the magnetron high power output. It can tolerate up to 3KW forward and reflected power and offers reverse isolation of the order of 20 dB. The phase shift through the circulator is 0^o (the input is in line with the output).

vi) The Load

The load used for the research work is a 3kW water load which came attached to the circulator. This load is equipped with a 65 dB loop coupler.

Apendix II

DIGITAL PHASE LOCKED LOOP IMPLEMENTATION FOR THE MAGNETRON AND LOOP FILTER DESIGN

The digital frequency synthesizer IC ADF4117 based PLL circuit used for the magnetron frequency control is shown in Figure AII.1.

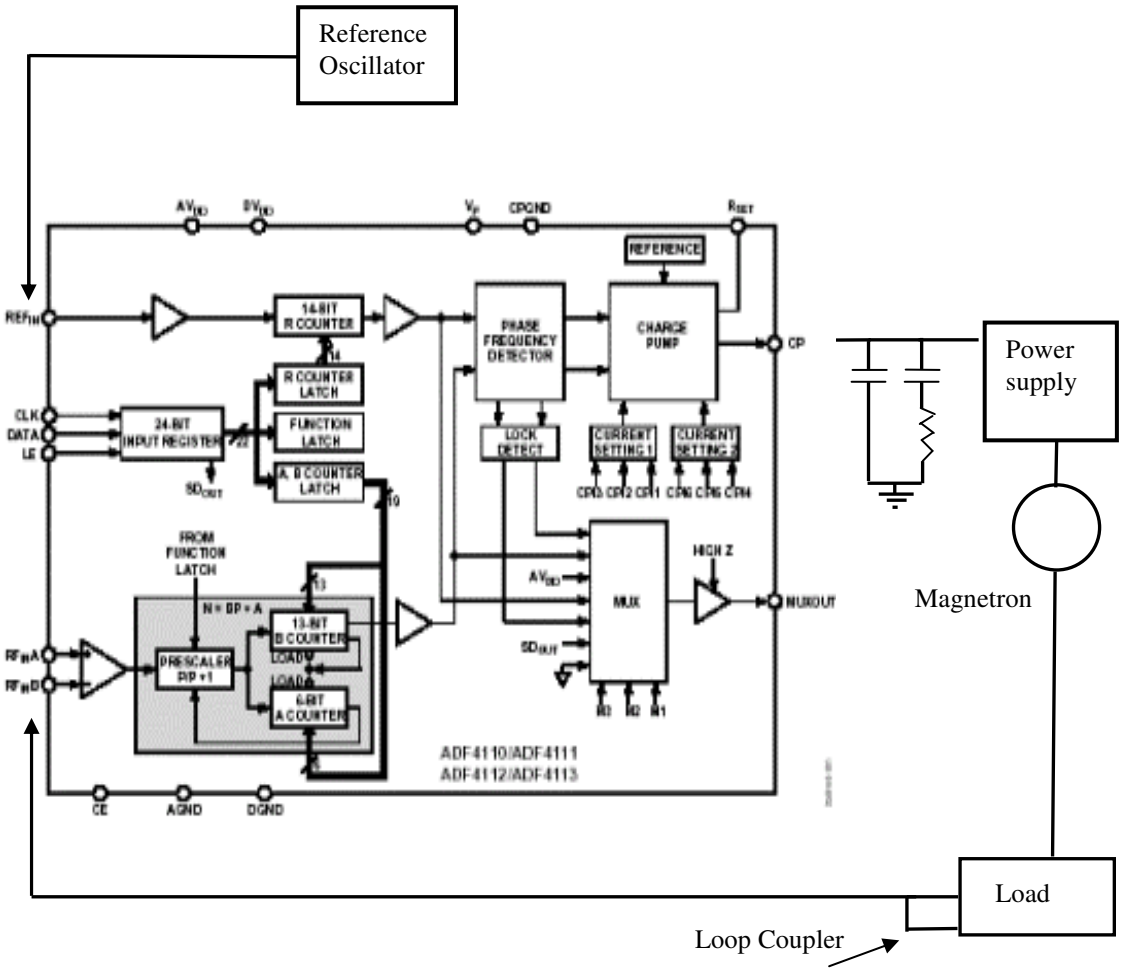

Figure AII.1 Block Diagram of Magnetron frequency feedback Control (DPLL) setup with ADF4113 (ADF4113 Internal Diagram from Analog Devices Data sheets[46]).

The ADF4113 requires some internal registers to be set in order to program division ratios for RF and reference inputs and the charge pump current output. It has a 3 pin

Serial Peripheral Interface (SPI) in order to program these registers. Serial data to set these parameters was provided by an 89C4051 microcontroller.

The main design parameters for the PLL are loop natural frequency, ω_n and the damping factor, ζ. The loop natural frequency is the frequency at which the loop would oscillate when disturbed from equilibrium. The loop natural frequency determines the response time of the loop. The damping factor is the rate at which the natural oscillation dies away while the loop is achieving a lock. Increasing the damping ratio improves the stability of the loop.

Related parameters when the loop is open are the open loop bandwidth and the phase margin. The open loop bandwidth, ω_p is defined as the frequency at which open loop gain becomes equal to 1 (0dB). The phase margin, ϕ_p is defined as the difference between 180^o and the phase of the open loop transfer function at the frequency ω_p.

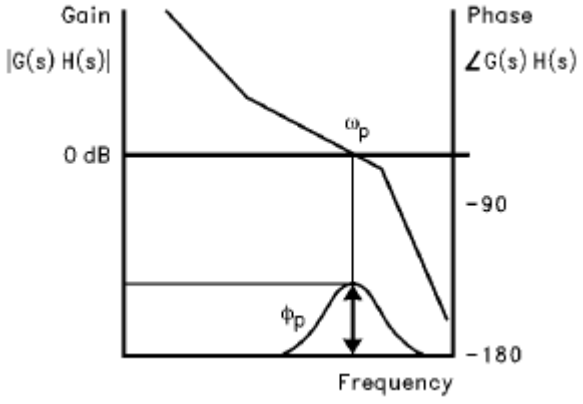

Figure AII.2 Open Loop Bandwidth and Phase Margin for a PLL system

(Reprinted from National semi conductor Application Note, 1001 [45])

After selecting appropriate VCO and PFD, next step is the loop filter design. Loop filter helps in controlling the critical loop parameters, natural frequency and damping factor.

AII.1 Detailed Loop Filter design [55],[56],[57],[58]

Considering design procedures from control theory, the loop filter can be designed using two methods; the Closed Loop method and the Open Loop method. The closed loop method uses loop's natural frequency and damping factor to obtain loop filter values, where as Open Loop method takes advantage of Open Loop bandwidth and Phase Margin as design parameters to do the same job.

As a charge pump PFD is being used, the filter which gives the best performance (low phase jitter and better control over loop parameters such as bandwidth, step response while keeping the loop stable) is a second order filter shown in Figure AII.3

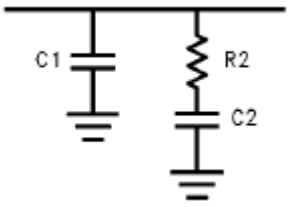

Figure AII.3 Second Order loop filter for a Charge Pump PFD(Reprinted from AN1001[45])

C1(with a minimal series resistance) is required to convert current pulses from the charge pump in to voltage, where as R2 and C2 form a lead-lag low pass network in order to provide with required bandwidth and phase margin.

Note: For design simplicity, 'Power supply + Magnetron' is considered as an ideal VCO, and gain and phase response of the power supply to its input frequencies is ignored. However their effect is discussed in detail in Chapter 4.

AII.1.1 Closed Loop method

A block diagram for the control loop has been given in Figure 3.1. Take the loop filter to be first order as a shown in Figure AII.4,

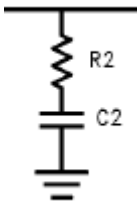

Figure AII.4 First order loop Filter

the transfer function for the filter is given by

$$Z(s) = R2 + \frac{1}{C2 \cdot s} = \frac{R2 \cdot C2 \cdot s + 1}{C2 \cdot s} \qquad \text{(AII.1)}$$

hence with reference to Figure 3.1 we have that

$$\text{Forward loop gain= } G(s) = K_p \cdot \frac{R2 \cdot C2 \cdot s + 1}{C2 \cdot s} \cdot \frac{K_v}{s} \qquad \text{(AII.2)}$$

$$\text{Reverse Loop Gain = } H(s) = \frac{1}{N} \qquad \text{(AII.3)}$$

$$\text{Closed Loop gain = } \frac{G(s)}{1 + G(s) \cdot H(s)} = \frac{K_p \cdot K_v (1 + R2 \cdot C2 \cdot s)/C2}{s^2 + \frac{K_p \cdot K_v \cdot R2}{N} \cdot s + \frac{K_p \cdot K_v}{N \cdot C2}} \qquad \text{(AII.4)}$$

The response to determined from the position of the poles in the denominator of the transfer function hence setting denominator in equation (AII.4) equal to zero

$$s^2 + \frac{K_p \cdot K_v \cdot R2}{N} \cdot s + \frac{K_p \cdot K_v}{N \cdot C2} = 0 \qquad \text{(AII.5)}$$

and comparing it with $s^2 + 2 \cdot \omega_n \cdot \zeta \cdot s + \omega_n{}^2 = 0$ gives us

$$2 \cdot \omega_n \cdot \zeta = \frac{K_p \cdot K_v \cdot R2}{N} \qquad \text{(AII.6)}$$

$$\omega_n{}^2 = \frac{K_p \cdot K_v}{N \cdot C2} \qquad \text{(AII.7)}$$

Criteria for choosing ω_n and ζ will be given later however once chosen values for the resistance and capacitance in the loop filter can be determined.

From Equations AII.6 and AII.7, we obtain values of R2 and C2 as

$$C2 = \frac{K_p \cdot K_v}{N \cdot \omega_n{}^2} \qquad \text{(AII.8)}$$

$$R2 = 2 \cdot \zeta \cdot \sqrt{\frac{N}{K_p \cdot K_v \cdot C2}} \qquad \text{(AII.9)}$$

The 3dB bandwidth of the closed loop transfer function given by [55] is

$$\omega_{3db} = \omega_n \sqrt{1 + 2\zeta^2 + \sqrt{(1 + 2\zeta^2)^2 + 1}} \quad \text{rad/sec} \qquad \text{(AII.10)}$$

Although this is termed Loop Bandwidth, there is a more useful measure of bandwidth called equivalent noise bandwidth B_n. The equivalent noise bandwidth of a linear system with transfer function H(s) is the bandwidth of a fictitious rectangular low pass filter with the same area as $|H(s)|^2$. For a 'proportional integral loop filter, it is given by [55]

$$B_n = \frac{\omega_n}{2}\left(\zeta + \frac{1}{4\zeta}\right) \quad \text{Hz} \qquad \text{(AII.11)}$$

We can see that loop bandwidth is a non linear function of damping factor. B_n is 1.6 times the 3db bandwidth.

If loop's natural frequency and damping factor is specified, then R2 and C2 can be calculated. In an ordinary Digital PLL, the loop bandwidth can be selected up to 1/5 times the PFD frequency (200 kHz for our implementation). However in our case, another constraint is introduced by the switching frequency of the power supply. No frequency components higher than 1/10 times the switching frequency should appear on the control input of the power supply. So our 3db loop bandwidth should be up to 1/10 times the switching frequency of the power supply, which is 43 kHz in our case, so the loop bandwidth should be up to about 4 kHz. As far as damping factor is concerned, it is normally chosen between 0.5 and 2, however ξ=0.707 is the most popular choice as it gives critically damped response. For ξ=0.707, equations AII.10 and AII.11 show that the loop natural frequency is about half the 3db loop bandwidth and 1/3.33 times the 'equivalent noise loop bandwidth'.

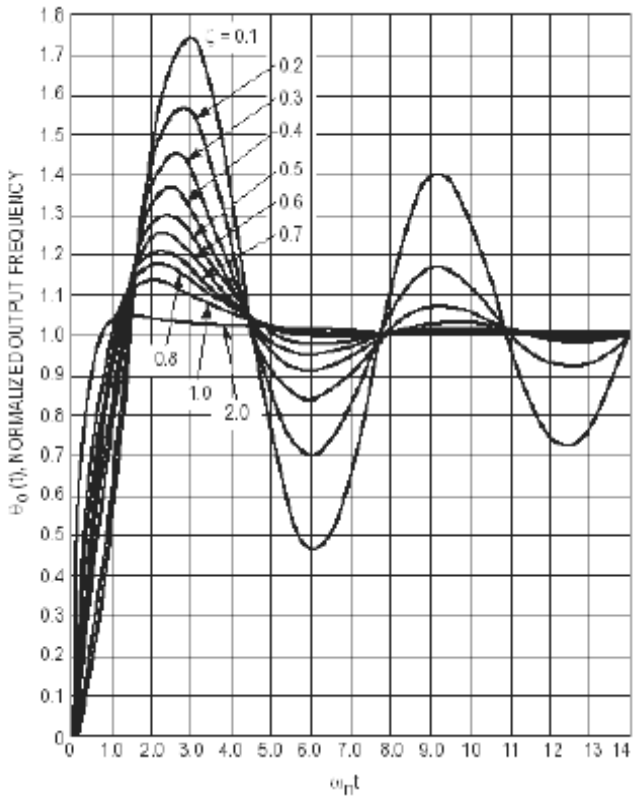

Figure AII.5 Type 2 second order step response for various damping factors

(Reprinted from Motorola AN-535 [59])

Now we can design the loop filter for a centre frequency of 2.45 GHz and frequency steps of 200 kHz.using following parameters:

VCO sensitivity = K_v = 14 MHz/V

PFD Constant = K_p = 2.5 mA

RF Division Ratio = N = $\frac{2.45\text{GHz}}{200\text{KHz}}$ = 12250

Damping factor = 0.707

3db Loop Bandwidth = 3.7 kHz (A value chosen to maximize the loop bandwidth)

From (AII.10) and (AII.11) we get

Loop natural frequency = f_n = 1.8 kHz ,

Equivalent noise bandwidth = B_n = 6 kHz

From (AII.8) and AII.9) we get

C2 = 22.2 nF

R2 = 5.64 KΩ

The phase detector's current source outputs pump electronic charge into the loop filter which then converts the charge into VCO's control voltage. The shunt capacitor C1 (as shown in Figure AII.3) is recommended to avoid discrete voltage steps at the control port of the VCO due to instantaneous changes in the charge pump current output. This is because in absence of C1, voltage across C2 cannot be changed instantly due to initial voltage drop across R2. In addition C1 makes the filter a second order low pass filter and the over all loop becomes of 3rd order. C1 adds a third pole of

finite frequency which is given by $\omega_{C1} = \frac{C1 + C2}{R2C2C1}$. The added pole reduces the phase margin. In fact now when the loop gain is increased, phase margin is reduced. So we must be careful that the pole frequency added by C1 is much higher than the natural frequency of the loop.

$$\omega_{C1} >> 10\omega_n \tag{AII.12}$$

For any C1/C2 ratio, it can be shown that the maximum phase margin is [25]

$$PM_{max} = 2\tan^{-1}\left(\sqrt{\frac{C2}{C1} + 1}\right) - \frac{\pi}{2} \tag{AII.13}$$

And a new cross over frequency (open loop gain =1) can be estimated as

$$\omega_p = \sqrt{\frac{C2/C1 + 1}{C2R2}} \tag{AII.14}$$

The phase margin equation leads to a guideline that C2>20C1 in order to obtain a minimum of 65 degree phase margin (which corresponds to ζ=0.707).

$$C1 \le \frac{C2}{20} \tag{AII.15}$$

So for a loop bandwidth (B_n) of about 6 kHz and damping factor (ζ) of 0.707, 2nd order loop filter component values would be;

R2 = 5.64 KΩ,

C2 = 22nF,

C1 = 1nF.

AII.1.2 Open Loop method

Considering the loop filter shown in Figure AII.3 again; the impedance of the second order loop filter is given by;

$$Z(s) = \frac{s(C2 \cdot R2) + 1}{s^2 (C1 \cdot R2) + sC1 + sC2} \quad \text{(AII.16)}$$

We can define the time constants which determine the pole and zero frequencies of the transfer function by letting

$$T1 = R2 \cdot \frac{C1 \cdot C2}{C1 + C2} \quad \text{(AII.17)}$$

$$T2 = R2 \cdot C2 \quad \text{(AII.18)}$$

Hence

$$Z(s) = \frac{(1 + sT2)}{C1 \cdot s \cdot (1 + sT1)} \cdot \frac{T1}{T2} \quad \text{(AII.19)}$$

Thus 3rd order PLL open loop gain can be calculated as

$$\text{Open Loop Gain} = G(s) \cdot H(s) = \frac{K_p \cdot K_v}{s^2 \cdot C1 \cdot N} \cdot \frac{(1 + sT2)}{(1 + sT1)} \cdot \frac{T1}{T2} \quad \text{(AII.20)}$$

Replacing s with jω

$$\text{Open Loop gain} = -\frac{K_p \cdot K_v}{\omega^2 \cdot C1 \cdot N} \cdot \frac{(1 + j\omega \cdot T2)}{(1 + j\omega \cdot T1)} \cdot \frac{T1}{T2} \quad \text{(AII.21)}$$

From open loop gain, the phase of open loop transfer function can be obtained as

$$\varphi(\omega) = \tan^{-1}(\omega \cdot T2) - \tan^{-1}(\omega \cdot T1) \quad \text{(AII.22)}$$

Phase Margin is given by the difference between 180 and the phase of the open loop transfer function at the frequency $\omega_{p,}$ as shown in Figure AII.2. So

$$\varphi_p(\omega) = \varphi(\omega) + 180 \quad \text{(AII.23)}$$

By setting the derivative of the phase margin equal to zero, the frequency point corresponding to phase inflection point (ωp), can be found in terms of filter time constants.

$$\frac{d\varphi_p}{d\omega} = \frac{T2}{1+(\omega \cdot T2)^2} - \frac{T1}{1+(\omega \cdot T2)^2} = 0 \qquad \text{(AII.24)}$$

Replacing ω with ω_p and solving the equation for ω_p, we get

$$\omega_p = \frac{1}{\sqrt{T2 \cdot T1}} \qquad \text{(AII.25)}$$

To ensure the loop stability, we want the phase margin to be the maximum, when magnitude of the open loop gain equals 1. So from Equation AII.21, replacing ω with ω_p and making open loop gain equal to 1, we get

$$\frac{K_p \cdot K_v}{\omega_p{}^2 \cdot C1 \cdot N} \cdot \left| \frac{(1+j\omega_p \cdot T2)}{(1+j\omega_p \cdot T1)} \right| \cdot \frac{T1}{T2} = 1 \qquad \text{(AII.26)}$$

$$\Rightarrow C1 = \frac{K_p \cdot K_v}{\omega_p{}^2 \cdot N} \cdot \left| \frac{(1+j\omega_p \cdot T2)}{(1+j\omega_p \cdot T1)} \right| \cdot \frac{T1}{T2} \qquad \text{(AII.27)}$$

Therefore, if loop bandwidth, ω_p, and the phase margin, φ_p, are specified, equations 4.27 and 4.30 allow us to calculate two time constants, T1 and T2.

$$T2 = \frac{1}{\omega_p \cdot T1} \qquad \text{(AII.28)}$$

$$T1 = \frac{\sec\varphi_p - \tan\varphi_p}{\omega_p} \qquad \text{(AII.29)}$$

Once time constants are calculated from loop bandwidth and phase margin, then values of C1, R2 and C2 are obtained in the equations AII.30 to AII.31.

$$C1 = \frac{K_p \cdot K_v}{\omega_p{}^2 \cdot N} \sqrt{\frac{1+(\omega_p \cdot T2)^2}{1+(\omega_p \cdot T1)^2}} \cdot \frac{T1}{T2} \qquad \text{(AII.30)}$$

$$C2 = C1 \cdot \left(\frac{T2}{T1} - 1 \right) \qquad \text{(AII.31)}$$

$$R2 = \frac{T2}{C2} \qquad \text{(AII.32)}$$

In order to obtain the component values for the loop filter, we need to specify phase margin and open loop bandwidth. In order to achieve 0.707 damping factor, phase margin should be 65 degrees (see Figure AII.6) [57]

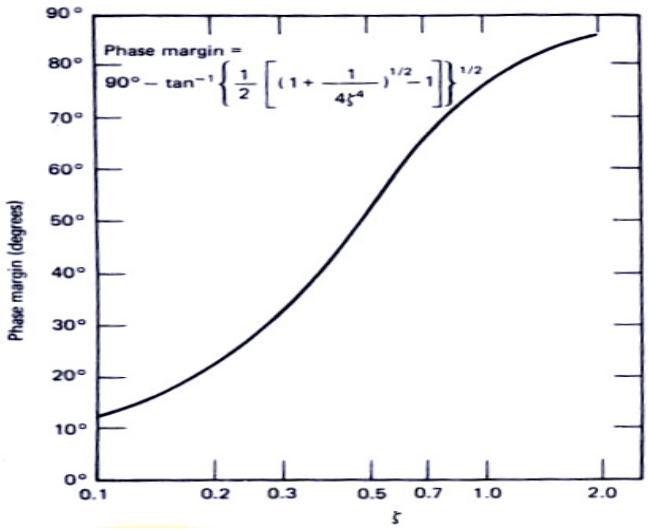

Figure AII.6 Phase Margin vs. damping factor for a loop with a low pass filter

(Reproduced from [57])

Open loop bandwidth can be set to any value provided it satisfies the less than 1/10 of the switching frequency of the power supply condition. Let's set it to 3dB closed loop bandwidth as in section 4.5.1.

Now

Phase margin = 65 degrees

Open Loop unity gain bandwidth = 3.7 kHz

VCO sensitivity = K_v = 14 MHz/V

PFD Constant = K_p = 2.5mA

RF Division Ratio = N = $\frac{2.45GHz}{200KHz}$ = 12250

Putting these values into equations 4.35 to 4.37, we obtain

C1 = 1.16 nF

C2 = 21.5 nF

R2 = 8.85 kΩ

One can appreciate the similarity of these component values to those obtained by the closed loop method for the first order filter. Actual values used were 1nF,22nF and 5.6KΩ respectively.

AII.2 Power supply input DC Offset circuitry

An offset voltage is provided at the control input of the input of the power supply, such that the magnetron is free running with about 100mA anode current before the frequency feedback control is turned on. Circuit diagram is shown in Figure AII.7.

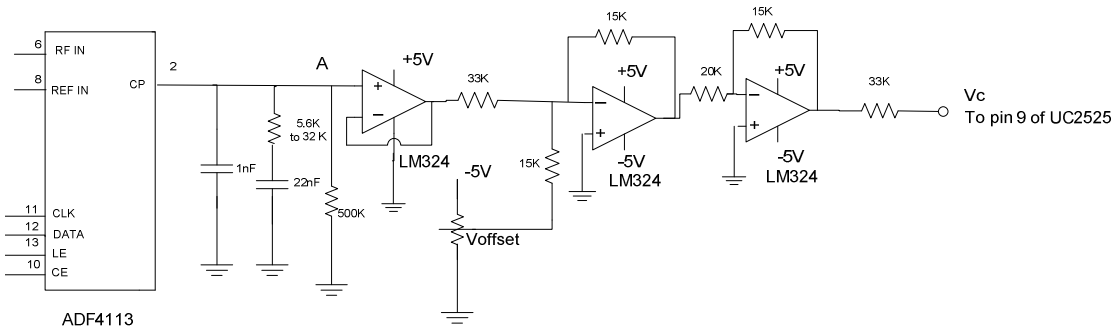

Figure AII.7 DC offset circuit along with ADF4113 output

Appendix III

THE INJECTION SOURCE

The injection source board we developed to phase lock the magnetron is shown in Figure AIII.1 and its schematic circuit diagram is shown in Figure AIII.2. The Injection source design uses same ADF4113 with a z-comm VCO V800ME11 VCO .Performance specifications of the VCO are shown in Table AIII.1.

In order to control the VCO's phase and frequency, it is phase locked to the same reference oscillator which is used for PLL control of the Magnetron. Reference and RF division ratios were chosen to achieve 200 kHz frequency steps. Frequency division registers and current setting in ADF4113 are programmed by the 89C4051 microcontroller. The inputs for both the injection source microcontroller and the magnetron frequency lock microcontroller are set in such a way that by pushing a single switch both ADF4113s are programmed with the same division ratios, hence the frequency of the magnetron and injection source are be the same. The output is amplified, using AD8353 as a pre-amplifier and AMP5000 as 1W output amplifier.

Parameters for the injection source PLL loop filter design were :-

Frequency sensitivity of the VCO =Kv = 56 MHz/V

Constant of PFD = Kp = 2.5 mA

RF Division ratio = N = 12250 (f_o = 2.45 GHz)

Open loop Bandwidth = 16 kHz

Phase margin = 55^o

Using (AII.30) to (AII.31) in Appendix II, we get

C1 = 1nF, C2 = 10nF, R2 = 3.15kΩ

PERFORMANCE SPECIFICATIONS	VALUE	UNITS
Oscillation Frequency Range	2400 - 2485	MHz
Phase Noise @ 10 kHz offset (1 Hz BW, typ.)	-97	dBc/Hz
Harmonic Suppression (2nd, typ.)	-20	dBc
Tuning Voltage	0.7-4.2	Vdc
Tuning Sensitivity (avg.)	56	MHz/V
Power Output	5±2	dBm
Load Impedance	50	Ω
Input Capacitance (max.)	50	pF
Pushing	<2	MHz/V
Pulling (14 dB Return Loss, Any Phase)	<15	MHz

Table AIII.1 Performance specifications of z-comm VCO VM800ME11(

Reproduced from VCO's datasheet [60]

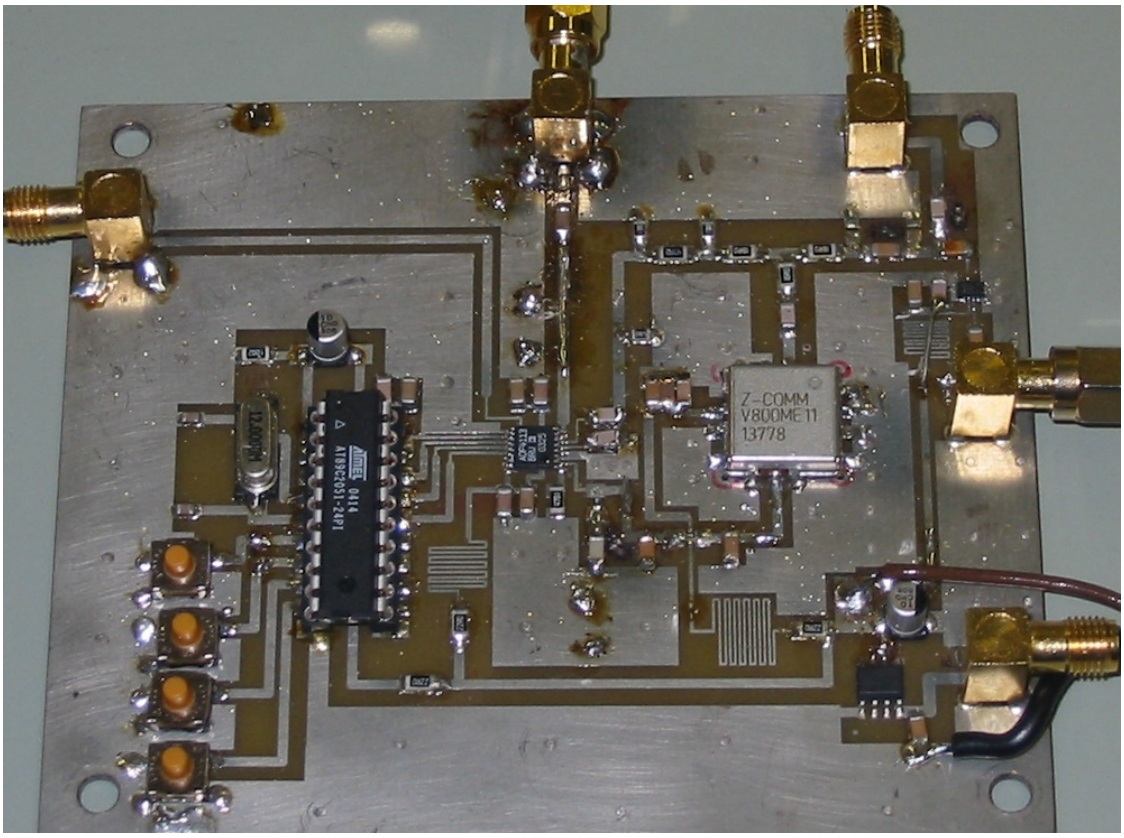

Figure AIII.1 The injection source board

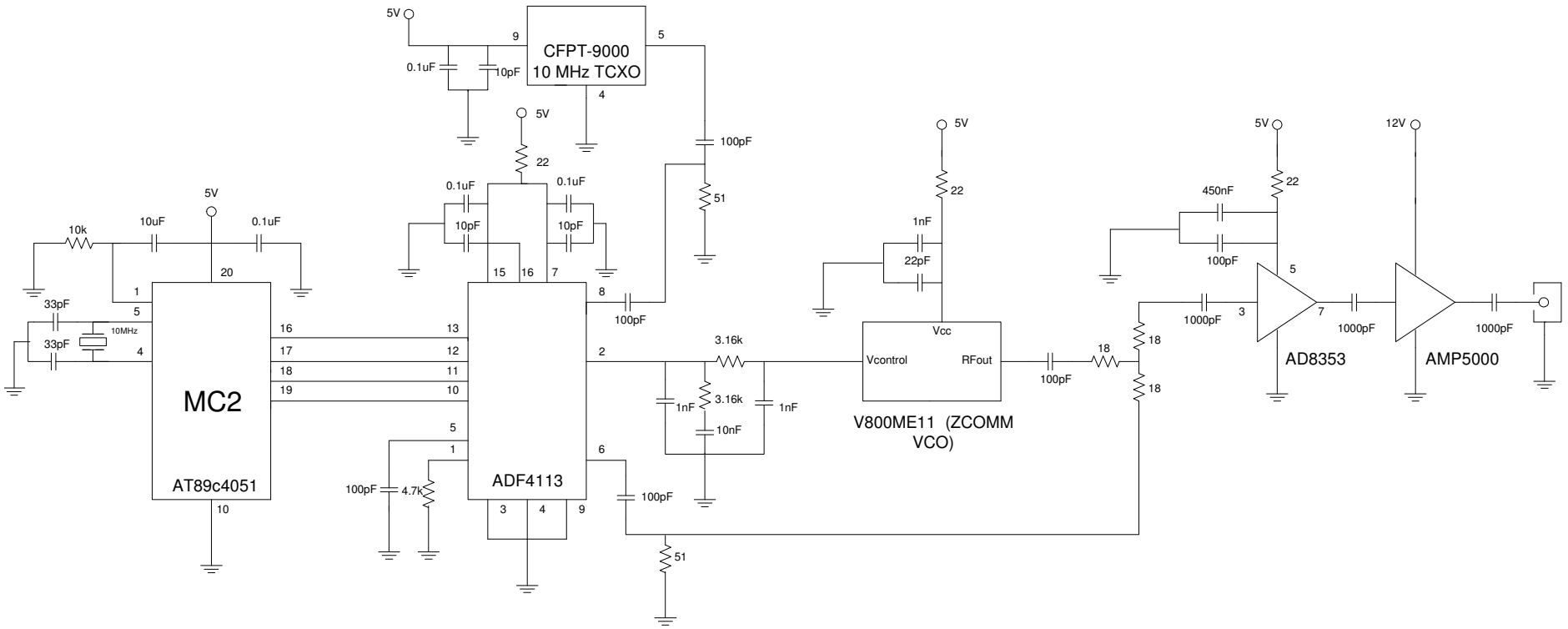

Figure AIII.2 Schematic diagram of the injection source

Appendix IV

C SOURCE CODE

Below is the C source code for microcontrollers (89c8051) that program different registers inside ADF4113 Chips. These microcontrollers are MC1 in Figure AII.1 and MC2 in Figure AIII.2.

```
#include <reg51.h>
sbit LE   = P1^4;
sbit DATA = P1^5;
sbit CLK  = P1^6;
sbit CE   = P1^7;
sbit E=  P3^5;
sbit F=  P3^4;
sbit G=  P3^3;
sbit H=  P3^2;
/* This function generates some delay if required*/
void delay(void){
unsigned int p;
for (p=0; p<100; p++);
}
/* This function generates the clock output for the serial peripheral interface between ADF4113 and the Microcontroller */
void clock (void){
CLK=0;
CLK=1;
}
/* This function generates the data output for the serial peripheral interface between ADF4113 and the Microcontroller */
void  shift( unsigned char x, unsigned char y, unsigned char z){
char a,b,word[4];
word[0] = x;
word[1] =
word[2] = z;

for (a=0; a<3;a++){
```

```
    for (b=0;b<8;b++){
                DATA= (bit) (0x80 & word[a] ? 1:0);
                clock();   // CLK pin goes high and the low for each data bit
                word[a] = word[a] << 1;   //shift left
               }
            }
  DATA= 0;
  CLK = 0;
  LE  = 1;              // LE (Latch Enable) goes high  then low at the end of one register write.
  LE  = 0;
}
/* This function writes values to different registers in ADF4113*/
void latches_dig_lock_detect (void){
shift(0x8D,0xA0,0x93); //Inilization latch, prescaler=32,MUXOUT =Digital Lock Detect, CP=Normal
shift(0x00,0x00,0xC8);  //Ref counter latch, Ref division ratio =50,. Step=200 KHz.
}
/*main begins*/
void main (void){
signed int  i, j, k;
DATA=0;
LE  =0;
CLK =0;
CE  =1;
latches_dig_lock_detect();
i = 126; j= 105;          // These values correspond to 2450 MHz
shift(1, i,j);            // Programming RF division ratio register in ADF4113

while(1){
while (E && F);
if (!E){
      j = j +4;                       //  J+4 corresponds to 200kHz Step
          if (j > 128)          { j= j-128; i = i + 1; }
          if ( i > 128)         i = 1;
          shift(1, i, j);
      }
while(!E);
        }


if(!F){
```

```
        j = j - 4;
            if (j < 0 ) { j = j + 128;; i = i - 1;}
            if (i < 1) i = 128;
            shift(1, i, j);
        }
while(!F);
        }
      }
}
/* main ends*/
```

REFERENCES

[1] K. Hinkel, "Magnetrons", Ch.1-4, 1st Edition, N.V. Philips' Gloeilampenfabrieken Eindhoven, Holland, 1961.

[2] M.L. Sisodia, "Microwave Active Devices, Vacuum and Solid State" Ch. 5, New Age International Ltd., New Delhi

[3] H. W. Welch, S. Ruthberg, H. W. Batten and W. Peterson "Analyis of dynamic characteristics of the magnetron space charge preliminary results", Technical Report No. 5, Electron Tube Laboratory, Department of Electrical Engineering, University of Michigan, 1951

[4] E. Okress, Ed., "Crossed-Field Microwave Devices", Ch. 4, vol.1, New York: Academic , 1961,

[5] Andrey V. Michin, "Portable linear accelerators for commercial applications" Proceedings for electron beam curing of composites workshop, Oak ridge, Tennessee, 10-11 Sep.1997.

[6] A.V Gritsunov, O.M. Nikitenko, "Probable sources of a noise in crossed field devices, Generating Tubes" 4th *IEEE Int. Conference on Vacuum Electronics,* May 2003.

[7] W.C.Brown, "The high signal to noise ratio of magnetrons and evidence of negative feedback to control it" Proc. 1st Int. workshop CVross-field devices, Aug. 1995, pp. 178-187.

[8] W.C. Brown, "The sophisticated properties of microwave oven magnetron", IEEE MTT-S Int. Symposium, Long Beach, CA, June, 1989.

[9] W.C Brown, "A reporting of personal observations of noise in magnetrons and CFAs" Raytheon Company, Waltham, MA Raytheon Internal Rep. PRP-5504, Mar. 1988.

[10] I.A. Karzhavin, B.Z. neyman, G.S. Gundobin, V.I. Vislov, A.V. Lashenko,, A.B. Levande, "A study of noise and collateral phenomenon observed in central cathode magnetron devices", *Applied Surface Science 215,* pp. 291-300, 2003.

[11] Spilios A. Riyopoulos, "Feedback induced noise in crossed field devices", IEEE Trans. On Plasma Sci., vol. 20, no. 5, June 1992.

[12] D.M. Variv and S.V. Sosnytskiy, "A comparative study of conventional and spatial harmonic magnetron", 4th *IEEE Int. Conference on Vacuum Electronics,*pp. 217-218*,* May 2003.

[13] Yokio Yamanks Characteristics of electromagnetic disturbances from microwave ovens and interface with digital communication systems

[14] K. Yamamoto, H. Kuronuma, T. Koinuma, and N. Tashiro, "A study of Magnetron Noise," IEEE Trans. Electron Devices, vol. ED-34 pp. 1223–1226, May. 1987.

[15] ---------,"The history of the reentrant beam crossed field amplifiers with emphasis on comparison with the magnetron" in *Proc. 1st Int. Workshop cross-field devices* , Aug. 1995, pp. 178-187

[16] H.G. Monossov, "Theoretical studies of magnetron noise by means of two dimensional simulation" 4th *IEEE Int. Conference on Vacuum Electronics,* pp. 370-371, May 2003.

[17] T. Mittani, N. Sinohara, H. Matsumoto, M. Aiga, N. Kuwahara and T. Handa, "Time domain analysis of noises generated from microwave oven magnetron" Electron. Commun. Jpn., vol. 88, pt. 2, no. 10, pp 28-36, 2005.

[18] George E. Domorowski, "Computer simulation study of primary and secondary anode loading in magnetrons", *IEEE Trans. On Electron Devices,* vol. 38, no. 10, Oct. 1991..

[19] Sun Shin Jung, Yun Sik Jin, and Hong-Sik Lee, "Three Dimensional Particle in cell simulations of a strapped magnetron oscillator" Journal of the Korean Physical Society, vol. 44, no. 5, pp. 1250-1255, May 2004.

[20] J.M. Osepchuk, "The Cooker Magnetron as a standard in crossed-field device research", *Proc. Ist Int. Workshop on Crossed-Field Devices*, Ann Arbor, Michigan, Aug 15-16, 1995, p159-157

[21] V. B. Neculaes, R. M. Gilgenbach, Yue Ying Lau, M. C. Jones and W. M. White "Low-Noise Microwave Oven Magnetrons with Fast Start-Oscillation by Azimuthally Varying Axial Magnetic Fields," *IEEE Trans. Plasma Science*, vol 32, 1152 –1159

[22] V.B Neculaes, M.C. Jones, R.M. Gilgenbach, Y.Y. Lau, J.W. Luginsland, B.W. Hoff, W.M. White, N.M. Jordan, P.Pengvanich, Y. Hidaka and H.L. Bosman, "A magnetic perturbation effect on noise and start up in DC operating oven magnetrons" *IEEE Trans. Electron Devices,* Vol. 52, no. 5, pp. 864-871, May 2005.

[23] ---------, “Magnetic priming effects on noise, start up and mode competition in magnetrons” *IEEE Trans. Plasma sci*., vol. 33, no. 1, pp. 94-102, Feb. 2005.

[24] N. Shinohara, H. Matsumoto and K. Hashimoto, “Solar Power Station/Satellite (SPS) with Phase Controlled Magnetrons”, IEICW Trans. Electron., vol E86-C, no 8, 2003

[25] Tahir I., Dexter A.C and Carter R.G., “Noise Performance of Frequency and Phase Locked CW Magnetrons operated as current controlled oscillators”, IEEE Transactions on Electron Devices, vol.52, no.9, pp2096-2103, 2005.

[26] .J. F. Hull, “Crossed field electron interaction in space charge limited beams,” Ph.D. dissertation, Dept. Elect. Eng., Polytechnic Institute of Brooklyn, NY, June 1958.

[27] Adler R. “A study of locking phenomena in oscillators” Proc IRE, vol 34, 1946

[28] B. Van der Pol, “The nonlinear theory of electric oscillations” Proc IRE, vol. 22, no. 9, pp1051-1086, 1934

[29] J.C. Slater, “The phasing of magnetrons” Res. Lab. Electron., MIT, Cambridge, MA. Tech Rep. 35, 1947.

[30] EE David, “RF phase control in pulsed magnetrons”, *Proc. IRE*, vol. 40, pp. 669-685, June 1952.

[31] Vaughan J.R.M. “A Model for Calculation of Magnetron Performance”, IEEE Transactions on Electron Devices, vol. 20, no. 9 pp818-826, Sep. 1973

[32] S.C. Chen, G. Bekefi and R.J. Temkin “ Injection locking of long pulsed relativistic magnetron”, in proc. PAC, 1991, PP. 751-753.

[33] T.A. Treado, R.A. Bolton, T.A. Hansen, P.D. Brown, and J.D. Barry, “High Power high efficiency injection locked secondary emission magnetron”, *IEEE Trans. Plasma Sci.* , vol. 20, no.3, pp. 351-359, June 1992

[34] Woo W. et al. “Phase locking of high power microwave oscillators”, J. Appl. Phys., vol. 65, no.2, pp861-866, 1989

[35] R.D. Weglein and H.A. Leach, “The noise behaviour of an injection locked magnetron reflection amplifier” in Proc. IEEE MTT-S Int. Microwave Symp., 1987, pp. 261-264..

[36] W.E. Garrigus, “Phase noise performance of magnetrons” *Microw. J.*, vol. 20, pp59-73, July 1977.

[37] J. Kline, “The magnetron as a negative resistance amplifier” IRE Trans. Electron Devices, vol. ED-8, no. 6, pp. 437-442, Nov. 1961.

[38] H.L.Thal and R.G. Lock, “Locking of magnetrons by injected RF signal” IEEE Trans. Microw. Theory Tech., vol. MIT-13, no. 6, pp 836-846, Nov. 1965.

[39] M.H. Seavey Jr. “Some properties of an injection locked pulsed magnetron, in a coherent echo detection system” electron Lett. Vol. 3, no. 8, pp. 375-377, Aug. 1967.

[40] T Overett, D. B. Remsen, E. Bowles, G. E. Thomas and R. E. Smith, “Phase locked magnetrons as accelerator RF sources”, in *Proc. PAC*, 1987, pp. 1464-1465.

[41] I.Tahir, A. Dexter, R. Carter, “Frequency and phase modulation performance of an injection locked CW magnetron”, IEEE Trans. On Elecetron Devices, vol. 53, no.7, July 2006.

[42] I.Tahir Fast feedback control of the magnetron

[43] Behzad Razavi, “A study of injection locking and pulling in oscillators”IEEE Journal of solid state circuits, vol. 39, no. 9, Sep. 2004.

[44] Ayvazyan V., et al., “Digital low level RF control system for the DESY TTF VUV-FEL linac”, TESLA-FEL Report 2005-06, DESY, Hamberg

[45] William O. Keese, “An analysis and performance evaluation of a passive filter design technique for charge pump phase locked loops”, National Semiconductor Application Note AN-1001, May 1996

[46] Analog devices adf4113 datasheet

[47] Anupama Hegde, “Phase-Locked Loop Clock Generators” , Application Note AN-155, Integrated Device Technologies, 1996.

[48] Erickson, R.W. and D. Maksimovic, “Fundamentals of Power Electronics”, Chapman and Hall, May, 1997.

[49] Pressman, Abraham I., “Switching Power Supply Design”, McGraw-Hill Professional; 2nd edition,Nonember,1997

[50] Device datasheet, SG2525, ST Microelectronics

[51] SM745 Switched-mode power supply wiring diagram, Aalter systems, Italy.

[52] Device Datasheet, HCPL2211, Agilent Technologies.

[53] Device Datasheet, IXGR32N60CDI, IXYS Corporation

[54] Device datasheet, IR2110 , International Rectifiers

[55] Best, Ronald E., Phase Locked Loops: Design, Simulation, and Applications, McGraw-Hill Professional, New York, 1999

[56] Gardner, F.M., Charge-Pump Phase-Lock Loops, IEEE Trans. Commun., vol. COM-28, pp 1849-1858, Nov 1980

[57] Gardner, F.M., Phase-Locked Loop Techniques, 2nd ed., John Wiley & Sons, 1980

[58] D. Stephens, Phase Locked Loops for Wireless Communications, Kluwer Academic Publishers, Norwell, MA, 2002.

[59] Garth Nash, "Phase-locked loop desighn fundamentals", Motorola Inc., Application Note An535, rev. 0, 1994.

[60] Device datasheet, VM800ME11 HMC439, Z-communications

[61] Device Datasheet, HMC439, Hittite Inc.

[62] Stephan R. Kurtz, "Mixers as phase detectors", WJ Tech Notes, vol. 5, no. 1, Jan/Feb 1978.

[63] George B. Collins, "Microwave Magnetron", 1st Edition, McGraw-Hill Book Company Inc, 1948

[64] S. Dushman, "Electron emission from metals as a function of temperature" Phys. Rev. 21: 623-636 (1923)

[65] Langmuir & KB Blodgeth, "Currents limited by space charge between coaxial cylinders" Phys. Rev. 22 : 347-356 (1922)

[66] Leon Nicolas Brillouin, "Les électrons dans les métaux et le classement des ondes de de Broglie correspondantes". Comptes Rendus Hebdomadaires des Séances de l'Académie des Sciences 191 (6):292-94

.